Dynamic Elastography of Pre-stressed Material with Multi-Directional Excitation in High Field MRI System

BY

ALBERTO GIAROLA
B.S. , Politecnico di Torino, Turin, Italy, 2019

THESIS

Submitted as partial fulfillment of the requirements
for the degree of Master of Science in Mechanical Engineering
in the Graduate College of the
University of Illinois at Chicago, 2021

Chicago, Illinois

Defense Committee:

Thomas J. Royston, Chair and Advisor
Dieter Klatt
Marco Carlo Masoero, Politecnico di Torino
Pasquale Vena, Politecnico di Milano

To my mother and father

ACKNOWLEDGMENTS

First of all, I would like to express my sincerest thanks to Doctor Thomas J. Royston for being my guide during these months and welcoming me to the Acoustic and Vibrations Laboratory. I am grateful for this opportunity to work in such an advanced and innovative field of study.

Furthermore, I want to thank Prof. Marco Carlo Masoero for his support and helpfulness throughout my work.

My gratitude goes also to Prof. Pasquale Vena for accepting to be my supervisor on such short notice, and for his willingness to help me in my research.

I would also like to thank Federica for standing by me and standing me, during this adventure abroad, and for her enlightening help in the biomedical aspects of my thesis. Many thanks also to Joseph Crutison, Harish Palnitkar, Melika Salehabadi, and Luca Leoni for their valuable teachings on how to use the laboratory equipment. Sincere thanks also to Joshua Smejkal for his manufacturing assistance in building the mechanical parts of my experiments.

A special thanks also to my fantastic friends, far away, but always close in the heart.

Last but not least, my deepest and unconditional gratitude goes to my family, and in particular to my parents, Patrizia e Roberto, for their emotional and practical support, not only during these academic years but also during my entire life. What is essential is invisible to the eyes, but thankfully you are here, and I can see you every day.

AG

TABLE OF CONTENTS

TABLE OF CONTENTS (continued)

CHAPTER **PAGE**

LIST OF TABLES

LIST OF FIGURES

LIST OF FIGURES (continued)

LIST OF FIGURES (continued)

LIST OF FIGURES (continued)

LIST OF ABBREVIATIONS

DLP	Digital Light Processing
DUS	Diagnostic Ultrasound
ID	Inner Diameter
LDV	Laser Doppler Vibrometry
MF	Magnetic Field
MR	Magnetic Resonance
MRE	Magnetic Resonance Elastography
MRI	Magnetic Resonance Imaging
OCE	Optical Coherence Elastography
OD	Outer Diameter
PM	Permanent Magnet
ROI	Region Of Interest
SI	International System of units
SLA	Stereolithography
SLDV	Scanning Laser Doppler Vibrometry
US	Ultrasound
USE	Ultrasound Elastography

SUMMARY

The main object of this thesis is the design and manufacturing of a mechanical setup to drive multi-directionally-polarized shear wave motion for the purpose of dynamic elastography in a tensile pre-stressed anisotropic biological sample in an Ultra-High Field MRI system. The main requirements for this task are the structural stability of the system at high frequencies, the nonmagnetic materials needed for the manufacturing (since the magnetic field applied is in the order of magnitude of 10 Tesla and magnetic materials pose both a danger and will distort the acquired image), and the connectivity between the actuators and the wave generator to monitor and control the excitation. Once the setup is created, the testing is performed and from the results of the same, the imagining and evaluation steps of the iterative design process are repeated.

After an initial analysis of the different Elastography techniques, the focus is set to the Magnetic Resonance Imaging one. The main functioning and hardware requirements are explained, and an overview of the current equipment is provided. Afterward, the design of the setup itself is presented in detail with particular attention to the matching between all the components and the materials adopted to manufacture them. Finally, the testing with different experimental methods is conducted, and the results are discussed and compared with the expected theoretical ones. From this comparison, a conclusion on the validity of the experiments is proposed and some future developments are suggested to continue the work most effectively and efficiently.

CHAPTER 1

INTRODUCTION

1.1 Background

Hundreds of years ago, it has been recognized the correlation between the mechanical properties of tissues and the presence of a disease or an injury. In particular, the subject of particular attention is the elasticity and the viscosity of the tested sample. The first and easiest way that has been used to gain knowledge of these properties was through a biopsy. Nevertheless, this is an invasive way of operating, as well as inefficient considering the sampling error and inability to perform the operation "in vivo". Subsequently, it has gone from the biopsy to the manual palpation to identify the presence of tumors or fibrotic tissues. This practice is not invasive, but only qualitative. At the same time, it works properly only with superficial tissues and it is strongly operator-dependent. For this reason, a new imaging technique has been developed. Elastography is different from the other imaging technique because the result is a quantitative map of the elastic properties and stiffness of the soft tissue analyzed [1]. In the last 30 years, in Elastography two main imaging methods drew particular attention in the clinical field of study, based on ultrasound and Magnetic Resonance Imaging (MRI). A common feature of these methods is that they both combine an imaging technique with a mechanical excitation. One of the main advantages of this is being able to obtain quantitative details on the mechanical properties of the area of study in a non-invasive way. The main differences between these two methods

are that ultrasound elastography is portable, and it provides a good resolution when the tissue of interest is right below the surface [2]. On the other hand, MRI requires more complex and expensive equipment, and it cannot be bedside. Nevertheless, the advantages of MRI are the deeper penetration behind bones and the motion encoding in three directions simultaneously. On the contrary, ultrasound elastography has a limited penetration depth, and one motion of encoding only. MRI is also able to give more specific frequency-dependent information, which can be valuable in some applications. To provide the mechanical vibration needed for the acquisition of the elastic properties there are two main devices, the piezoelectric actuators and other electromechanical ones based on the Lorentz force. The first ones are transducers that convert an electrical input into a mechanical displacement or stress using the piezoelectric effect. This ability of certain material consists in converting an electrical field into a mechanical strain. The Lorentz-force actuators, instead, take advantage of the magnetic field generated by a conducting coil wire to move a permanent magnet, according to the Lorentz force [3].

1.2 Elastography

Elastography is a medical imaging technique that determines the stiffness of organs. It is non-invasive, and for this reason, it is commonly used to assess the liver. During Elastography, painless low-frequency vibrations are directed to the organ. Ultrasound (US) or Magnetic Resonance Imaging (MRI) acquires the vibrational signals that moved through the organ, and thanks to this information the system is able to create a visual map showing the stiffness of the organ [4].

In the case of a US Elastography, the equipment needed for the scan consists of a computer

console, a transducer, and a video display screen. The transducer is responsible for sending out the sound waves into the body and collecting the returning signal. For an MR Elastography instead, the equipment is a large cylinder-shaped tube surrounded by a circular magnet. The type of equipment that will be used in this paper is this second one.

The main benefits and risks of this procedure are herein summarized in the table below (Table I):

TABLE I: COMPARISON BETWEEN BENEFITS AND RISKS OF ELASTOGRAPHY

Benefits and risks of Elastography	
Benefits	**Risks**
Non invasive	If sedation is used, there is a risk of using too much
Not involve exposure to ionizing radiation	The MF can cause malfunction in implanted medical devices
Can detect diseases such as fibrosis earlier than other imaging tests	In case of a gadolinium contrast injection, nephrogenic system fibrosis may occur
Can help predicting the risk of certain complication, such as ascites	Slight risk of allergic reaction if contrast material is used
Asseses a large portion of the organ	
May eliminate the need for biopsy	

In general, the elastographic methods can be divided into three main categories: Devices for testing ex vivo samples, Quasi-static elastography, and Dynamic elastography [5]. A graphical

representation of the methods is shown in Figure 1:

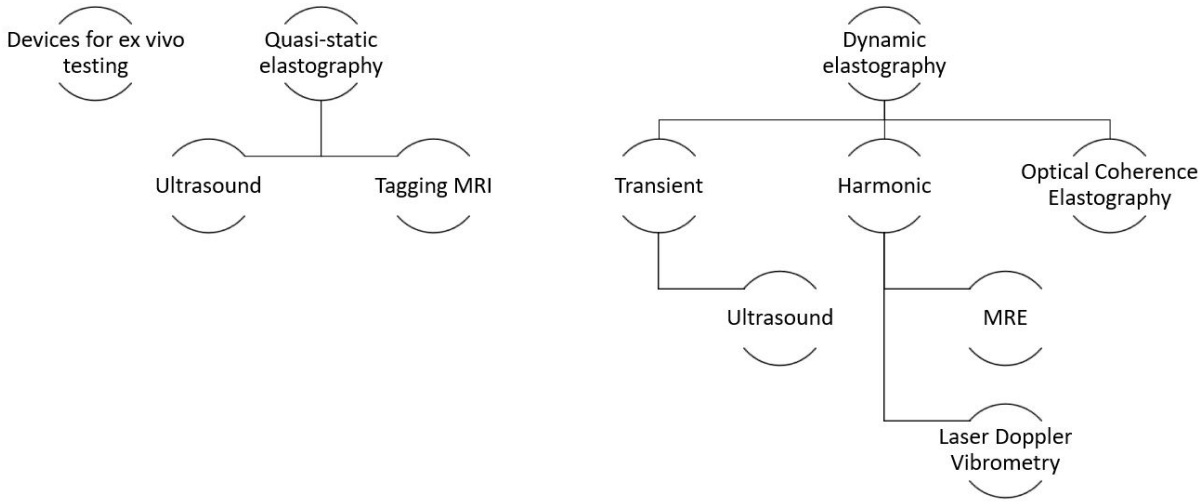

Figure 1: Scheme of the elastographic methods.

The first type requires taking the tissue out of the body to evaluate its mechanical properties. An example of a device used for this purpose is the indentation device [6]. By measuring the force needed to cause a deformation it is possible to evaluate the mechanical properties of the tissue according to the Amador mathematical formula [7]:

$$F = \mu\delta\frac{1-\gamma}{4af(\gamma, a/h)} \tag{1.1}$$

Where:

F is the indentation force

μ is the shear modulus

δ is the deformation

γ is the Poisson ratio

a is the radius of the cylinder that is causing the deformation

h is the thickness of the tissue

f is a function that varies from tissue to tissue

A scheme of the device is presented in Figure 2:

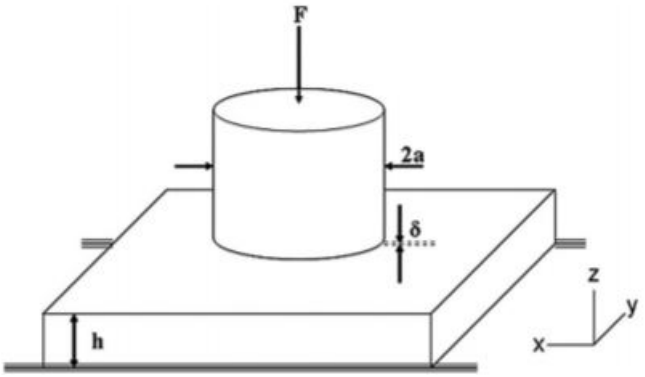

Figure 2: Graphical representation of an indentation device.

In the second one, the Quasi-static method, a deformation is applied and then the acquisition of data is implemented. The measurement is performed in a state of rest even if the tissue was previously excited by a vibration. There are two different techniques used in this case, the ultrasound-based procedure and the MRI one. It is important to underline that both these methods boundary conditions can play a significant role, and observations of natural tissue deformation may be used for relative, but not absolute, tissue stiffness assessment. The ultrasound-based procedure uses a static compression applied to the tissue through the transducer to create a deformation in the material. If a phantom with different inclusions is considered, from the deformation it is possible to determine the different stiffness of the inclusions but only in a relative way. The inclusions can be compared between each other but it is not possible to extract exact values of the stiffness of the material [8]. On the other hand, the tagging MRI procedure uses special MRI sequences, called tagging MRI sequences, that are saturated in specific regions. In these sequences, some areas are suppressed by the signal and appear as "dark regions", while others appear as "white regions". The deformation is caused by the muscles themselves, and for this reason, this technique is commonly used for myocardial tagging. The dark and white regions create a grid that deforms accordingly to the myocardial tissue during cardiac contraction and tracking this grid allows to assess the displacement of the myocardial tissue and calculate cardiac strain [9]. Another interesting application of this method is in the cardiac-induced strain in the liver. Thanks to the tagging MRI technique it is possible to assess the smaller cardiac-induced strain in the liver of cirrhotic patients [10].

In the last method, Dynamic elastography, the excitation is performed during the acquisition of data. This method can be subdivided into two other categories which are harmonic and transient. In the harmonic case, the tissue oscillates as a harmonic function, while in the transient one typically a pulse propagates through the tissue creating a disturbance and while this displacement occurs, data is acquired.

The first category is frequently associated with the MRI. This technique will be further discussed in the next chapters. At this point of the introduction, it can be said that MRI is a medical imaging technique using magnetic fields and gradients, with radio waves, to generate images of the organs in the body [11].

This second category is commonly associated with Ultrasound Elastography (USE). US is a compression wave above the sound, with a frequency greater than 1.6 Hz. The frequency range used for the Diagnostic Ultrasound (DUS) is $10^6 - 4 \cdot 10^7$. A typical transducer for DUS has an operating frequency of $2MHz - 20MHz$. It takes advantage of the piezo-electric effect to detect and transmit vibrations. The piezo-electric effect consists of generating an electric signal in response to applied mechanical stress, and vice versa thanks to the micro-structure of certain materials [12]. When the transducer is used as a detector, it receives mechanical stress from an external force and it transforms the displacement into an electrical signal that is elaborated by the computer. On the other hand, when it is used to transmit vibration, the electric signal is given by the machine and the material responds with a displacement that causes mechanical stress. A scheme of the functioning of a piezoelectric material is shown in Figure 3.

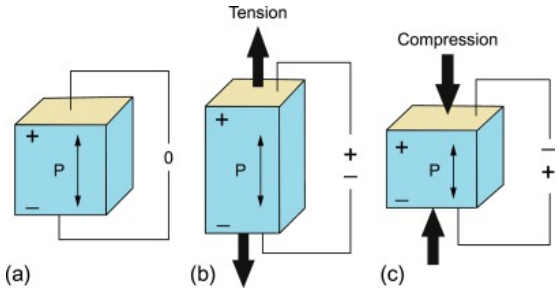

Figure 3: Scheme of the piezoelectric effect

By combining the transmission and the detection of the vibration it is possible to evaluate the travel time. Assuming the speed to be constant, it is possible to evaluate the distance between the transmitter and any object according to the formula:

$$speed = \frac{2 \cdot distance}{travel\ time} \tag{1.2}$$

When using this formula, it is crucial to remember that multiple echo arrivals indicate multiple reflection horizons but they can also be caused by multiple reflections at parallel, strongly reflective interfaces. A graphical representation is presented in Figure 4:

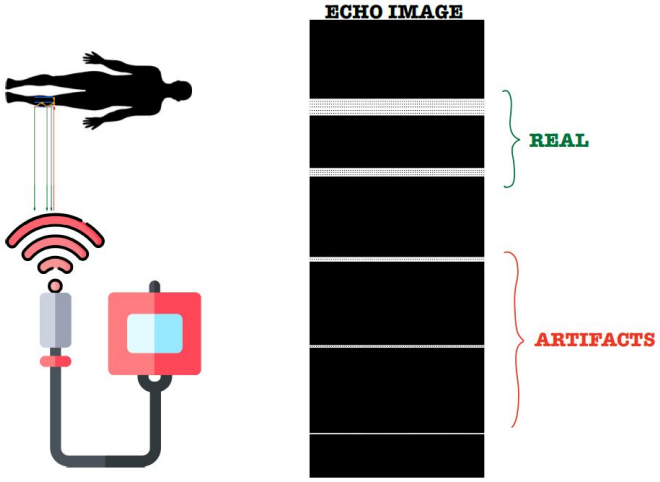

Figure 4: Multiple reflection scheme in US systems.

Radiologists have to keep in mind this phenomenon when operating.

1.3 Motivation

The presented research has the objective of leading to improvements in surgical procedures and enhance a doctor's ability to navigate around the body during operations [13]. To do so, an experimental setup is created to stimulate a biological anisotropic phantom in an Ultra High Field MRI system. Thanks to the results of these experiments it will be possible to better understand the propagation of mechanical waves into anisotropic materials such as the human muscles. In particular, it will be possible to have a comparison between the theoretical results given by the laws that govern the propagation of waves in a pre-stressed material, and the empirical results given by the experiments. The comparison is intended to be performed both

for the axial and the torsional excitation of the muscle. With this knowledge, the MRI and MRE techniques can be further developed and applied to human bodies. Elastography is a non-invasive imaging method that allows, simultaneously, to have quantitative information about the mechanical properties of the tissues.

Therefore, this work aims to design a mechanical setup able to excite torsionally a biomedical phantom or soft tissue specimen for the MRE technique. Starting from the evaluation of the mechanical properties of homogeneous and anisotropic polymer samples, the intention is then to move forward to human tissues like muscles. The experiments are intended to be performed in Ultra High Field MRI System which is, in this case, the Agilent 9.4 T. For this reason, the whole setup is intended to be completely amagnetic, and the dimensions thereof are designed to fit into the Ø72 mm cave of the Permanent Magnet (PM).

Besides, the value of this research lies also in the similar mechanical properties between the human soft tissues and the biological phantoms used for the experiments [14]. This symmetry can be seen in particular in three properties:

1. *Poisson coefficient:* both of them are very close to the one of incompressible materials:

$$\nu = 0.5 \tag{1.3}$$

Where:

ν is the Poisson coefficient

2. *Young's modulus:* the relation between the shear modulus and the Young's modulus is a linear one with a scaling factor of 3 for both the materials:

$$E = 3\mu \tag{1.4}$$

Where:

E is the Young's modulus

μ is the shear modulus

3. *Density:* the value is almost the same as water for both the materials:

$$\rho = 1000\ \frac{kg}{m^3} \tag{1.5}$$

Where:

ρ is the density

Note that for all the units of measurements considered in this paper are the ones of the International System of Units (SI).

1.4 Objectives

The objectives of this project can be collected and organized into three specific aims as listed below:

1. **Develop an anisotropic phantom with three layers of different mechanical properties to mimic a biological muscular tissue.** From previous researches differ-

ent phantoms have been produced in terms of dimensions, material, and manufacturing technique. Starting from those models, the maximum number of layers that have been implemented was two. The goal is to add another layer to the previous model to better simulate the anisotropy of human tissue. According to this new model the phantom will present an external matrix made with the softest material between all of the materials used, a circular concentric repetition of cylinders that run through the phantom made with an intermediate material in terms of stiffness, and inside every cylinder another concentric circular repetition of cylinders that extend for the length of the sample made with the stiffest material between all of the material used. The geometry has been accurately designed to fulfill the mechanical requirements of the sample but at the same time to guarantee the feasibility of the production. The material used for every layer of the model is $EcoFlex^{TM}$, with different levels of stiffness for every layer. The molds are 3D printed with a DLP Photon Mono SE. The material used for the mold is Siraya Tech *Fast*. The sample is then tested with MRE experiments using an Agilent 9.4 T in an Ultra High Field MRI System.

2. **Design and test a mechanical setup for torsional excitation in an Ultra High MRI System.** To better understand the analytical theory for shear wave propagation in anisotropic media, a mechanical device able to stimulate a biomedical phantom torsionally has been developed. Staring from designs of previous years, a horizontal system laying on a half-tube is designed. The movement is given by two piezoelectric actuators connected to the same wave generator to impart the same force on one of the edges of the phantom

through the mobile support. The goal is to generate momentum over the sample and take advantage of the shear wave propagation for the MR Elastography of the phantom on the Agilent 9.4 T system. The results are compared with the Table-Top MRI system.

3. **Analyze the results of the MRE experiments on different phantoms and validate the predictions from the computational model.** Once the setup is ready, several experiments are performed on different phantoms – starting from the isotropic one and moving to the ad hoc designed phantom with three layers of anisotropy. The expected result is an accurate image acquisition of the biological sample as well as a close approximation of the mechanical properties of the same.

An improvement in the model and the understanding of the wave propagation in the Magnetic Resonance Elastography technique can improve the detection of tumors or cirrhosis. Very often a different stiffness in specific regions of soft tissues such as the brain, heart muscle, tendons, and ligaments can be associated with the presence of a disease. In these terms, a standardized MRE applied to anisotropic tissues can help in the diagnosis and prevention of this sort of illness.

CHAPTER 2

MAGNETIC RESONANCE ELASTOGRAPHY

2.1 MRI and MRE

To move from the MRI to the MRE it is needed to detect the mechanical properties of the tissues examined. To do so, is necessary to invert the Navier's equation for 3D viscoelastic wave in frequency domain below [15]:

$$-\omega^2\mathbf{U}(\omega) = (G_L(\omega) + G_S(\omega))\nabla(\nabla \cdot \mathbf{U}(\omega)) + G_S(\omega)\Delta\mathbf{U}(\omega) \tag{2.1}$$

Note that:

$$\nabla = \vec{e}_x\frac{\delta}{\delta x} + \vec{e}_y\frac{\delta}{\delta y} + \vec{e}_z\frac{\delta}{\delta z} \tag{2.2}$$

$$\Delta = \nabla \cdot \nabla = \frac{\delta^2}{\delta x^2} + \frac{\delta^2}{\delta y^2} + \frac{\delta^2}{\delta z^2} \tag{2.3}$$

Where:

ρ is the density of water

$\mathbf{U}$ is the complex wave image (deflection)

G_L is the complex modulus of 1^{st} (λ) Lame-parameter

G_S is the complex modulus of 2^{nd} (μ) Lame-parameter

The diagnostic information that is the object of interest for this research is contained in the G_S modulus. The G_L modulus, instead, does not contain any diagnostic information. To obtain G_S is then necessary to measure **U**, that is the displacement. **U** corresponds to the displacement vectors in the 3D system, and for this reason, it is space-dependent. MRI is the tool used to determine this displacement [5].

MRI is different from other imaging techniques because MRI signals can be tuned sensitive to a variety of contrast parameters. Different MRI sequences can be set to obtain different image contrasts as it can be seen in the Figure 5 below:

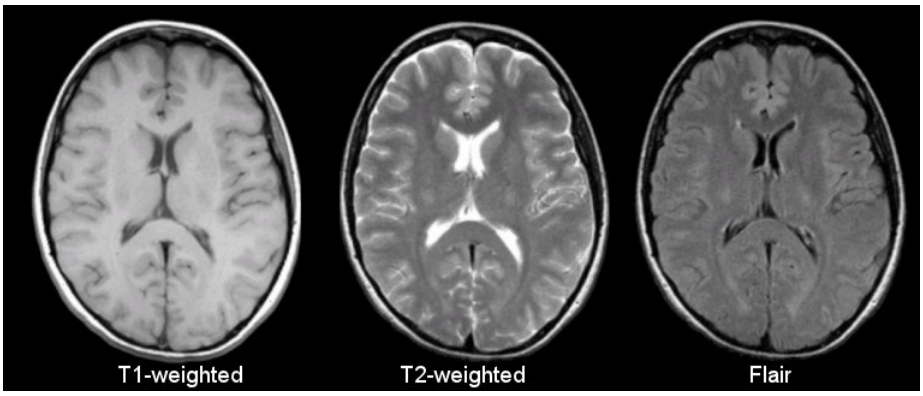

Figure 5: Different image contrasts in MRI scans of a brain.

What is measured in the MRI scan is the so-called *Transverse Magnetization* (M_T). This is a magnetization vector in the x-y plane that is rotating on the plane at the time of reading. Because the signal is in the x-y plane it is possible to make it a complex value. For this reason, in every scan two images are acquired, the *Magnitude* (that corresponds to the real part) and the *Phase* (that corresponds to the imaginary part) of the Transverse Magnetization. See Figure 6 below:

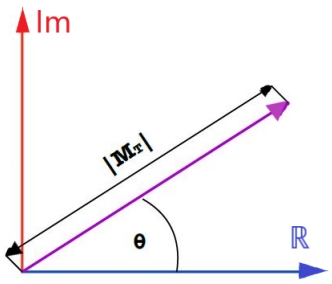

Figure 6: Transverse Magnetization – Argand plane representation.

Starting from these two values, it is then comprehensible to relate the magnitude and the phase to a harmonic signal as shown in Figure 7:

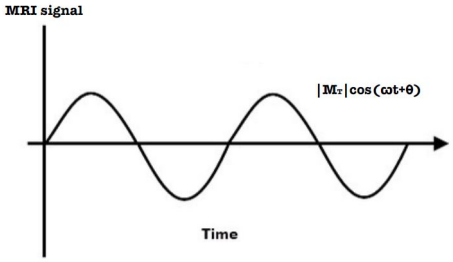

Figure 7: Transverse Magnetization – Harmonic sinusoidal wave representation.

2.1.1 MR Physics

MRI is based on the magnetization of atomic nuclei [16]. Each nucleus can be taken as a magnet because of its spin which involves a magnetic moment as shown in Figure 8.

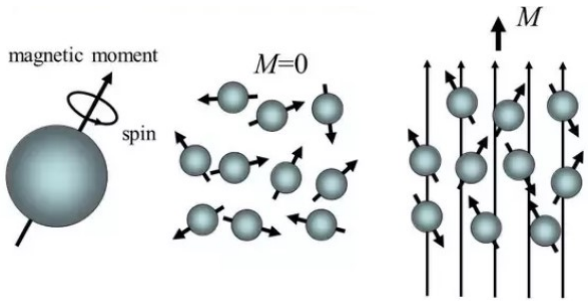

Figure 8: Representation of the magnetic moment for unpaired protons.

Thanks to the external magnetic field applied by the permanent magnet, the spatial orientation of this magnetic moment is modified. Nevertheless, since most applications in MRI are proton-based, the presence of water is needed in the tissue examined. Indeed, the MRI method is more suitable for soft tissues where there is a high percentage of water. The hydrogen atoms resulting from the water splitting are precisely the unpaired protons that take part in the external magnetization process. The splitting process is herein chemically presented:

$$H_2O \iff H^+ + OH^- \tag{2.4}$$

The process is summarized in Figure 9 below:

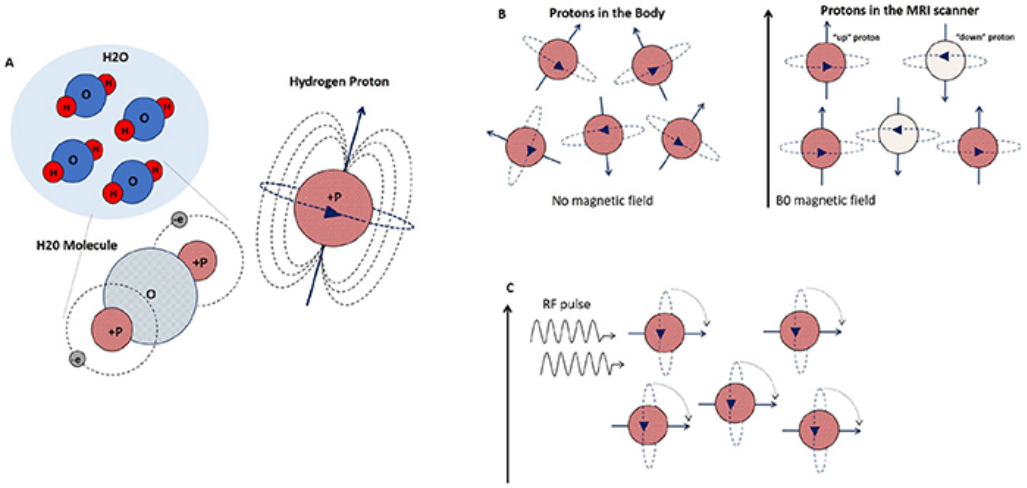

Figure 9: Graphical representation of the process of water splitting and magnetic moment generation.

Note that the model used for describing the physics of MRI is the *Semi-classical* one. In Figure 9 it is possible to graphically understand the magnetic moment generation from the proton spin (A), protons alignment with the external magnetic field (B), and protons flipping when a RF wave with the same frequency as the proton's Larmor frequency is turned on (C).

After the external magnetic field of the permanent magnet is applied, the energy level of the proton is split into two. The energy difference between the two levels can be evaluated according to the formula below:

$$\Delta E = \gamma h B \tag{2.5}$$

Where:

ΔE is the Energy split

h is the Planck-constant

γ is the gyromagnetic ratio (specific of the nucleus)

B is the magnetic field strength

This phenomenon of splitting the spectral line into several components is called the Zeeman effect, and it occurs whenever a static magnetic field is applied to an atom [17].

An example is herein presented for an isotope of rubidium (Figure 10):

The product between the gyromagnetic ratio and the magnetic field is called *Larmor frequency.* This frequency is the signal measured by the MRI system [5].

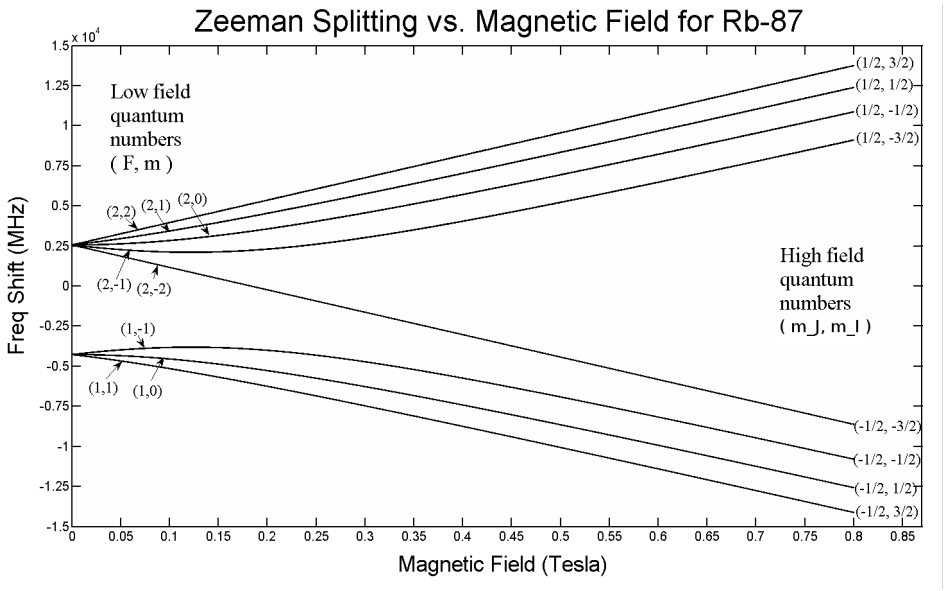

Figure 10: Zeeman effect for Rb-87 as a function of the magnetic field.

$$\omega = \gamma B \tag{2.6}$$

If the gyroscopic ratio is assumed to be constant, which is comprehensible considering that only hydrogen nuclei are taken into consideration, it is possible to vary **B** and obtain different Larmor frequencies that contain information on where the signal is spatially located. This is indeed the basic principle of MRI. When the external magnetic field **B** is applied, thanks to the paramagnetism of the material, a macroscopic magnetization **M** occurs. The thermal equilibrium manifests itself when **B** and **M** are parallel. The macroscopic magnetization **M** is made up of two components, the *Longitudinal Magnetization* (M_L) and the *Transverse Magnetization*

(M_T), this second component is the one that can be measure with the RF coils, and for this reason, it is important to create this component. The macroscopical magnetizaton **M** equations of motion are called *Bloch equations* and can be written in the following componential form [18]:

$$\frac{dM_x}{dt} = \gamma(\mathbf{M} \times \mathbf{B})_x - \frac{M_x}{T2} \tag{2.7}$$

$$\frac{dM_y}{dt} = \gamma(\mathbf{M} \times \mathbf{B})_y - \frac{M_y}{T2} \tag{2.8}$$

$$\frac{dM_z}{dt} = \gamma(\mathbf{M} \times \mathbf{B})_z - \frac{M_0 - M_z}{T1} \tag{2.9}$$

Where:

M_x is x component of the macroscopical magnetization

M_y is y component of the macroscopical magnetization

M_z is z component of the macroscopical magnetization

γ is the gyromagnetic ratio (specific of the nucleus)

T1 is the Longitudinal relaxation time

T2 is the Transversal relaxation time

M_0 is the Magnetization in thermal equilibrium

From these equations, it can be stated that the Transversal Magnetization (M_T) can be excited by using RF pulses with Larmor frequency equal to $\omega = \gamma B$. At the same time, it is clear the precession of **M** around **B** with Larmor frequency $\omega = \gamma B$, and the tendency of M_T

to converge to 0 and M_L to M_0 because of the damping term. Moreover, the consequences of these equations are that in thermal equilibrium there is only a longitudinal magnetization M_z, which is the direction parallel to the main magnetic field. To create the transverse component an RF panel with the Larmor frequency is used [5].

The angle by which the Magnetization in thermal equilibrium is flipped can be evaluated according to the following formula [19]:

$$\alpha = \int_0^\tau \Omega_1(t)\, dt = \gamma \int_0^\tau B_1^e(t)\, dt \tag{2.10}$$

That becomes, in case of a rectangular pulse:

$$\alpha = \gamma B_1 \tau \tag{2.11}$$

Where:

τ is the duration of the RF-pulse

B_1^e is the envelope of the RF-pulse

B_1 is the amplitude of the RF-pulse

Ω_1 is the frequency of the RF-pulse

B_0 is the magnetic field from the MRI magnet

To obtain the resonance condition, which means flipping M_0 by 90° (i.e. $\alpha = 90$), the frequency of the RF-pulse should be equal to the Larmor frequency:

$$\Omega_1 = \gamma B_0 \tag{2.12}$$

After the nuclei have been perturbed by the external RF energy, they return to their resting position through different relaxation mechanisms emitting RF energy again. By using Fourier transformation the RF energy becomes a signal from each location in the imaged plane to corresponding intensity levels, which creates the different shades of gray that appear in the matrix arrangement of pixels [16].

As anticipated before, the MRI method is one of the most powerful because of its flexibility. In fact, by changing the sequence of RF pulses applied and collected, different types of images can be created. The two parameters that can be varied are [16]:

- **Repetition Time (TR)**: it is the time between two pulse sequences applied to one slice consecutively
- **Time to Echo (TE)**: it is the amount of time between the arrival of the RF pulse and the obtaining of the echo signal

As shown before, during the process there are two different relaxation times:

- **Longitudinal relaxation time (T1)**: it is a constant that expresses the time required by the excited protons to come back to the equilibrium position. It is the time needed

by spinning protons to align again with the external magnetic field or to return to the Gaussian distribution of spin states in the absence of an magnetic forces

- **Transverse relaxation time (T2)**: it is a constant that expresses the time required by the excited protons to reach equilibrium or go out of phase with each other. It is the time needed by spinning protons to lose phase coherence between the nuclei that spin perpendicular to the external magnetic field [16]

A graphical representation of the relaxation times is herein presented (Figure 11):

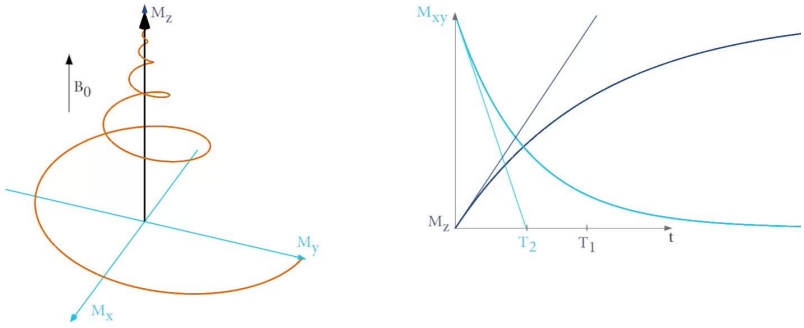

Figure 11: Visual representation of the relaxation times T-1 and T-2.

According to these two relaxation times, it is possible to have the two most common MRI sequences that are the T1-weighted and T2-weighted. In the first sequence, the TE and TR times are both short, and the contrast and brightness of the image are determined mainly by

the T1. On the other hand, in the second sequence, the TE and TR times are both longer, and the images are mainly generated according to the T2 properties of the tissue [20].

From the above considerations, it is possible to write the solutions to the Bloch equations for the Transverse magnetization and the Longitudinal magnetization [21]:

$$\begin{aligned} \vec{M}_T &= M_x\vec{e}_x + M_y\vec{e}_y \\ M_T(t) &= M_0 sin(\alpha) e^{(-i(\omega t+\phi_0)-\frac{t}{T_2})} \end{aligned} \tag{2.13}$$

$$\begin{aligned} \vec{M}_L &= M_z\vec{e}_z \\ M_L(t) &= M_0[1+(cos(\alpha)-1)e^{-\frac{t}{T_1}}] \end{aligned} \tag{2.14}$$

Where:

ω is the Larmor frequency

α is the flip angle

M_0 is the equilibrium magnetization

M_T is the transverse magnetization

ϕ_0 is the initial phase of M_T

M_L is the longitudinal magnetization

T_1, T_2 are the relaxation times

2.1.2 Hardware

An MRI and MRE hardware system is composed by four main components, which are the magnet, the gradient coils, the RF transmitter and receiver, and the computer [22].

- **The magnet**: it is usually a superconducting electromagnet inside the MRI casing. The material used is a Niobium-Titanium alloy that below the temperature of 9 K loses its resistivity. The cooling is provided by liquid helium that is pumped all around the alloy. One of the most important parts of this component is its stability, and this particular alloy allows tolerances as low as 1 p.p.m. over the volume of interest [22] which guarantees a permanent, and homogeneous B_0 magnetic field inside bore. The magnetic field B_0 is parallel to the scanner axis.
- **The Gradient Coils**: they are essential for the generation of the magnetic field in all the different directions of space, and they can be classified into two categories according to the orientation of the magnetic gradient they are generating:
  - *Maxwell Coils.* To generate the linear variation in the direction of the field, it is usually used a Maxwell coil. It consists of two coils separated by a distance d where the current is flowing in the opposite sense as shown in Figure 12:

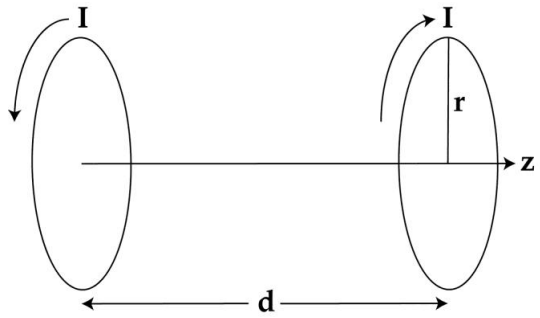

Figure 12: Z-axis production of linear field gradient through Maxwell coils.

– *Golay coils.* For what concerns the production of linear gradients along the other axis, a saddle-coil is usually the best solution. This configuration is made up of four saddles that run along the bore of the magnet to produce a linear variation in **B** in the x or y axis. A graphical representation of a double-saddle Golay coil configuration is shown in Figure 13:

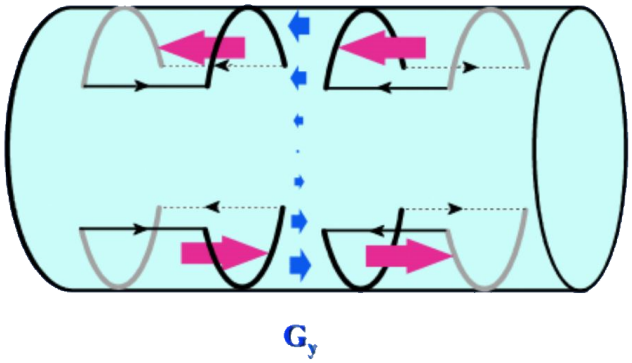

Figure 13: Double-saddle Golay coil for producing a linear field gradient along the y-axis.

- **RF Transmission and Reception**: there are many designs for transmission and reception coils, but they can be classified into two macro-categories:
  - *Surface Coil*. It is as simple as a coil with a capacitor in parallel. The inductance of the coil and the capacitance are tuned to have the same resonant frequency of the spins to be imaged. A graphical representation is shown in Figure 14
  - *Volume Coil*. It consists of several wires running along the x-axis, disposed to generate a cosine current variation around a circle. An oscillator supplies the frequency and modulates it to create a shaped pulse. A graphical representation is shown in Figure 14 below:

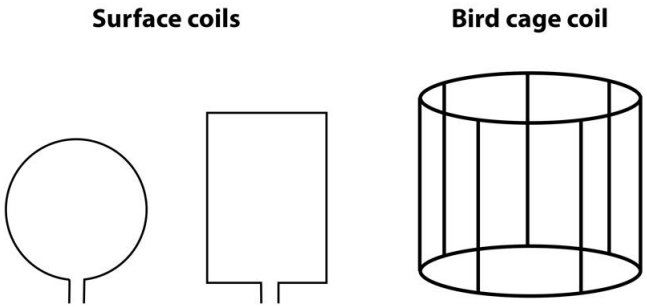

Figure 14: Surface coils (left) and volume coil in the bird cage configuration (right).

- **Computer**. It is in charge of all the scanning and control operations. These include, but are not limited to, the following:
  - Specify the shape of the gradient
  - Specify the RF waveforms
  - Specify the timing to be used
  - Pass information to the waveform generator
  - Process the digital signal for Fourier transformation
  - Display the image on a monitor

  A sketch of the system is presented in Figure 15:

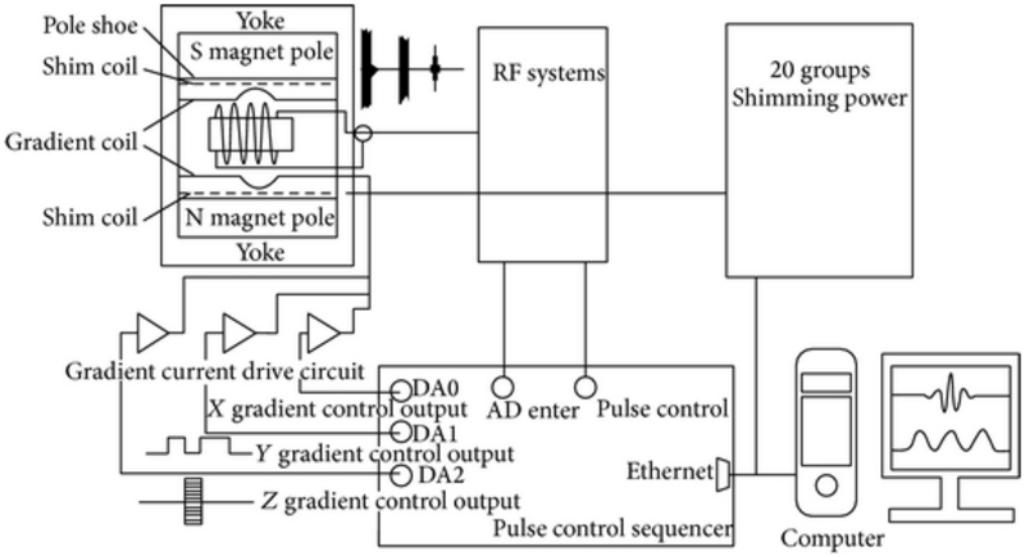

Figure 15: Sketch of the diagram of a MRI scanner.

2.1.3 Image acquisition

As with other imaging techniques, there are three different planes of interest: the axial plane, the sagittal plane, and the coronal plane. Note that the plane perpendicular to the scanner axis in MRI is the axial one [23]. The main principle of the image acquisition is the generation of space-dependent magnetic field gradients inside the magnetic resonance chamber that can create the resonance condition for the Larmor frequency only in specific areas. In general, the mathematical expression for the magnetic field is the following [24]:

$$B = B_0 + \vec{r} \cdot \vec{G} \tag{2.15}$$

Where:

B is the magnetic field along a spacial dimension

B_0 is the main magnetic field in the magnet isocenter

$\vec{r}$ is the unit vector

$\vec{G}$ is the magnetic field gradient

Note that the magnetic field is always parallel to the z-axis.

Once the transverse magnetization has been created, an induced voltage signal in the RF coil is received as a result of its precessing (MR signal) with a specific Larmor frequency equal to ω. If the magnetic field is changing, the signal is detected by other RF receiver coils as induced voltages with Larmor frequency equal to ω. The result of the application of magnetic field gradients is the spatial dependence of the Larmor frequency [25]. This dependence can be seen in the following simplified formula which expresses the resonance condition for exciting transverse magnetization in a transverse slice [5]:

$$\Omega_{RF} = \gamma B = \gamma(B_0 + zG_z) \tag{2.16}$$

Where:

Ω_{RF} is the RF pulse-frequency

z is the position of the selected slice

This equation can be inverted in order to get the position of the selected slice, which means:

$$z = \frac{1}{G_z}(\frac{\Omega_{RF}}{\gamma} - B_0) \tag{2.17}$$

Furthermore, the thickness of the selected slice (Δz) is defined as:

$$\Delta z = \frac{H}{\gamma G_z} \tag{2.18}$$

Where:

H is the RF pulse-bandwidth

Gradient and RF pulse are applied simultaneously for slice selection. Once the slice is selected, the slice position is determined by RF pulse frequency and the thickness by the RF pulse bandwidth.

The RF pulses that are sent to the system are usually sinc-type. A graphical representation of these pulses is shown in the Figure 16 below:

Figure 16: Sinc-type RF pulses in the time domain (left) and in the frequency domain (right).

The formula that rules this pulse shape in the time domain is the following:

$$\frac{sin(\pi Ht)}{\pi Ht} e^{-i\Omega_{RF}t} \tag{2.19}$$

While in the frequency domain it is simply a rectangular shape function.

2.1.4 Actuators

The actuation for the MRE system can occur in different ways. Some of the most used devices are herein summarized:

- **Piezoelectric actuators**. Because of their amagnetic property, they are mainly used in MRE applications. They consist of transducers that convert the electrical energy into mechanical one by using the piezoelectric effect [12]. There mainly two categories of

piezoelectric actuators which are stack actuators, characterized by low stroke and high blocking force, and stripe actuators, characterized by a large mechanical deflection [26]. Thanks to their simple design they do not require any lubrication. They are precise and silent, and besides, they can operate in cryogenic and vacuum environments.

- **Stepper motors**. There are different types of step-motor construction, but the most common ones are with a Permanent Magnet (PM). They are brush-less DC electric motors characterized by an inner gear that divides the full rotation into equally spaced steps. It is commonly used in an open-loop controlled system for its easiness in controlling. The main advantages of this actuation system are the low cost and maintenance, as well as the excellent start-stop response and the flexibility to work in any environment [27].

- **Electric actuators**. Besides classical electric motors that are based on the torque created by a magnetic field on a rotating shaft, there are many innovative electric motors compatible with MRI that are taking hold [28]. An example is the electromagnetic actuator presented in the Figure 17.

  The functioning is based on a ferromagnetic sphere that rolls and slides inside a cavity so to move the actuator. The system can be implemented inside the MRI system and the rotation of the actuator is regulated by the same magnetic field that makes the MR imaging possible.

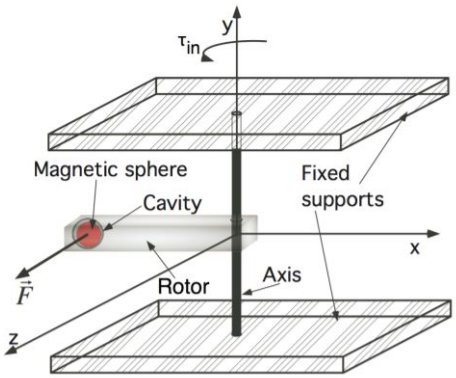

Figure 17: Innovative electric actuator scheme – compatible with MRI.

2.2 Mechanical excitation

The mechanical excitation in MRE is a fundamental part of the process, essential to detect the mechanical properties of the tissues analyzed such as elasticity, stiffness, and Poisson ratio. The excitation is applied using actuators, and the most commonly used ones are the piezoelectric actuators. The biomedical tissue can be excited in three different ways, which corresponds to the three different states of stress that can be present in a material, which are: axial, shear, and torsional. Each excitation is discussed and analyzed in the following sections considering the excitation modalities and the stress-induced. Note that considering the dimension of the phantoms used for these experiments, the mechanical model chosen for the computation of the results is the *Timoshenko-Ehrenfest beam theory* whose formulation is reported below [29][30]:

$$EI\frac{\partial^4\omega}{\partial x^4} + m\frac{\partial^2\omega}{\partial t^2} - (J + \frac{EIm}{kAG})\frac{\partial^4\omega}{\partial x^2\partial t^2} + \frac{mJ}{kAG}\frac{\partial^4\omega}{\partial t^4} = q(x,t) + \frac{J}{kAG}\frac{\partial^2 q}{\partial t^2} - \frac{EI}{kAG}\frac{\partial^2 q}{\partial x^2} \quad (2.20)$$

Where:

ω is the frequency

A is the cross section area

E is the elastic modulus

G is the shear modulus

I is the second moment of area

k is the Timoshenko shear coefficient

q(x,t) is the distributed load

m is equal to: $m = \rho A$

J is equal to: $J = \rho I$

ρ is the density of the beam material

2.2.1 Axial

The axial stress can be both compressive or tensile, and it is the quantitative expression of the internal forces acting within the beam when an axial force is applied [31]. The mathematical expression for the axial stress is the following:

$$f_a = \frac{N}{A} \tag{2.21}$$

Where:

f_a is the axial stress acting on the section

N is the compressive or tensile force

A is the cross-sectional area

For the experiments taken into account in this paper, the axial excitation is performed through an excitation ring that is connected to the center of the phantom to excite the material right at the center of the ROI. The excitation ring is then connected to a piezoelectric actuator through other plastic supports that transmit the displacement without breaking or deforming. In this case, the load is applied directly to the surface of the sample, creating a normal stress gradient along the cross-section of the phantom.

In this case the Timoshenko-Ehrenfest equation becomes the following [30]:

$$EI\frac{\partial^4\omega}{\partial x^4} + N\frac{\partial^2\omega}{\partial x^2} + m\frac{\partial^2\omega}{\partial t^2} - (J + \frac{EIm}{kAG})\frac{\partial^4\omega}{\partial x^2\partial t^2} + \frac{mJ}{kAG}\frac{\partial^4\omega}{\partial t^4} = q + \frac{J}{kAG}\frac{\partial^2 q}{\partial t^2} - \frac{EI}{kAG}\frac{\partial^2 q}{\partial x^2} \tag{2.22}$$

2.2.2 Shear

The shear stress is coplanar component of the stress on a beam cross section. The shear stress is related to the shear force by the cross sectional area according to the following mathematical formulation [32][33]:

$$\tau_s = \frac{F}{A} \tag{2.23}$$

Where:

τ_s is the shear stress

F is the applied force

A is the cross-sectional area

For the experiments taken into account in this paper, the shear stress has not been applied yet. A proper setup still needs to be prepared for this type of excitation but it can be implemented both from the previous setups and from the one described in this paper by simply modifying the orientation of the piezoelectric actuators. If the modification occurs in the previous setup, then the excitation will be applied through the excitation ring, and then to the surface of the phantom. Otherwise, if the modification is applied to the current setup, the excitation will be applied to one end of the phantom in the totality of the section.

2.2.3 Torsional

The torsional stress is shear stress produced by the couple acting on a mechanical shaft during the twisting thereof. The torsional stress for shafts with uniforms cross-section, like the ones considered in this paper, can be evaluated according to the following formula [34][35]:

$$\tau_t = \frac{T \cdot r}{J} = \frac{G \cdot \theta}{l} \tag{2.24}$$

Where:

τ_t is the Maximum Shear stress induced at the external surface by the torsion

T is the twisting moment or torque

r is the radius of the shaft

J is the polar moment of inertia

G is the shear modulus

l is the length of the shaft

θ is the angle of twist in radians on the length l

For the experiments taken into account in this paper, the torsional stress has been applied to one end of the phantom through the so-called "Mobile Support" that will be better discussed in section 4. The torque is possible thanks to two piezoelectric actuators that are operating simultaneously against the surface of the mobile support with a moment arm of approximately $15mm$.

2.3 Encoding techniques

In order perform the spacial encoding there are different techniques can be used. The first one is the phase-encoding technique that is used for the x-direction encoding, and it is based on the resolving of columns by means of the phase of M_T. A graphical representation is shown in Figure 18 below [36][5]:

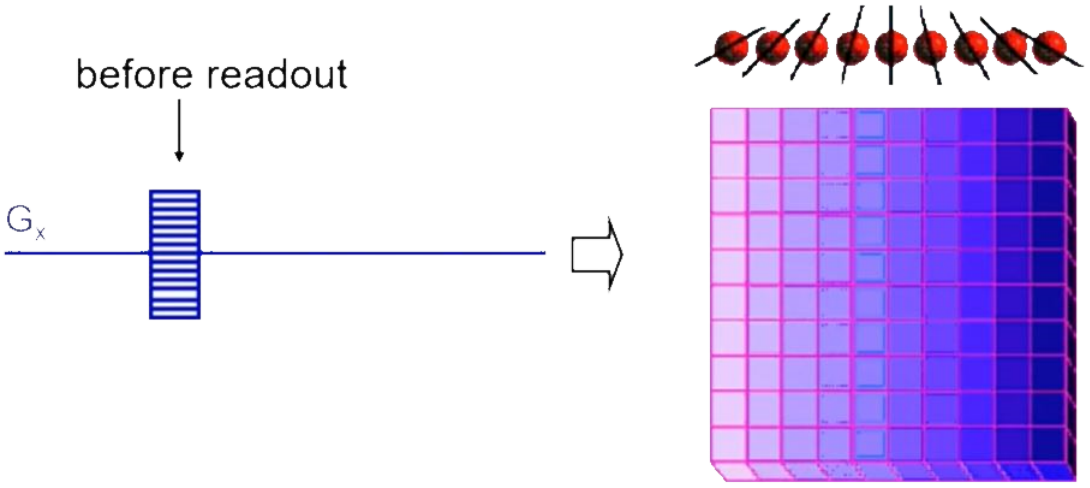

Figure 18: Resolving of columns by means of phase M_T – x-direction.

For the y-direction encoding instead, the frequency encoding technique is chosen. In this case, one specific value of the gradient is applied along the y-direction during the readout. The

y-position is then evaluated thanks to the precession frequency being present. A graphical representation is presented in Figure 19 below [5]:

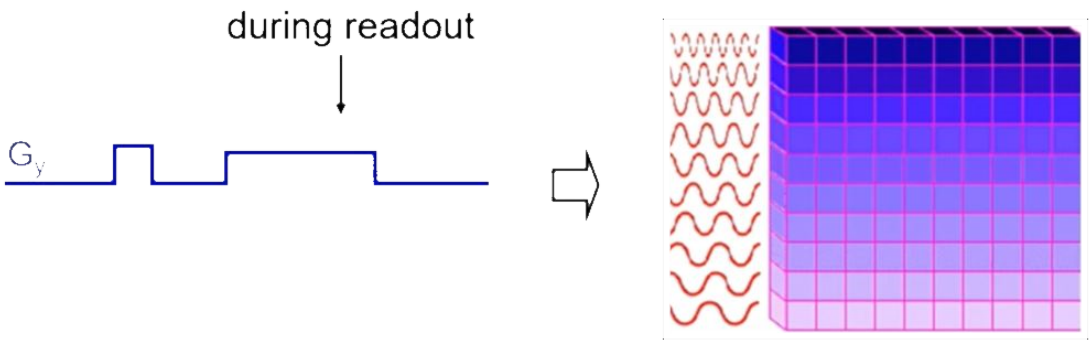

Figure 19: Resolving of rows by means of precession frequency.

The correspondent equation that put together both the phase encoding in the x-direction and the frequency encoding in the y-direction is the following:

$$S(t) = S(k_x, k_y(t)) = \int_{-\infty}^{\infty}\int_{-\infty}^{\infty} \mathbf{M}_T^*(x,y)e^{-i2\pi[k_x x + k_y y]}dxdy \tag{2.25}$$

Considering that:

$$\begin{aligned} k_x &= \frac{\gamma G_x \tau}{2\pi} \\ k_y &= \frac{\gamma G_y \tau}{2\pi} \end{aligned} \tag{2.26}$$

Where:

$\mathbf{M}_T^*$ is transverse magnetization

γ is the gyromagnetic ratio

τ is the duration of G_x

G_x, G_y are the magnetic gradients

Note that the MR signal corresponds to the 2D Fourier-Transform of $\mathbf{M}_T$ [37]. Indeed, it is right from the inverse Fourier-Transform that is possible to move from the signal (K-space) to the space domain.

A Graphical representation of the acquisition process is presented in Figure 20 below:

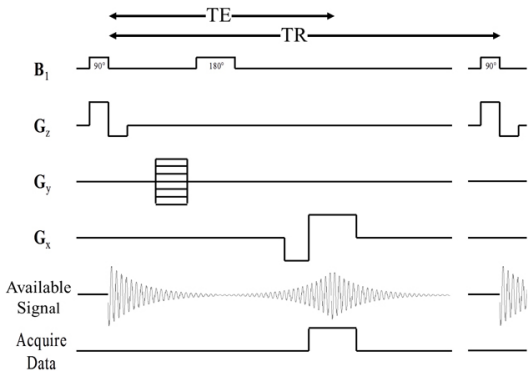

Figure 20: MR signal acquisition – schematic representation.

2.4 Wave propagation theory

The model considered for the comparison between the theoretical and the empirical results is the one of a uniaxial tensile pre-stress on axially and torsionally driven axisymmetric shear wave motion in isotropic and transversely isotropic materials [38][39]. These materials, in particular, are soft tissue cylindrical phantoms made with a polymer called $EcoFlex^{TM}$.

This sort of material is incompressible, linear elastic, and transversely isotropic. Furthermore, it presents a constant bulk modulus κ taken to be the one of the water. To describe this material, it is sufficient to use κ and three other parameters dependent by the shear and tensile moduli, respectively: $\mu_\perp$ and $\mu_\parallel$, $E_\perp$ and $E_\parallel$. Note that the subscripts indicate the orientation of the fiber direction compared to the principle direction. The additional parameters chosen are the following:

$$\phi = \frac{\mu_\parallel}{\mu_\perp} - 1 \tag{2.27}$$

$$\zeta = \frac{E_\parallel}{E_\perp} - 1 \tag{2.28}$$

Where:

ϕ is called *shear anisotropy* parameter

ζ is called *tensile anisotropy* parameter

The additional equation is given by the relationship between $E_\parallel$ and $\mu_\perp$:

$$E_{\parallel} = \mu_{\perp}(4\zeta + 3) \tag{2.29}$$

The pre-stress is now considered by introducing uniaxial initial stress parallel to the fibers of amplitude T. As a first approximation, the deformation of the pre-stress and anisotropy generation by its interplay are neglected [40][41].

During the propagation of the shear wave, it is possible to polarize the displacement into slow independent and fast independent shear wave components. These components are perpendicular to the wave propagation direction and the direction of the fiber at the same time. The equation that regulates these components are the following [41]:

$$c_s^2 = \frac{\mu_{\perp}}{\rho}(1 + \phi cos^2(\theta) + \frac{T}{2\mu_{\perp}} cos^2(\theta)) \tag{2.30}$$

$$c_f^2 = \frac{\mu_{\perp}}{\rho}(1 + \phi + \frac{T}{2\mu_{\perp}} cos(2\theta) + (\zeta - \phi) sin^2(2\theta)) \tag{2.31}$$

Where:

c_s is the slow shear wave

c_f is the fast shear wave

ρ is the density of the material where the wave is propagating

θ is the angle between the propagation and the fiber direction

Note that because the fibers are not stretched by the slow component, the relative component c_s is independent of ζ.

CHAPTER 3

STATE OF THE ART

3.1 Agilent 9.4 T

The magnet that is used to run these experiments is a superconductive electromagnet that produces a magnetic field of 9.4 T. This is an Ultra High-Field MRI system and for this reason, it involves contraindication for pacemakers, ferromagnetic implants, and neurostimulators. The low-loss helium cryostat bore is 400 mm long. Superconducting shim coils are disposed of all around it to guarantee the field shimming. The control is provided by a helium cryomonitor and an emergency quench heater control unit. The helium consumption is reduced almost to zero thanks to two cryo-refrigerators that eliminate the need for a liquid nitrogen reservoir.
The magnet is made up of multiple niobium-titanium alloy filaments with a high percentage of copper. The magnetic field is homogeneously defined over a Ø200 mm spherical volume.
The magnet is protected by a passive resistor network next to the helium reservoir. It is designed to guarantee high levels of mechanical stress and stability to ensure reliable and stable operations [42].
The cryostat is an all-welded helium vessel made in stainless steel, surrounded by an aluminium cryocooled radiation shield. The helium reservoir has a capacitance of approximately 5,000 liters, even if nominally the consumption of helium is zero. Cryomonitors are incorporate also in this case to control the level of helium and display warnings or alarms. A backup liquid

helium level probe is provided in case of failure of the first one. A picture of the system is provided here below (Figure 21):

Figure 21: Agilent 9.4 T system at the University of Illinois at Chicago.

3.2 Phantom

Nowadays it is possible to create a wide range of phantoms for biomedical experimentation. What is needed is a 3D printer to create the mold of the phantom, and then the polymer to cast inside the mold. A versatile and easy-to-use polymer, that the UIC Bioengineering laboratories are using a lot, is the $EcoFlex^{TM}$. It comes in two different parts (A and B) that need to be mixed so that the material starts to polymerize and get stable. Phantoms may differ in terms of dimension, symmetry, isotropy, and stiffness.

The phantom that has been used for the experiment is an anisotropic one with three different

layers of stiffness. The matrix of the phantom is made with $EcoFlex^{TM}$ 20 which is the softest material between all the three materials that have been used. Inside the external shell of the phantom, there are four smaller cylinders made with $EcoFlex^{TM}$ 30 which are disposed radially around the axis of the biggest cylinder. This polymer has a stiffness that is in between the matrix and the smallest cylinders. They simulate the role of the fibers inside the muscle. Inside each of these cylinders, there are four other smaller cylinders made with $EcoFlex^{TM}$ 50 which is the stiffest material between all the material used. A technical data sheet of the material is presented in Figure 22:

	Ecoflex™ 5	Ecoflex™ 00-50	Ecoflex™ 00-30	Ecoflex™ 00-33 AF	Ecoflex™ 00-20	Ecoflex™ 00-10
Mixed Viscosity (ASTM D-2393)	13,000 cps	8,000 cps	3,000 cps	3,000 cps	3,000 cps	14,000 cps
Specific Gravity (g/cc)(ASTM D-1475)	1.07	1.07	1.07	1.07	1.07	1.04
Specific Volume (cu.in./lb.)(ASTM D-1475)	25.8	25.9	26.0	26.0	26.0	26.6
Pot Life (ASTM D-2471)	1 min	18 min	45 min	45 min	30 min	30 min
Cure Time	5 min	3 hours	4 hours	4 hours	4 hours	4 hours
Shore Hardness (ASTM D-2240)	5A	00-50	00-30	00-33	00-20	00-10
Tensile Strength (ASTM D-412)	350 psi	315 psi	200 psi	200 psi	160 psi	120 psi
100% Modulus (ASTM D-412)	15 psi	12 psi	10 psi	10 psi	8 psi	8 psi
Elongation at Break % (ASTM D-412)	1000%	980%	900%	900%	845%	800%
Die B Tear Strength (ASTM D-624)	75 pli	50 pli	38 pli	38 pli	30 pli	22 pli
Shrinkage (in./in.)(ASTM D-2566)	<.001 in./in.	<.001 in./in.	<.001 in./in.	<.001 in./in.	<.001 in./in.	<.001 in./in.

Figure 22: $EcoFlex^{TM}$ data sheet.

For what concerns the dimension the phantom is 130 mm long, with a Ø35 mm diameter for the center part and a Ø45 mm diameter at the two end parts. The center part is 100 mm long, and the shoulders are 120° inclined. The inner cylinders are Ø10 mm and Ø2 mm and they run along the whole section of the phantom. A graphical representation of the phantom is shown in Figure 23:

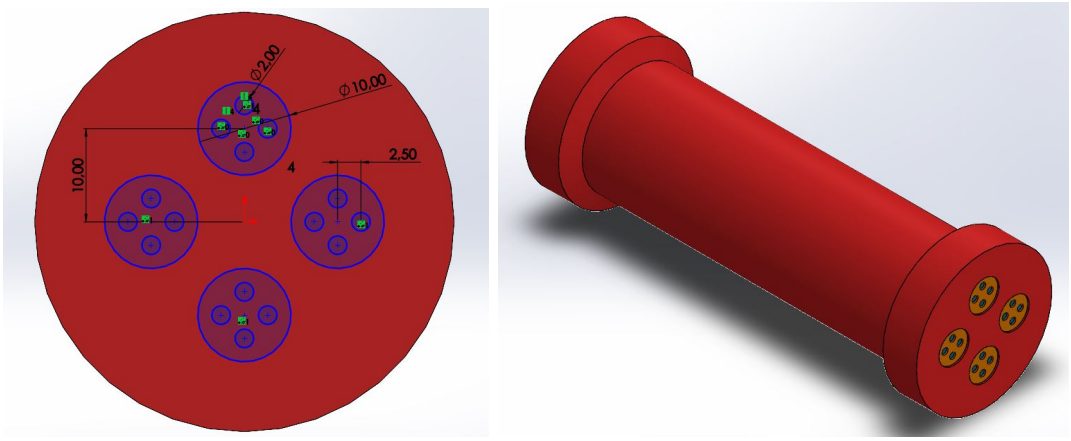

Figure 23: Phantom section with quotes (left) and prospective (right).

To create all the phantoms a plastic casting mold is created using the *Siraya*® Tech Fast material. It is an affordable resin, fast to print and cure. More details are provided in the next chapter.

3.3 3D Printer

The 3D printer that has been used for the manufacturing of the majority part of the pieces in the setup is the Photon Mono SE by Anycubic, which is shown in Figure 24. It is a Digital Light Processing (DLP) printer so it uses light to cure the project. Instead of heating and extruding a filament, it cures one layer of the project at a time using liquid resin and UV rays. At the end of this process, the print bed moves upwards to allow the next layer to be cured as well. The detail level is usually higher than Stereolithography (SLA) printing, and not heating the filaments allows a safer environment [43].

Figure 24: Photon Mono SE 3D Printer.

The technical specification are herein summarized in Table II:

TABLE II: TECHNICAL SPECIFICATION – PHOTON MONO SE BY ANYCUBIC

Technical Specifications	
System	ANYCUBIC Photon Mono SE
Operation	3.5 inch Touch Screen
Software	ANYCUBIC Photon workshop
Connectivity	USB
Technology	LCD-based SLA
Light-source (wavelength)	High-quality filament (405 nm)
XY Res.	0.051 mm 2560*16202K
Z Axis Res.	0.01 mm
Layer Res.	0.01 $\sim$ 0.15 mm
Printing Speed	MAX 80 mm/h
Rated Power	55 W
Printer Size	220mm(L)*200mm(W)*400mm(H)
Build Volume	130mm(L)*78mm(W)*160mm(H)
Material	405 nm UV Resin
Net Weight	$\sim$ 8.2kg

3.4 Viscoelastic models

Considering the excitation frequencies used for the experiments that go from $100Hz$ to $1000Hz$, rheological models are needed to approximate the complex behavior of shear modulus. A rheological model is a viscoelastic model that represents the behavior of bodies and materials

when an external force is applied [44][45].

The first model analyzed in these terms is the Linear Elastic Spring one which states that [46]:

$$\sigma = \epsilon E \tag{3.1}$$

Where:

σ is the stress

E is the modulus of elasticity

ϵ is the deformation

Furthermore, the Linear Viscous Dash-pot model is introduced, and it states that:

$$\sigma = \eta \dot{\epsilon} \tag{3.2}$$

Where:

$\dot{\epsilon}$ is straining velocity

η is the viscosity of the material

From the combination of these models, it is possible to create other models such as the Springpot-Model. Between all the linear viscoelastic models, this is the one that better describes the distortion that is measurable within biological tissues, and it guarantees a good

reproducibility [47]. It is based on two independent parameters, and the viscosity (η) is given as a constant. A graphical representation of the model is presented in Figure 25 below [5]:

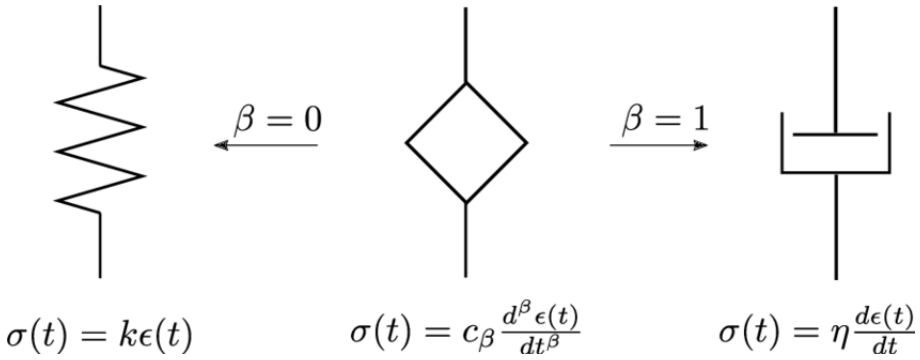

Figure 25: Sketch of the fractional element-springpot.

The mathematical formulation for the complex shear modulus is the following:

$$G(\alpha) = \mu^{1-\alpha}(i\omega\eta)^{\alpha} \tag{3.3}$$

Where:

μ depends on the viscoelastic connectivity

α depends on the matrix geometry

$G(\alpha)$ is the complex shear modulus

CHAPTER 4

METHODS AND MATERIALS

4.1 Background

Before starting the design of the setup, some research and studies on the previous experiments' configurations have been performed. In particular, it has been taken into account the last setup created in the lab during the previous year. This setup was created to excite axially a phantom to study the propagation of axisymmetric waves through the material. It was already innovative compared to the other ones because of its half-tube configuration, while the previous ones preferred a full-tube configuration. The system used for the image recognition was the same Agilent 9.4T system used for the experiments on the torsional excitation. The design is presented in Figure 26 below:

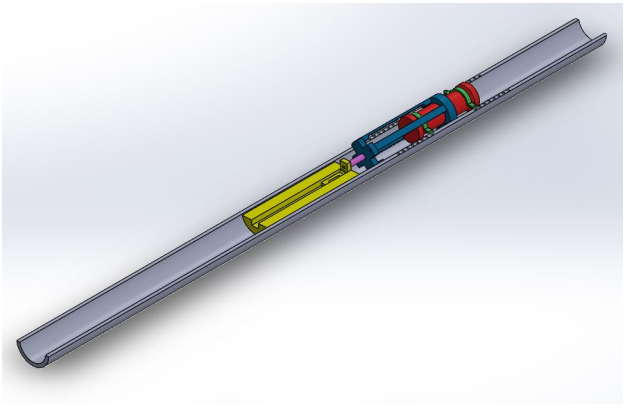

Figure 26: Representation of a previous axial excitation setup.

The phantom is held by two clamps that are connected to the holding tube. The excitation is possible thanks to the blue x-shape structure that connects the piezoelectric actuator to the center of the phantom. On the other side of the piezoelectric motor, there is an L-shape holder which maintains the motor stable, gives inertia to the system, and avoids vibration of any type. The elongation to the phantom is performed by moving the clamps on the holding tube and securing them to the structure with M4 screws.

To move from this setup to a new one able to excite torsionally the phantom, some critical aspects have been analyzed and modified. First of all, the gripping system of the phantom with the clamps was not suitable, and to perform a torsional excitation it would have been needed a redesign. Secondly, the mounting of the system was complicated because of the excitation ring. Additionally, this last component needed to be changed every time according to the elongation of the phantom which affects the section area. Finally, the phantom needs to be supported to rotate inside the holding tube considering its sticky surface and low stiffness.

The design of the new setup tried to solve all these problems, by keeping the best solutions out of the previous one. The holding tube has not changed, and the phantom dimensions are the same, even if the inner geometry is different.

For what concerns the material it is important to notice that, because of the strong magnetic field inside the magnetic resonance, no metallic or magnetic material, in general, is allowed in the setup. For this reason, all the materials that will be discussed in the next sections are completely amagnetic.

Also, the material has changed from the previous setups, to the new one. Previously, the

material that has been used for the structural part of the setup was VeroClear by $Stratasys^{TM}$. The majrity part of the pieces 3D printed for this setup are in $Siraya^{®}$ Tech Blu. It is an easy to use tough resin suitable for making functional parts. The main mechanical properties of the two materials are presented in the Table III and Table IV below:

TABLE III: VEROCLEAR BY STRATASYS^{TM} MECHANICAL PROPERTIES

Mechanical Properties	
Tensile Strength	50 MPa
Shore D	83
Young's Modulus	2000 MPa
Elongation At Break	10%
Impact test with 140 kg	20 J

TABLE IV: SIRAYA® TECH BLU MECHANICAL PROPERTIES

Mechanical Properties	
Tensile Strength	39 MPa
Shore D	85
Young's Modulus	1500 MPa
Elongation At Break	25%
Impact test with 140 kg	14 J

4.2 Holding Tube

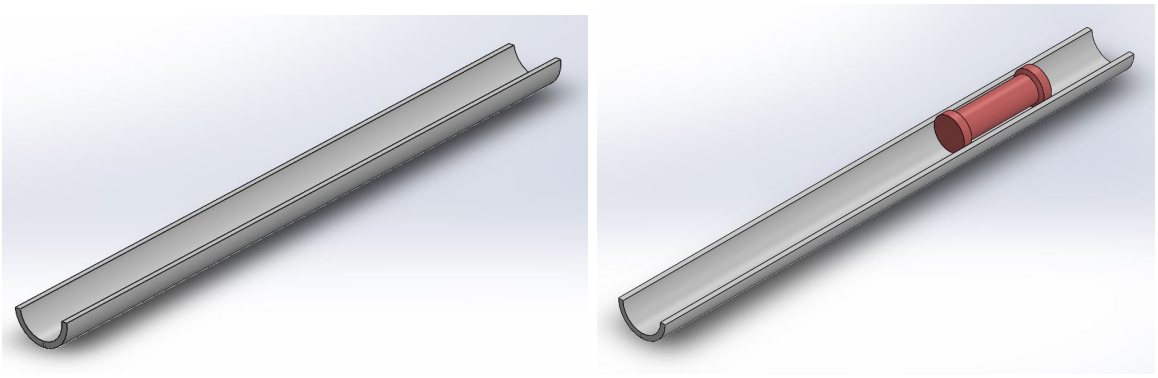

Figure 27: Holding tube (left) and assembly (right) representation.

The base of the entire system is the holding tube shown in Figure 27. The role of this part is to support the other parts and guarantee that the phantom is located exactly in the Region Of Interest (ROI) of the Agilent. The Outer Diameter (OD) is 70 mm to guarantee a 1 mm gap on each side of the tube and the magnet. The Inner Diameter (ID) is 56 mm to fit every component in it. The length of the holding tube is 700 mm, and the cut is performed parallel to the longitudinal axis 3 mm below the horizontal diameter defining the half of its cross-section. On the cross-sectional surface at one end of the tube, there is a Ø3 mm threaded to host a 506 mm long rod screwed on top. The purpose is to locate the holding tube in the 1206 mm bore and have the center of the phantom in the ROI of the magnetic resonance. On the borders of

the tube, a series of drilled holes are performed to fix both the phantom and the fix support clamps, which will be illustrated further in this chapter.

This component has been taken from previous setups, and for this reason it is made in VeroClear by $Stratasys^{TM}$.

4.3 Fix Support

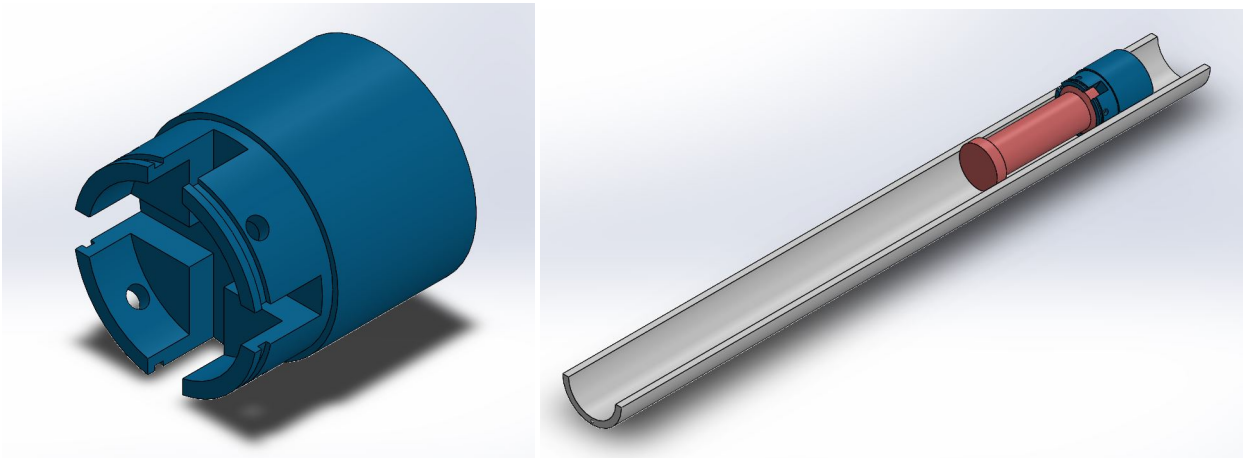

Figure 28: Fixed support (left) and assembly (right) representation.

The fixed support shown in Figure 28 is made up of two ends: one that is facing the phantom and the other one that represents the end of the inner-tube setup. The first one is 22 mm long, and it is hallowed to host the phantom embossment. The 12 mm hallow is the same length as the phantom gripping fixture, as well as the Ø45 mm ID matches perfectly the end section of

the phantom. In this way, the support can enfold the phantom completely. A secondary 19 mm cross-hallow is performed to facilitate the phantom extraction process. Each side of the cross-shape is 10 mm in width. The OD of this first end is 53 mm, and some additional features are added to this outer surface. A 2.5 mm groove all around the support to fit a plastic cable tie and ensure that the phantom is fixed to the support. For further experimentations, four peripherical holes are added around the outer surface to fit four M6 screws. These may be used in case the muscle tested does not provide a homogeneous shape to fix the sample to the fixed support. The other end of the fixed support is a simple 40 mm long solid cylinder with a Ø56 mm diameter to fit in the holding tube. Along the outer surface of this end, the support clamps will be connected to the holding tube as described later in this chapter.

This component has been 3D printed using the *Siraya*® Tech Blu resin described previously.

4.4 Mobile Support

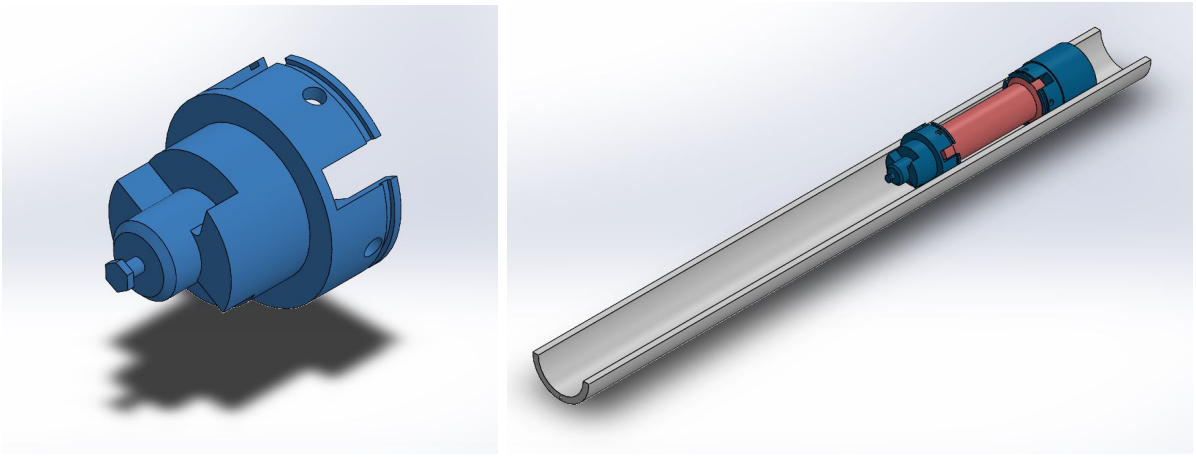

Figure 29: Mobile support (left) and assembly (right) representation.

The mobile support shown in Figure 29 is made up of two ends: one that is facing the phantom and the other one that is connected to the stabilizer. Like the fixed support, the first one is 22 mm long, and it is hallowed to host the phantom embossment. The 12 mm hallow is the same length as the phantom gripping fixture, as well as the Ø45 mm ID matches perfectly the end section of the phantom. In this way, the support can enfold the phantom completely. A secondary 19 mm cross-hallow is performed to facilitate the phantom extraction process. Each side of the cross-shape is 10 mm in width. The OD of this first end is 53 mm, and some additional features are added to this outer surface. A 2.5 mm groove all around the

support to fit a plastic cable tie and ensure that the phantom is fixed to the support. For further experimentations, four peripherical holes are added around the outer surface to fit four M6 screws. These may be used in case the muscle tested does not provide a homogeneous shape to fix the sample to the mobile support. The other end is made up of a first 25 mm extruded cylinder with a Ø39 mm diameter and two 10 mm flanges with an extension of 60°. One of the walls of these flanges is radial to the circumference, while the other one is 45° inclined with respect to the radial direction. On this second wall, there is a Ø4 mm hole to fit the piezoelectric motor for both of the two flanges. The design of this second wall takes into account the perpendicular contact between the piezoelectric actuator and the flanges. A second Ø20 mm cylinder is then extruded for 18 mm from the base of the previous one to ensure the stabilizer and the mobile support are concentric. The end of this second cylinder is rounded, considering it is designed to fit inside the stabilizer to create a mechanical coupling with a backlash so that the mobile support can rotate inside the stabilizer. At the end of this second cylinder, there is a screw to connect the wire that is responsible for the pre-load of the system. The wire and its function will be further discussed later in this chapter.

This component has been 3D printed using the *Siraya*® Tech Blu resin described previously.

4.5 Stabilizer

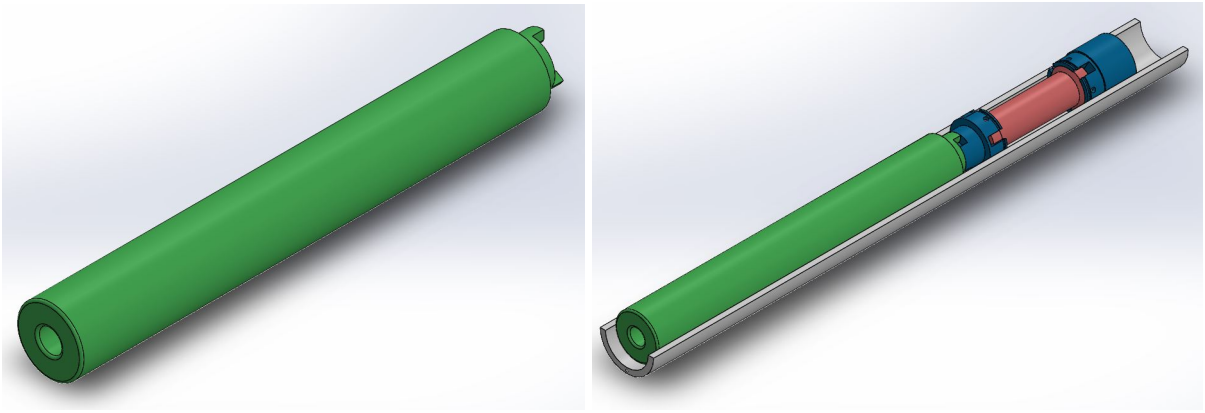

Figure 30: Stabilizer (left) and assembly (right) representation.

The role of the stabilizer Figure 30 is to give support to the piezoelectric actuators by adding inertia to the system. Because of its length, the manufacturing process of the part required to split it into two different components and then fixing them together. The two parts of the stabilizer will be called Tube and End Part and are better described in the next sections.

4.5.1 Tube

The tube shown in Figure 31 is a 400 mm long hollow cylinder with a Ø56 mm OD, and a Ø24 mm ID. The reason for the hollow is to let the wire pass through it and reach the screw at the end of the mobile support. In this way, the preload on the phantom can be parallel to its axis.

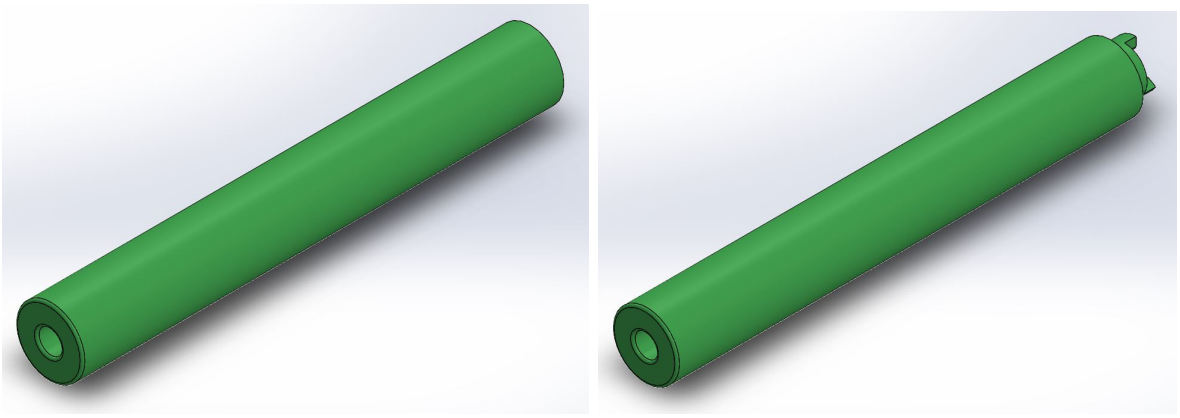

Figure 31: Tube (left) and stabilizer (right) representation.

The material used for the Tube of the Stabilizer is *Delrin*® Acetal Homopolymer. It is polymer that perfectly replace metal for its high strength and stiffness properties. At the same time it combines the high mechanical properties with a low-friction and high-ware resistance. The material has been mixed and cast inside a 3D printed casing made with *Siraya*® Tech Fast. The main mechanical properties of the *Delrin*® acetal homopolymer are presented in the Table V:

TABLE V: DELRIN® ACETAL HOMOPOLYMER MECHANICAL PROPERTIES

Mechanical Properties	
Tensile Strength	75 MPa
Shore D	89
Young's Modulus	3100 MPa
Elongation At Break	30%
Izod Impact Notched	1.0 $^{ft\ lb}/_{in}$

4.5.2 End Part

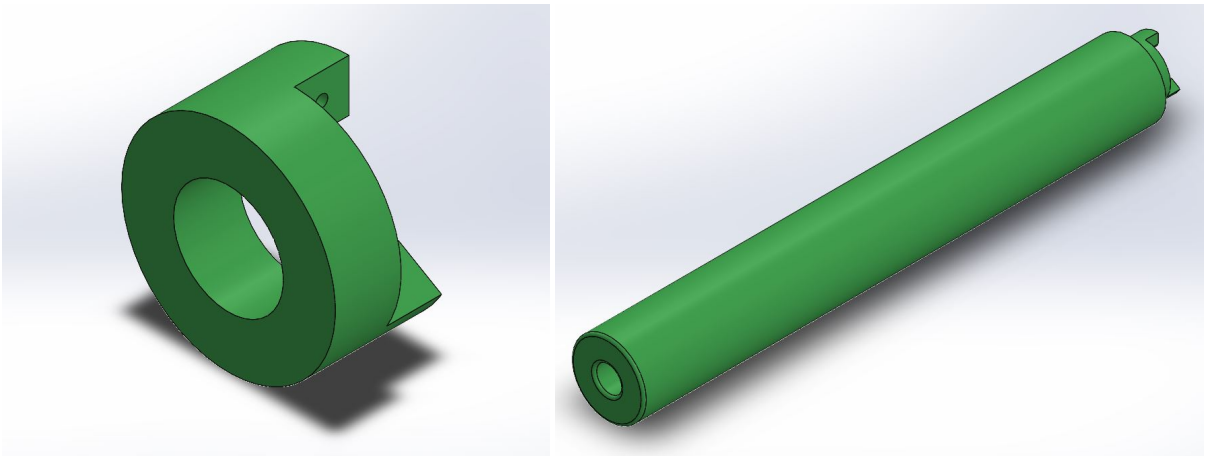

Figure 32: End Part (left) and stabilizer (right) representation.

On the end that is facing the mobile support the stabilizer, there is the end part Figure 32. It is another extruded hollow cylinder with a Ø39 mm OD, a Ø20 ID, and a length of 12 mm. This is the hollow where the shaft of the mobile support is fitting to make the two parts concentrical. On top of this hollow cylinder, there are again two flanges that are extruded for 10 mm. The walls of the flanges this time are both radial to the circumference and they extend for a 60° angle.

This component has been 3D printed using the *Siraya*® Tech Blu resin described previously.

4.6 Piezoelectric actuators

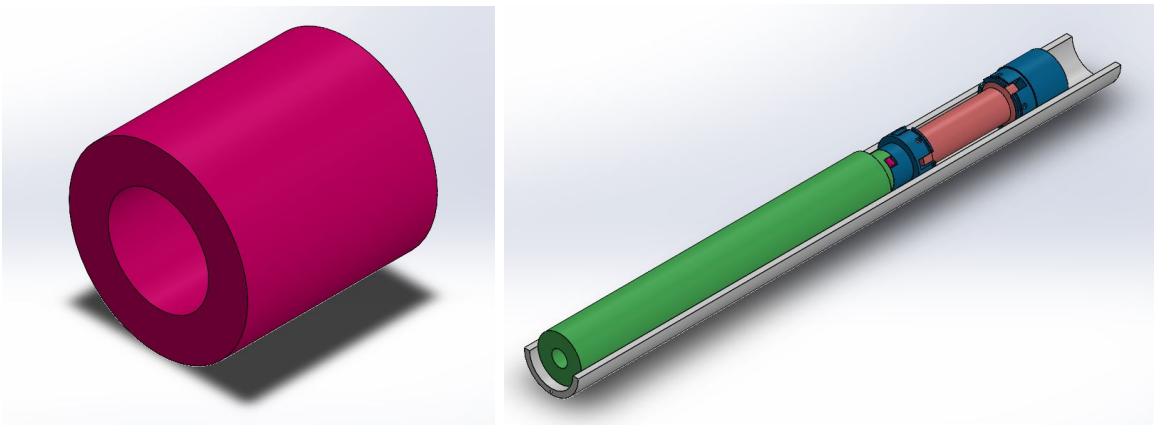

Figure 33: Piezoelectric actuator (left) and assembly (right) representation.

The piezoelectric actuators chosen are $PICMA^{®}$ Stack Multilayer Ring Actuator P-080. The model chosen for this setup is the P-080.311. The appearance of these actuators is shown in the figure below in Figure 34. They can be represented as hollow cylinders with a Ø8 mm OD, a Ø4.5 mm ID and a length of 8.5 mm. The travel range is nominally 5.5 μm. These actuators connect the flange of the stabilizer, and the one of the mobile support.

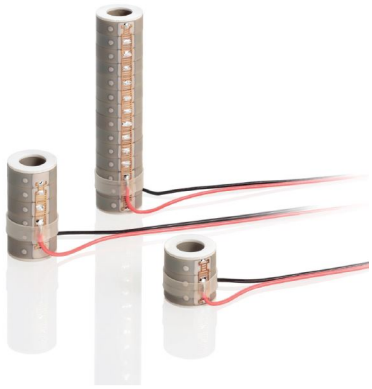

Figure 34: P-080 actuators by $PICMA^{®}$.

In the setup, two piezoelectric motors are used, one for every pair of flanges. The inner hole is used for positioning purposes and not for any preload in this case. The cylinders are fixed to the stabilizer, and by elongating they are pushing the mobile support in a clockwise direction, creating a torque over the level of the radius of the circumference. Further specifications can be found in Figure 35:

	P-080.311	P-080.341	P-080.391	Unit
Dimensions OD × ID × L	8 × 4.5 × 8.5	8 × 4.5 × 16	8 × 4.5 × 36	mm
Nominal travel range	5.5 ±20 %	11 ±20 %	25 ±10 %	µm
Blocking force	800	825	850	N
Stiffness	145	75	34	N/µm
Electrical capacitance	0.86	1.7	4.0	µF
Resonant frequency	135 ±20 %	85 ±20 %	40 ±20 %	kHz

Figure 35: P-080 data sheet.

4.7 Phantom clamps

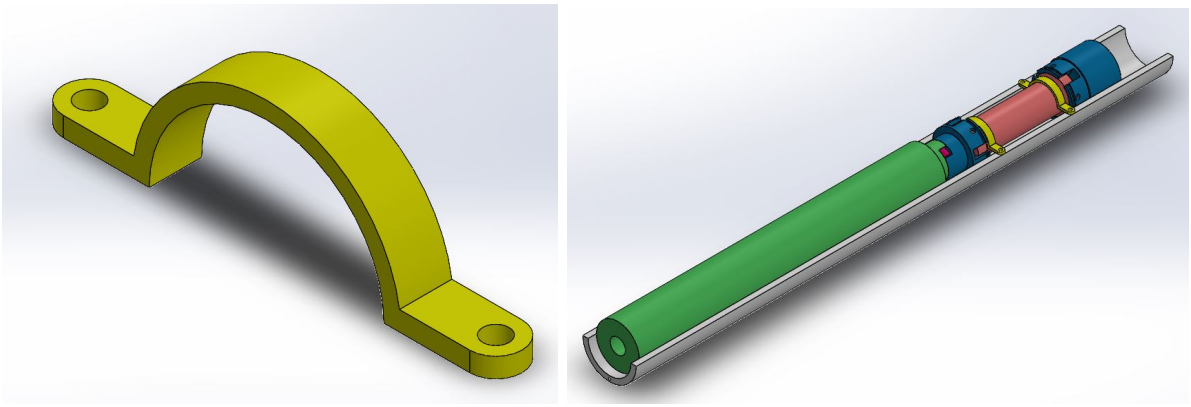

Figure 36: Phantom clamp (left) and assembly (right) representation.

Even if not strictly necessary for this setup, herein are presented the phantom clamps. Accordingly to the new gripping systems, this component is not necessary, but in the design phase, it has been considered anyway in case the fixed and mobile support would have not been sufficient. The role of this structure is the fix the phantom to the holding tube. The clamp is made up of a double arc with an inner radius of 17.9 mm and an outer one of 20.5 mm. The total length of the clamp is equal to the total length of the half tube, which is 70 mm. The width of the clamp is 8 mm, and the two holes have a Ø4 mm diameter.

This component has been 3D printed using the *Siraya*® Tech Blu resin described previously.

4.8 Support clamps

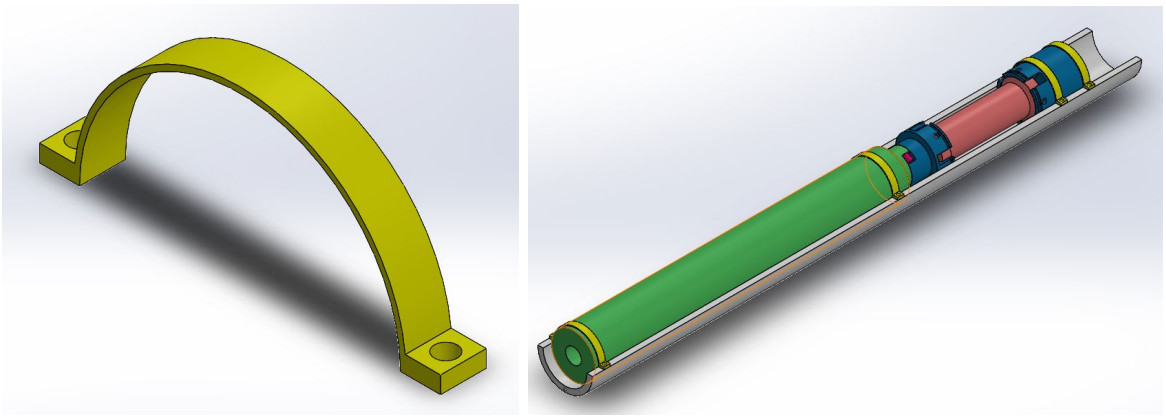

Figure 37: Support clamp (left) and assembly (right) representation.

More important for this setup are the support clamps. The design is similar to the phantom clamps, but these ones are fixing the fixed support and the stabilizer to the holding tube, instead of the phantom. Considering the high frequency used for the experiment the support clamps on the stabilizer are not essential, but for safety reasons they have been implemented in any case. The clamp is made up of a double arc with an inner radius of 28 mm and an outer one of 29 mm. The total length of the clamp is equal to the total length of the half tube, which is 70 mm. The width of the clamp is 8 mm, and the two holes have a Ø4 mm diameter.
This component has been 3D printed using the *Siraya*® Tech Blu resin described previously.

4.9 Wire and Weights

Figure 38: The nylon wire (left) and the lead weights (right) used for the setup.

The wire and the lead weights are two fundamental components for the preload of the phantom. When applying a preload the phantom is elongated and it is possible to study how the propagation of the waves inside the material changes according to the elongation of the sample. The wire used for this purpose is a nylon monofilament with a Ø.3 mm diameter. The weights are made of lead, which is a-magnetic so it can fit inside the Agilent room. There are different sizes of weights and these are: 1.05oz, 0.68oz, 0.48oz, 0.35oz, 0.25oz, and 0.17oz.

CHAPTER 5

RESULTS AND DISCUSSION

5.1 Preliminary testing

Before running experiments inside the MRI system, some preliminary testing is required. The aim is to verify the correct functioning of the setup and to have some prediction of the results. For this reason a Scanning Laser Doppler Vibrometry (SLDV) has been used to assess the movement of the piezoelectric actuators, as well as the alignment of the different components in the setup. Here in the Figure 39 the stabilizer and the piezoelectric actuators are shown:

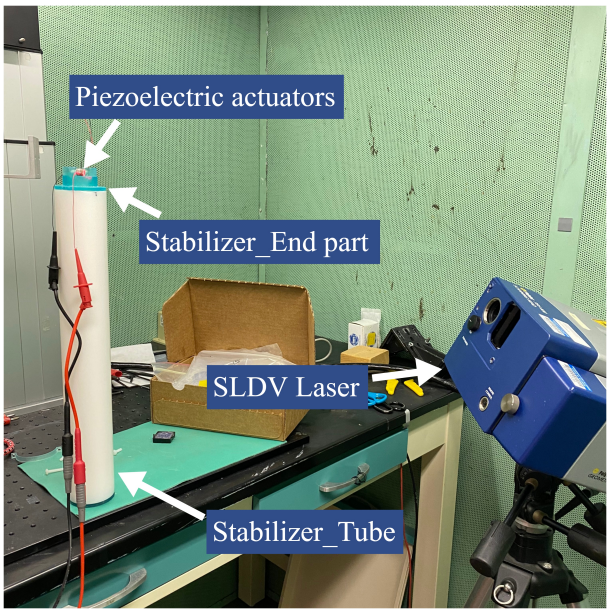

Figure 39: Piezoelectric inspection setup with SLDV system.

To guarantee the correct alignment between the piezoelectric actuator and the stabilizer, an M4 grub screw has been used for each actuator.

After assembling all the components together, a main criticism came out. It was related to the surface of contact between the piezoelectric actuator and the mobile support. Figure 40 shows the coupling between the two components:

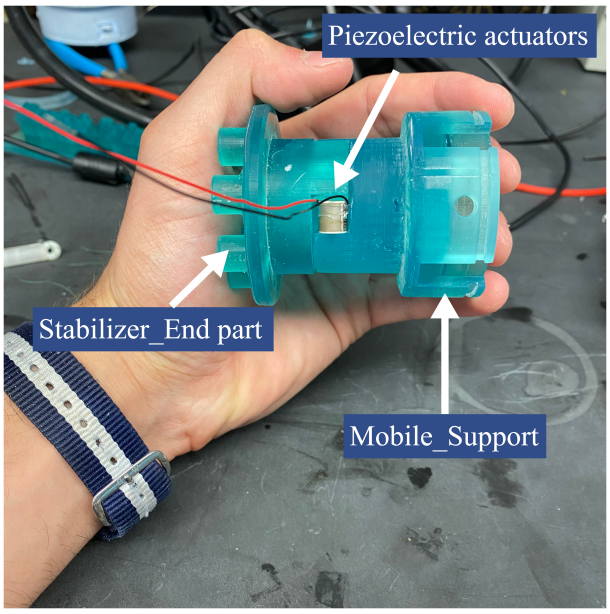

Figure 40: Coupling between the Stabilizer_End part and the Mobile Support.

The contact between the two components was not occurring at the same way for both the piezoelectric actuators because of the tolerances of the pieces. For this reason one of the two

contact areas has been sanded, and super glue has been applied to it, in order to guarantee the entire surface of the piezoelectric actuator to take part in the force generation.

The final configuration of the setup for the SLDV testing is herein presented (Figure 41):

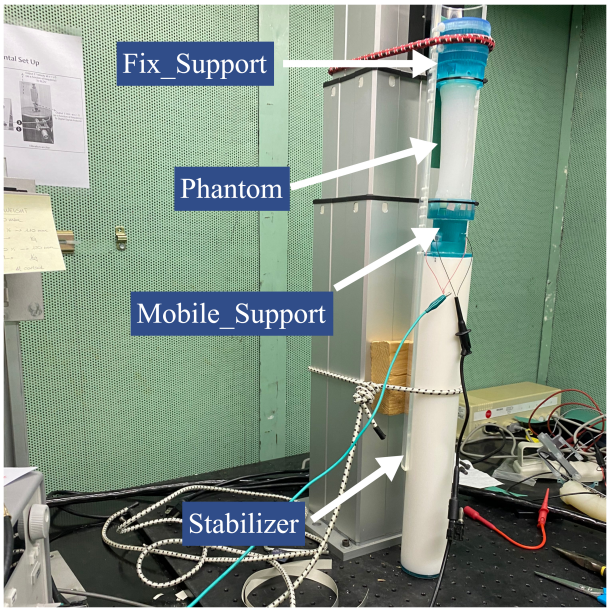

Figure 41: Vertical configuration of the setup for SLDV experiments.

Considering the necessity of pre-stressing the phantom, it has also been necessary to evaluate the Young's modulus of the material. Because of the three layers of anisotropy, the Elastic modulus has been evaluated both experimentally and theoretically, on the base of the volume occupied by each layer inside the phantom.

Experimentally, the end part of the mobile support has been attached to a bucket fulfilled with different weights and step by step it has been computed the Hooke diagram Figure 42 considering the engineering curve, since the section is kept constant. Here in Table VI the experimental data.

TABLE VI: EXPERIMENTAL DATA TO EVALUATE YOUNG'S MODULUS IN THE PHANTOM

Force [N]	0	2.94	4.39	4.74	5.93	6.89	7.97	9.19	10.02	10.43
σ [kPa]	0	0.764	1.14	1.232	1.552	1.79	2.07	2.387	2.603	2.711
ϵ	0%	2%	2.9%	3.3%	5.2%	6%	6.8%	8.2%	9.2%	10%

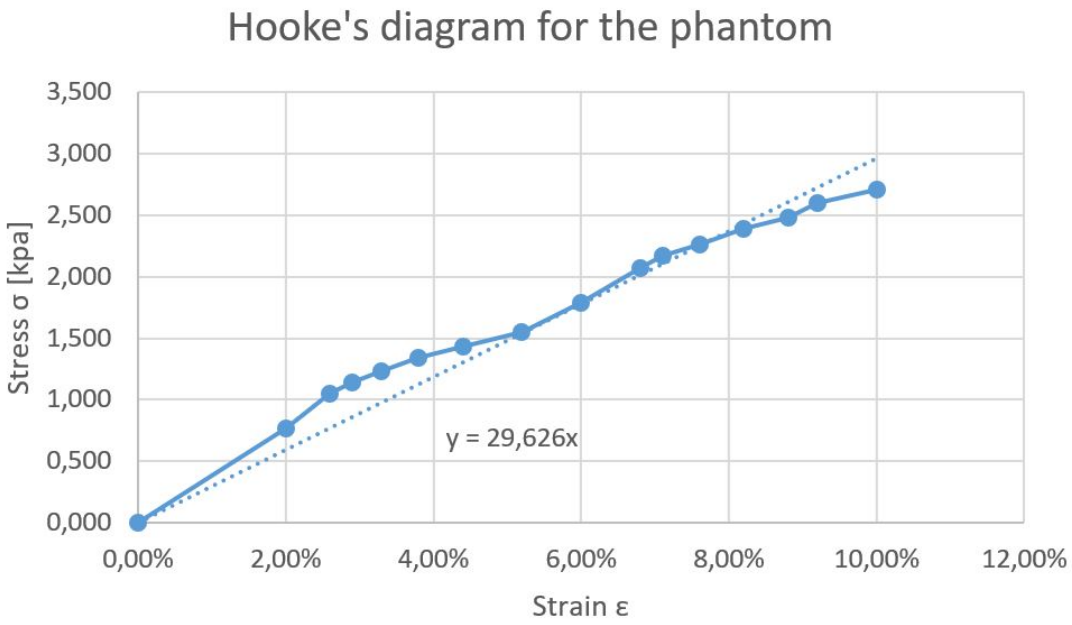

Figure 42: Hooke's engineering curve $\sigma - \epsilon$ for a phantom with three layers of anisotropy.

Theoretically, it has been used the weighted average on the volume of the layers and the formula comes out to be:

$$E = \frac{E_1V_1 + E_2V_2 + E_3V_3}{V_1 + V_2 + V_3} = 8.76\ psi = 0.0604\ MPa \tag{5.1}$$

Where:

E_1, E_2, E_3 are the Young's moduli of the three layers respectively

V_1, V_2, V_3 are the volumes of the three components respectively

E is the theoretical Young's modulus of the phantom

The two results are slightly different between each other, but both of them in the range of acceptability given by the data sheet of the material. Considering the interaction between the layers, the shape of the phantom, and the method used for the theoretical evaluation of the parameter, the experimental value has been chosen for further evaluations.

$$E = 0.0296\ MPa \tag{5.2}$$

5.2 SLDV testing

The goal of the SLDV testing is to verify and quantify the mechanical excitation before the setup is tested inside the MRI system. To do so, the Doppler shift of the reflected beam is acquired, and by knowing the frequency of the emitted one, it is possible to evaluate the vibration on the surface.

The SLDV is based on the Laser Doppler Vibrometry (LDV). This is a technique used to measure the distance between objects, and it is based on the Doppler effect. The Doppler effect consists in the changing of frequency of a wave caused by relative movement of the observer, or the source [48]. The reason for this effect is that the source of the waves is relatively moving towards the observer or opposite to it, and the successive wave is emitted in a position closer or further to the observer which causes a shift in the wave frequency [49].

There are different steps to complete before scanning the surface of the phantom and these include focusing the laser on the surface, measuring the distance between the laser and the surface, calibrate the laser and set the scanner parameters. These parameters include the

bandwidth of the wave, the shape, and the frequency. For these experiments, sinusoidal waves have been used with a range of frequency of 200 $Hz - 1000$ Hz. To guarantee a reliable result without being in overtime with the acquisition, the bandwidth for the frequencies below 500 Hz has been chosen to be 0.0004 MHz, with a Sample Frequency of 1.024 kHz, a Sample of 1000 ms and a Resolution of 1 Hz. On the other hand, for the frequencies above 500 Hz, it has been chosen a bandwidth of 0.001 MHz, with a Sample Frequency of 2.56 kHz, a Sample of 400 ms and a Resolution of 2.5 Hz. The above mentioned parameters have been chosen according to the Nyquist theorem that states the following:

$$R_{max} = 2B \log_2 M \tag{5.3}$$

Where:

R_{max} is the maximum data rate

M is the discrete level of the signal

B is the bandwidth

Sometimes the Nyquist theorem can also be re-written with the Shannon formulation, which introduces the signal power:

$$R_{max} = B \log_2(1 + \frac{S}{N}) \tag{5.4}$$

Where:

S is the signal power

N is the noise power

In general, these theorems suggest the user to use a sampling frequency that is at least two and a half times the frequency of the generated signal [50].

The first experiment that has been tried is the torsional one, with a vertical configuration. The result of the test, as well as a image of the configuration is shown in Figure 43.

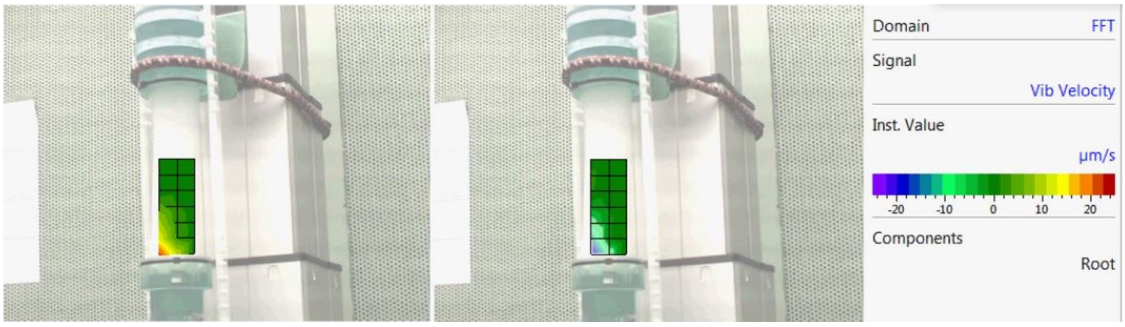

Figure 43: SLDV torsional experiment with vertical configuration - 300 Hz - 0% elongation.

The results are satisfying in terms of type of movement expected, but the resultant displacement from this actuation system is not sufficiently high to be detected from the MRI system. For this reason different frequencies and voltages have been tried to increase this displacement, arriving until the breakup of one of the piezoelectric actuator, and still the displacement was

not enough. In fact, the maximum displacement achievable can be evaluated according to the following formula:

$$u_{max} = \frac{v_{max}}{2\pi f} = 0.01\mu m \tag{5.5}$$

Where:

u_{max} is the maximum displacement

v_{max} is the maximum velocity according to the empirical results

To detect a displacement inside the MRI system, a displace of at least 1 μm is required. For this reason the following configuration has been set aside for further developments, and the axial configuration has been tested. Below the result of the experiment (Figure 44):

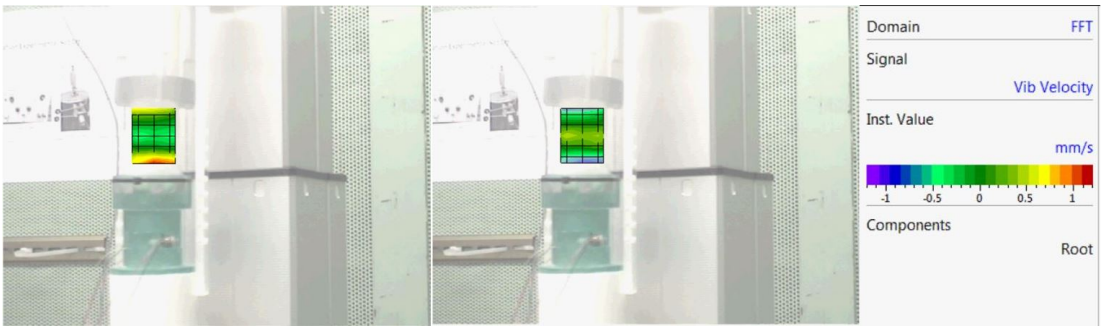

Figure 44: SLDV axial experiment with vertical configuration - 300 Hz - 0% elongation.

It can be verified with Equation 5.5 that, in this case, the displacement is sufficiently high to be detected by the MRI system. From this result, different frequencies and pre-stress conditions

have been tested using the axial excitation.

Additionally, to apply the pre-stress with the weights as the setup was intended to, the configuration has been rotated from vertical to horizontal. A graphical representation of the horizontal setup, as well as an image of the propagation of the waves is proposed in Figure 45:

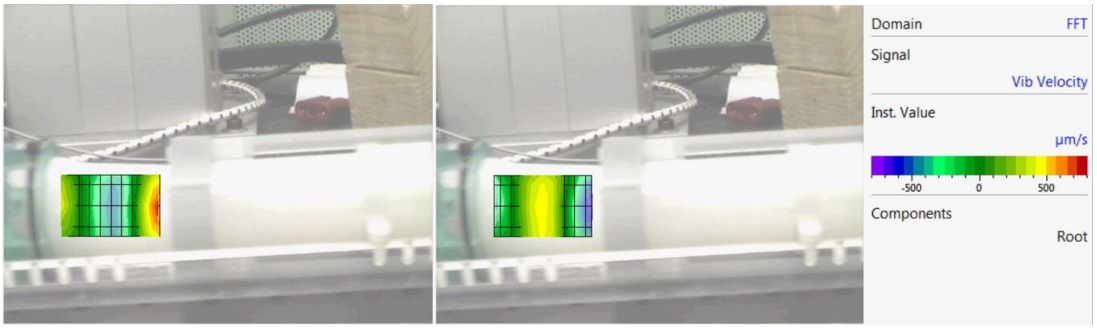

Figure 45: SLDV axial experiment with horizontal configuration - 300 Hz - 0% elongation.

The first results that have been obtained by simply exporting the resultant graphs from the SLDV software appeared confused and not uniform over the six different frequencies. The scale is not uniform and the waves are not easily visible. The color map exported from the software is the following (Figure 46):

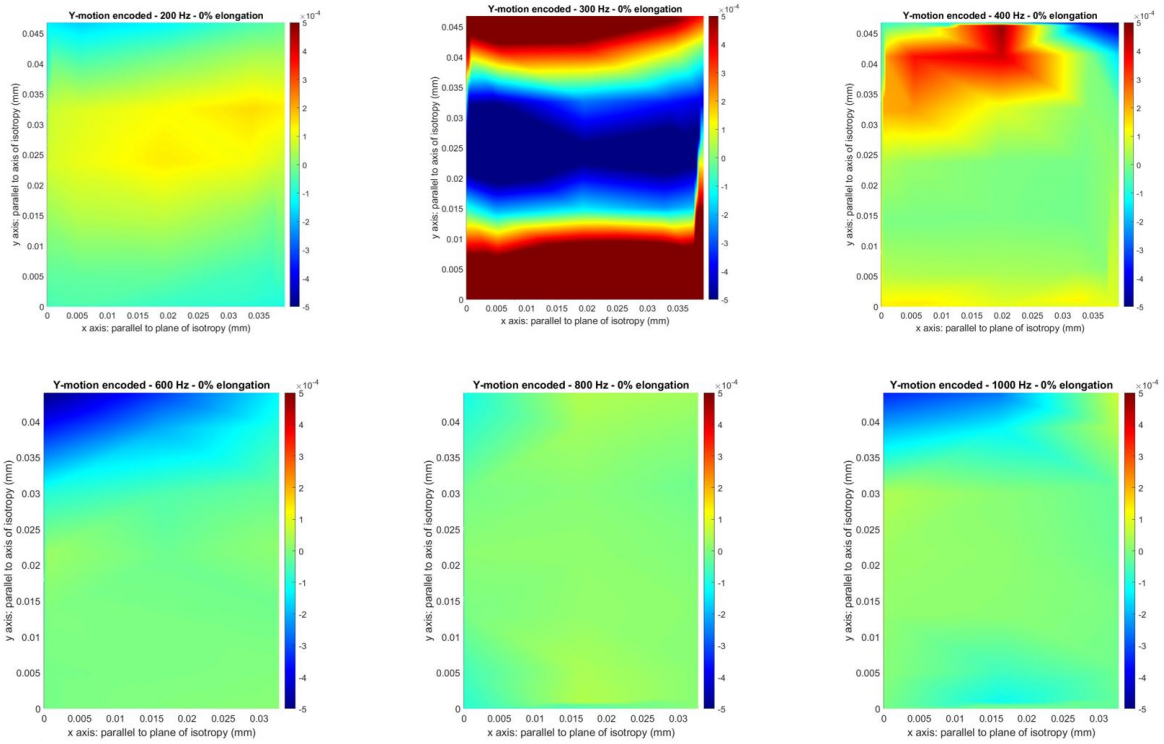

Figure 46: Color maps for SLDV axial experiments with vertical configuration - Frequencies 200 Hz, 300 Hz, 400 Hz, 600 Hz, 800 Hz, 1000 Hz - 0% elongation.

Therefore, to give a better graphical representation in a 2D domain without using the evolution of the wave over the time, the average of the values has been considered and the 3D motion has been transformed into a 2D wave. Here below a comparative graph for every frequency is provided. Every graph contains the results for the most significant frequencies

which are 300 Hz (Figure 47), 400 Hz (Figure 48), 500 Hz (Figure 49), 600 (Figure 50), and 800 Hz (Figure 51).

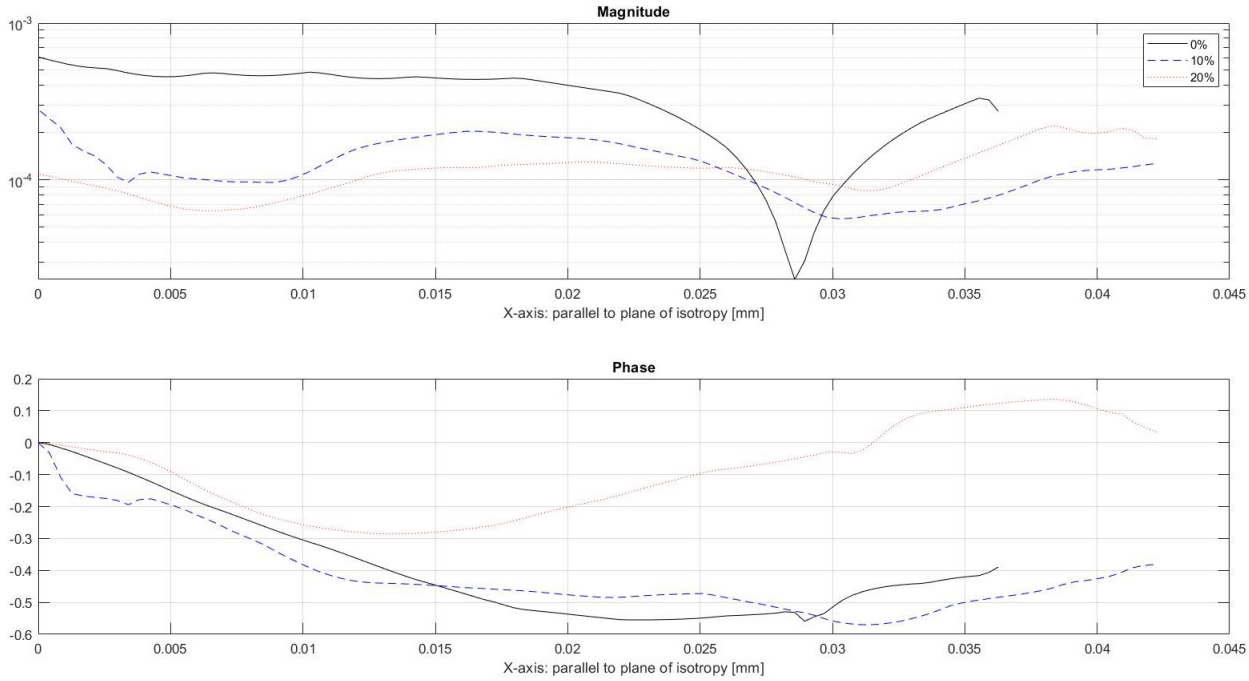

Figure 47: Horizontal axial excitation for different strain levels at 300 Hz.

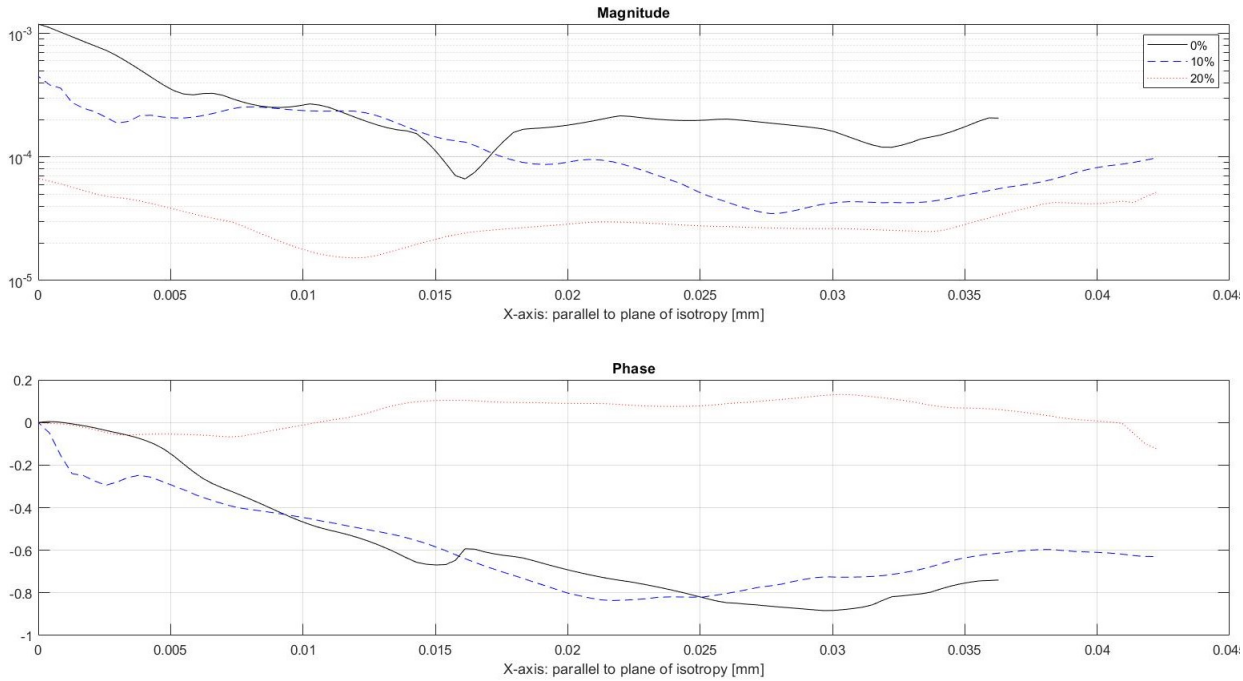

Figure 48: Horizontal axial excitation for different strain levels at 400 Hz.

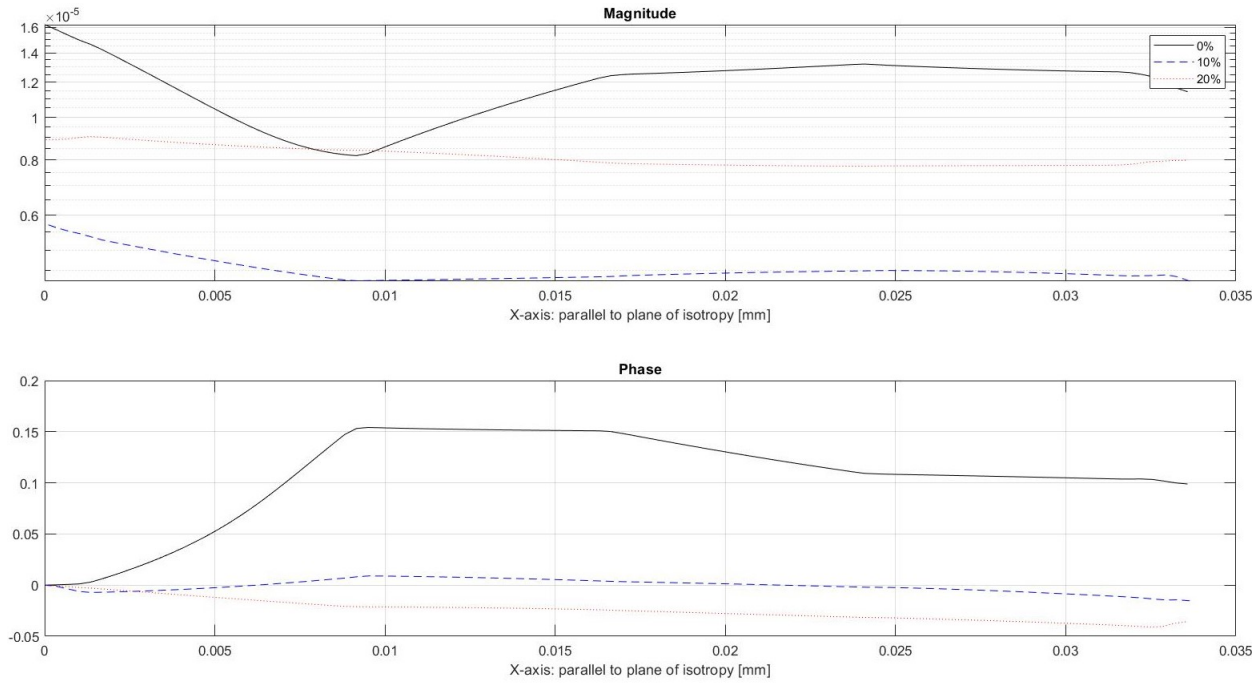

Figure 49: Horizontal axial excitation for different strain levels at 500 Hz.

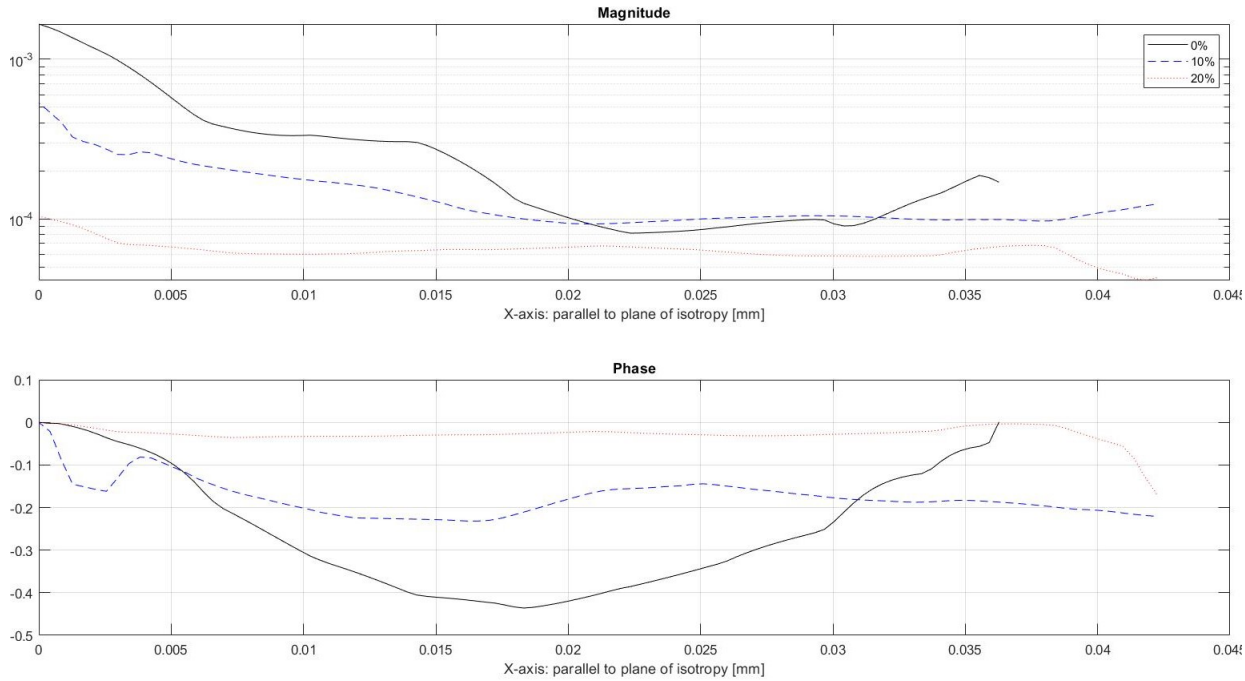

Figure 50: Horizontal axial excitation for different strain levels at 600 Hz.

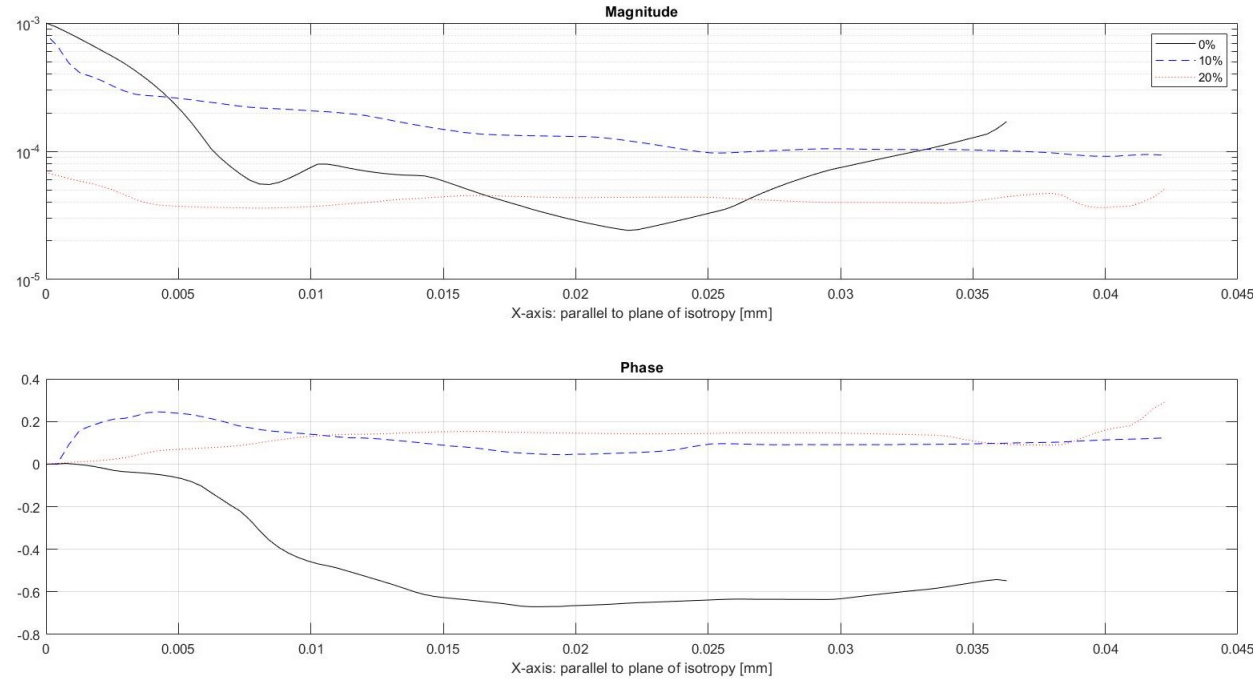

Figure 51: Horizontal axial excitation for different strain levels at 800 Hz.

From the above mentioned graphs, the main wave properties can be estimated. A table with all the results for the different frequencies is herein proposed (Table VII). The attenuation is directly proportional to α, and this latter parameter is evaluated from the initial slope of the magnitude. The wavelength λ is taken from the phase, reconstructing the distance between two peaks from the first cycle of the sinusoidal wave. The wave speed is evaluated accordingly, using the formula $v = \lambda f$.

TABLE VII: WAVE PROPERTIES EXCTRACTED FROM SLDV FOR DIFFERENT FREQUENCIES AND PRE-STRESS CONDITIONS

Wave Properties				
Frequency	Elongation	Alpha (α)	Wave length (λ) [mm]	Wave speed (v) [$^m/_s$]
300 Hz	0%	0.03	33	9.9
	10%	0.004	29	8.7
	20%	N/A	N/A	N/A
400 Hz	0%	0.161	30	12
	10%	0.083	28	11.2
	20%	0.005	N/A	N/A
500 Hz	0%	0.001	38	19
	10%	N/A	31	15.5
	20%	N/A	N/A	N/A
600 Hz	0%	0.117	37.5	22.5
	10%	0.071	21	12.6
	20%	0.013	N/A	N/A
800 Hz	0%	0.15	30	24
	10%	0.47	100	80
	20%	N/A	N/A	N/A

5.3 COMSOL Multiphysics® Simulation

COMSOL Multiphysics® is a multiphysics simulation software. Thanks to this tool, it is possible to simulate the behavior of the phantom when an axial or torsional displacement is applied. The first step in the computation of the model is defining the geometry and the parameters that are needed for the simulation. The phantom with three different layers of anisotropy has been defined.

After that, the boundary conditions are imposed and in this case, both of the ends of the phantom have been set to *fixed* and the displacement is applied to the half section of the phantom. Even if this situation is not optimal for the torsional case, it allows to monitor the propagation of the waves in both the direction and to make a direct comparison between the torsional and the axial case. The boundary condition between the two halves of the phantom has been set to Dirichlet boundary condition to guarantee the continuity of the solution. Finally, the displacement application has been divided in two steps, one to pre-stress the phantom (if needed) and another one to apply the torsional or axial displacement. Here below an example of the Von Mises stress configuration for the torsional case with no elongation and a frequency of 400 Hz (Figure 52):

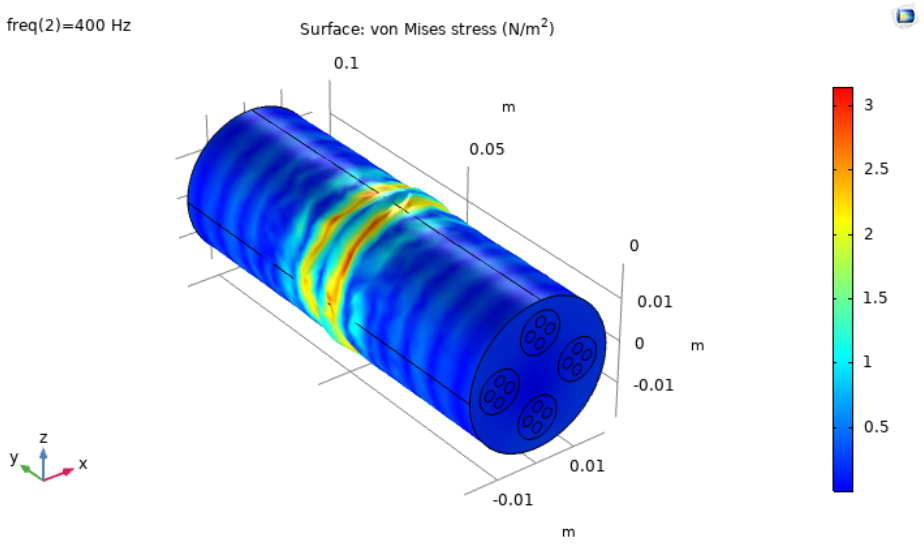

Figure 52: Von Mises stress for torsional excitation - 400 Hz - 0% elongation.

The harmonic displacements imposed are equal to $11.6E^{-6} \cdot x\ [mm]$ in the z direction and $-11.6E^{-6} \cdot z\ [mm]$ in the x direction to create the torque. The total displacement on the cross-sectional area of the phantom are then displayed below (Figure 53, Figure 54, Figure 55):

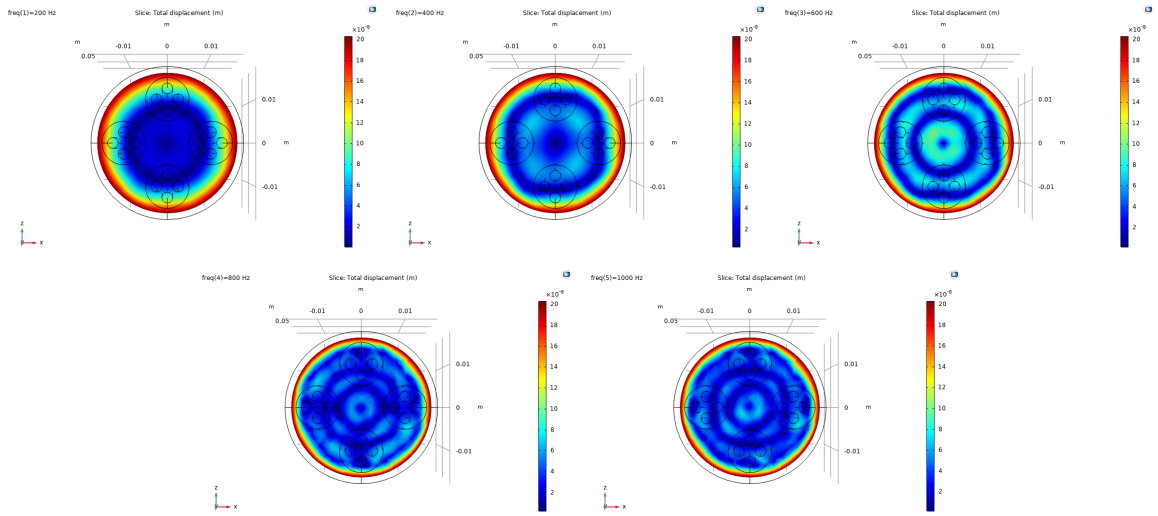

Figure 53: Total displacement on the cross-sectional area for torsional excitation - from left to right 200 Hz, 400 Hz, 600 Hz, 800 Hz, 1000 Hz - 0% elongation.

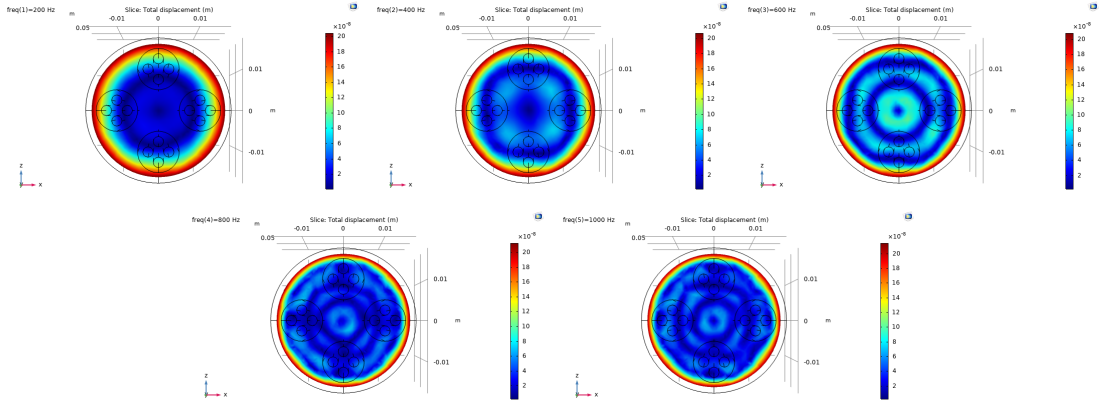

Figure 54: Total displacement on the cross-sectional area for torsional excitation - from left to right 200 Hz, 400 Hz, 600 Hz, 800 Hz, 1000 Hz - 10% elongation.

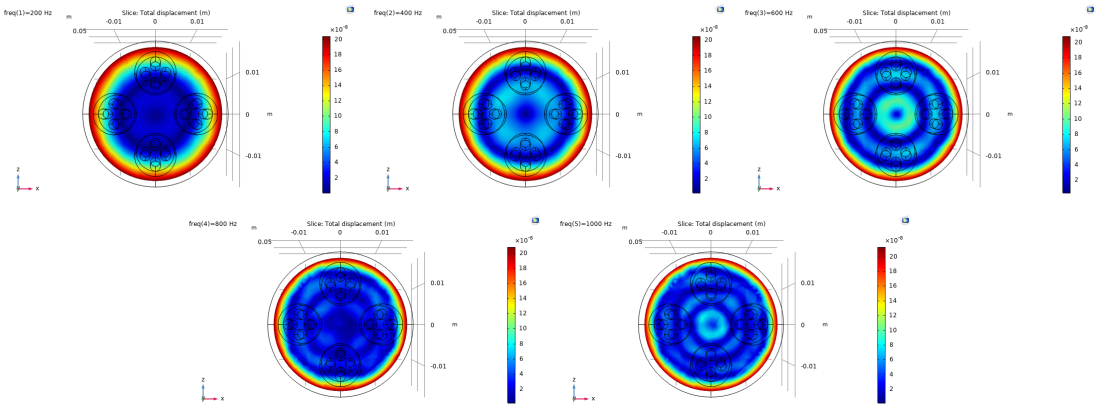

Figure 55: Total displacement on the cross-sectional area for torsional excitation - from left to right 200 Hz, 400 Hz, 600 Hz, 800 Hz, 1000 Hz - 20% elongation.

Additionally, the same computation measures has been performed for the axial case. The Von Mises stress configuration for the torsional case with no elongation and a frequency of 400 Hz is displayed here below (Figure 56):

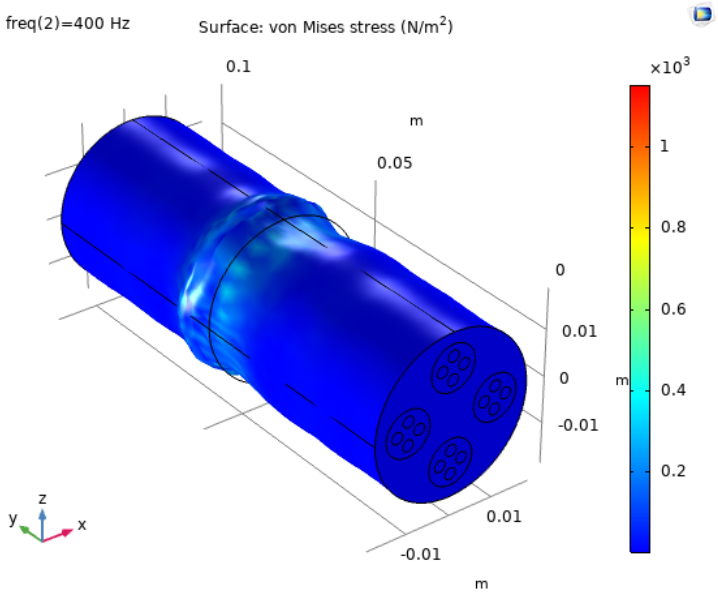

Figure 56: Von Mises stress for axial excitation - 400 Hz - 0% elongation.

The harmonic displacement imposed is equal to $11.6E^{-6}$ $[mm]$ in the y direction to create the torque. The total displacement on the cross-sectional area of the phantom are then displayed below (Figure 57, Figure 58, Figure 59):

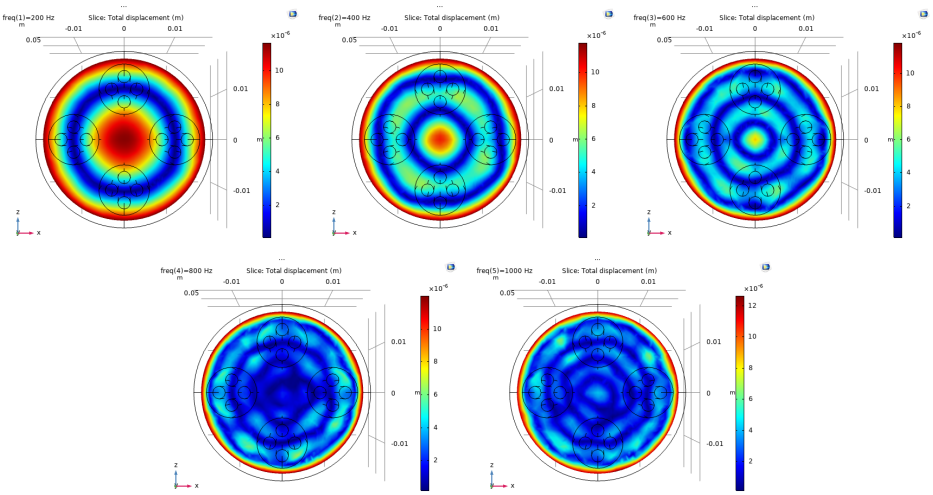

Figure 57: Total displacement on the cross-sectional area for axial excitation - from left to right 200 Hz, 400 Hz, 600 Hz, 800 Hz, 1000 Hz - 0% elongation.

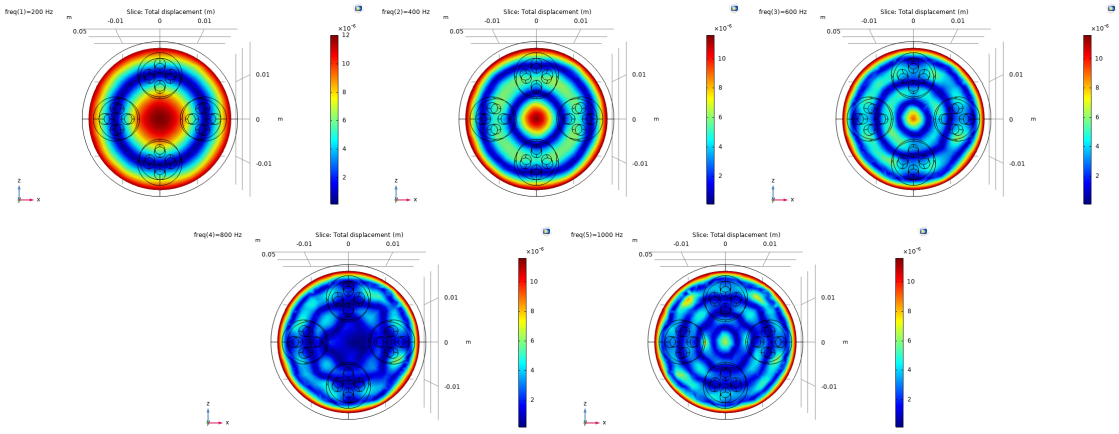

Figure 58: Total displacement on the cross-sectional area for axial excitation - from left to right 200 Hz, 400 Hz, 600 Hz, 800 Hz, 1000 Hz - 10% elongation.

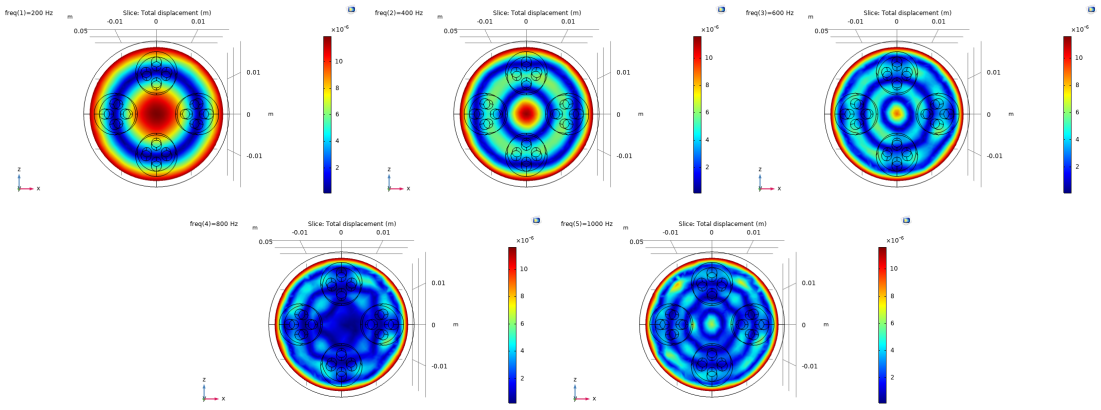

Figure 59: Total displacement on the cross-sectional area for axial excitation - from left to right 200 Hz, 400 Hz, 600 Hz, 800 Hz, 1000 Hz - 20% elongation.

5.4 Agilent testing

The Agilent testings have been conducted in accordance to the safety guidelines to guarantee the harmlessness of the setup for the people in the environment and for the technology itself [51]. Once the magnet is predisposed for the study, the modus operandi to obtain the MR images is the following:

1. Running a *scout* command to verify the correct alignment of the phantom inside the coil. The pulse sequence used is the *gems* with the parameters summarized in Table VIII

TABLE VIII: SCOUT PARAMETERS FOR THE PULSE SEQUENCE: *GEMS*

Scout parameters for the *gems* pulse sequence	
read_dim	64
phase_dim	1
read_FOV	4
phase_FOV	4
TR	MIN
TE	MIN
Number of slices	3
Slide thickness	2 [mm]
Slide spacing	1 [mm]

2. Running a *MRI scan* to obtain the axial and sagittal sections of the phantom. The pulse sequence used is the *fsems* with the parameters summarized in Table IX

TABLE IX: MRI PARAMETERS FOR THE PULSE SEQUENCE: *FSEMS*

MRI parameters for the *fsems* pulse sequence	
read_dim	128
phase_dim	1
read_FOV	4
phase_FOV	4
TR	1.2 [s]
TE	MIN
Number of slices	20
Slide thickness	1 [mm]
Slide spacing	1 [mm]

3. Running a *MRE scan* to obtain the elastography images of the sample. The pulse sequence used is the *sems_slimo_mre* with the parameters summarized in Table X

TABLE X: MRE SCAN PARAMETERS FOR THE PULSE SEQUENCE: *SEMS_SLIMO_MRE*

MRE scan parameters for the *sems_slimo_mre* pulse sequence	
read_dim	64
phase_dim	64
read_FOV	4
phase_FOV	4
TR	1.6 [s]
TE	MIN
Number of slices	20
Slide thickness	1 [mm]
Slide spacing	1 [mm]

The results for every frequency and strain conditions are now presented, starting from the lower frequency and no strain conditions. After that a discussion regarding the comparison between the experimental results and the theoretical one is inserted.

The results obtained for 600 Hz and no strain conditions are presented below (Figure 60, Figure 61):

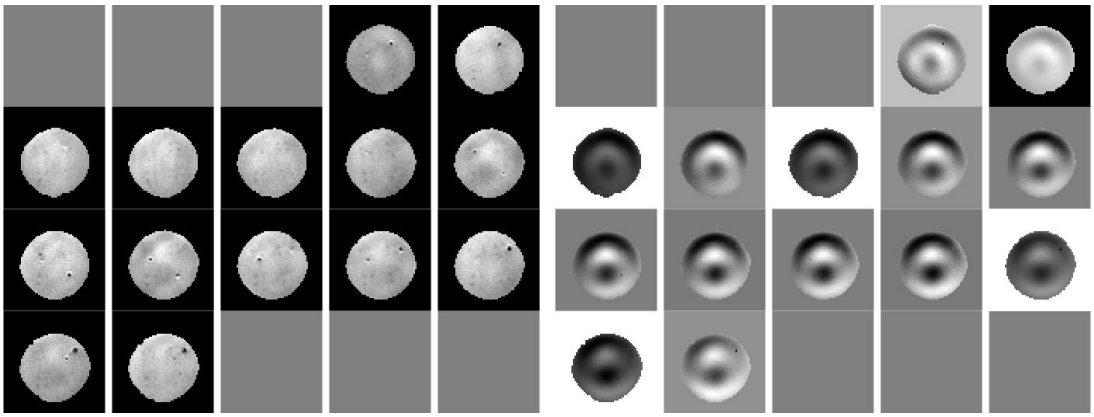

Figure 60: Magnitude (left) and Phase (right) axial cross-sectional sequence of images for 20 layers - 600 Hz - 0% elongation.

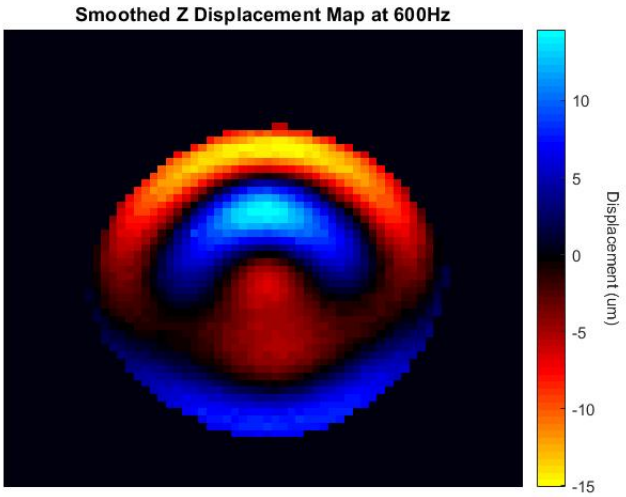

Figure 61: Z displacement map - 600 Hz - 0% elongation.

The results obtained for 600 Hz and 10% strain condition are presented below (Figure 62, Figure 63):

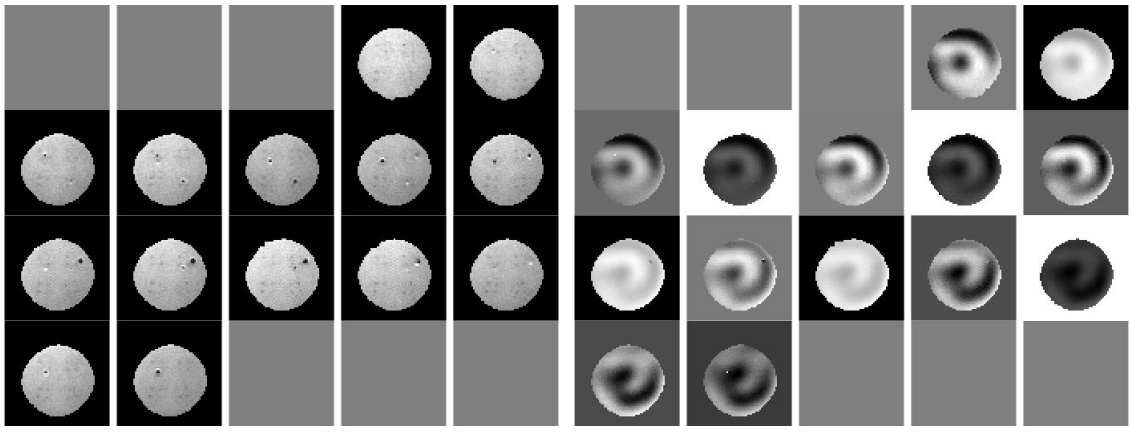

Figure 62: Magnitude (left) and Phase (right) axial cross-sectional sequence of images for 20 layers - 600 Hz - 10% elongation.

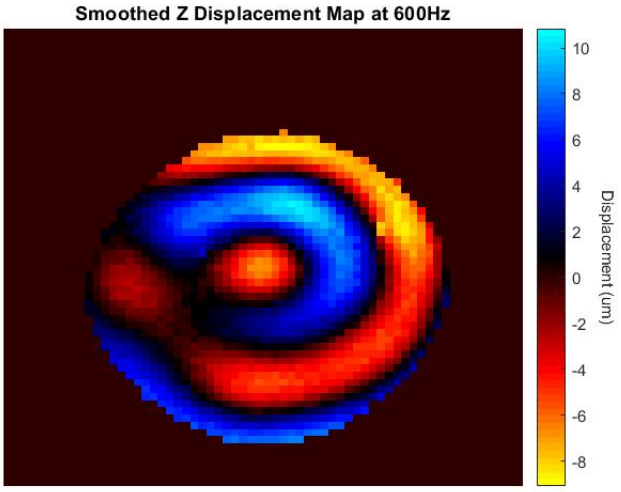

Figure 63: Z displacement map - 600 Hz - 10% elongation.

The results obtained for 800 Hz and no strain conditions are presented below (Figure 64, Figure 65):

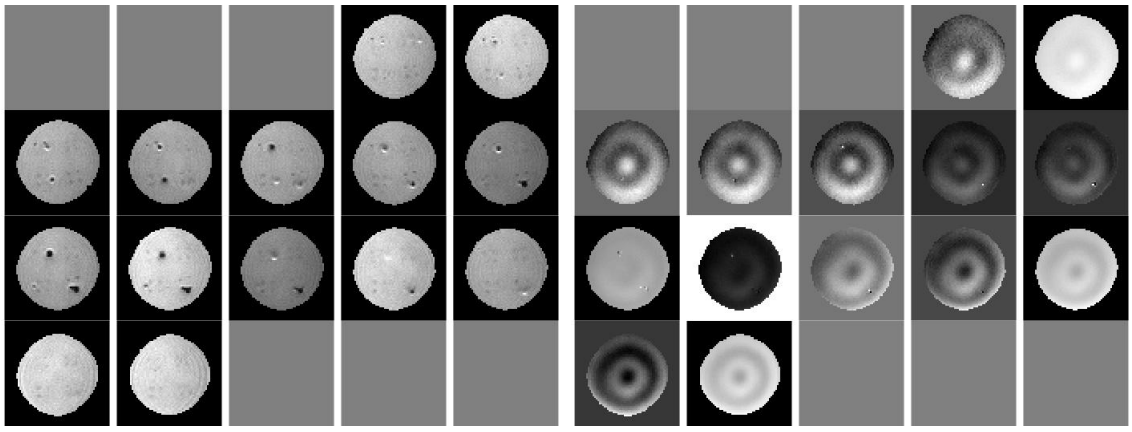

Figure 64: Magnitude (left) and Phase (right) axial cross-sectional sequence of images for 20 layers - 800 Hz - 0% elongation.

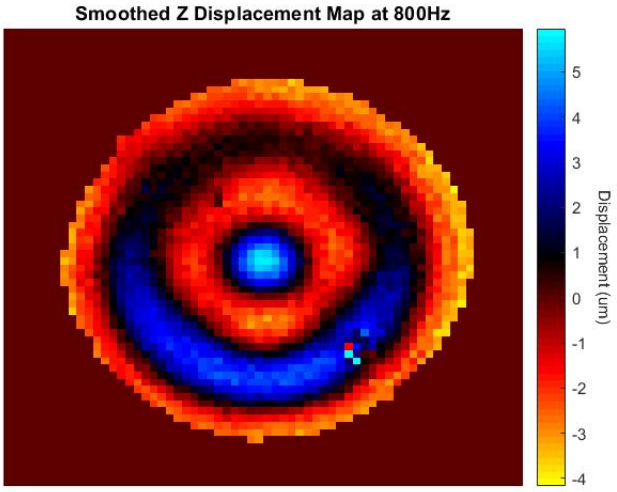

Figure 65: Z displacement map - 800 Hz - 0% elongation.

The results obtained for 800 Hz and no strain conditions are presented below (Figure 66, Figure 67):

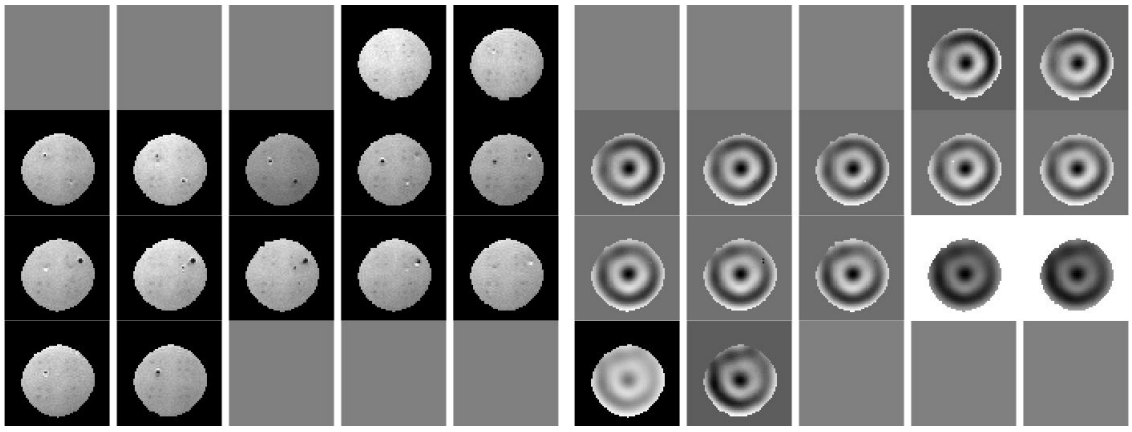

Figure 66: Magnitude (left) and Phase (right) axial cross-sectional sequence of images for 20 layers - 800 Hz - 10% elongation.

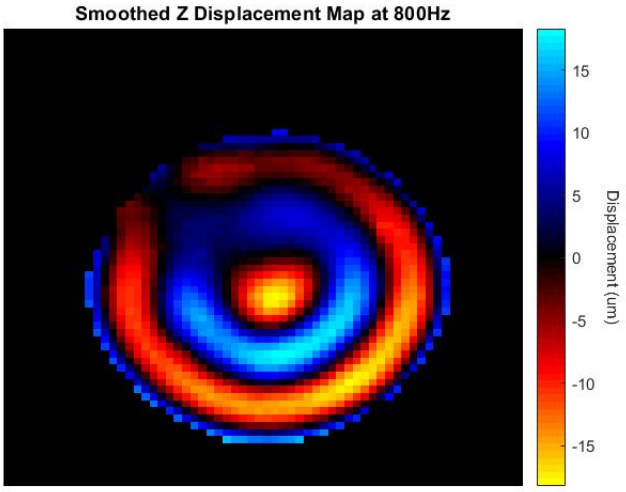

Figure 67: Z displacement map - 800 Hz - 10% elongation.

By comparing the experimental and the theoretical results in terms of displacement it is possible to notice a valid correspondence. The waves in the theoretical results are better defined and the anisotropy is more evident, but the experimental results show a certain level of anisotropy and well-defined wave fronts. Overall, the graphical definition of the images is positive, and there is not an evident amount of noise.

CHAPTER 6

CONCLUSIONS AND FUTURE WORK

6.1 Conclusions

It is possible to state that the setup is functional. It provides the movement expected and the structure is stiff enough to supply the displacement to the phantom and not to the stabilizer. According to the SLDV experiments the torsion is applied correctly to the end point of the phantom and the waves propagate easier in the phantom with low frequency, but they suffer from attenuation once the frequency is increased. Nevertheless, the piezoelectric actuators used for these experiments do not provide a sufficient displacement to be detected by the MRI Agilent 9.4 T system. For this reason they need to be replaced with another type of piezoelectric actuators or air drum system as it will be discussed in the next section. Regarding the axial excitation, the setup is working as expected. The excitation ring provides an axial displacement on the surface of the phantom, and the waves propagate in both the direction according to the frequency imposed in the wave generator and the stiffness of the material. From the SLDV testing, the proper functioning of the piezoelectric actuator is proven, and the surface waves generated by the excitation ring are shown while they propagate throughout the surface of the phantom. From the COMSOL Multiphysics® simulation, it can be seen the expected result in the cross-sectional area of the phantom in terms of stress distribution, when the axial displacement is applied. These results are compared to the MRI Agilent 9.4 T, and

the experimental results confirm the theoretical ones. In both the images it can be asserted the better response of the sample for low frequency, and the presence of attenuation once the frequency is increased up to 1000 Hz. This match reveals the success of the testing and the reliability of the results.

6.2 Future work

The results of the experiments are satisfying, but there are some aspects in the design that can be improved. First, the piezoelectric actuators used for the torsional setup do not provide a sufficient displacement in the phantom to be detected by the MRI system so they need to be replace with something different. It can be a couple of more powerful piezoelectric actuators, but still they should fit in between the stabilizer and the mobile support. It can be difficult to find a piezoelectric actuator that fits and provides a greater power than the ones already used. Another possible solution could be to use an air drum actuation system. It is an innovative technique used for the stimulation of a mouse's heart and it may provide a sufficient displacement [52]. The critical points in this approach is the connection between the source (a speaker) and the point where the displacement needs to be applied. The tube connecting the two end points should have a constant section to avoid the creation of reflective waves travelling backwards and creating interference. At the same time, it should provide a constant section even when the tube is externally stressed, for example in curves or next to the speaker. Once the piezoelectric actuators have been substituted, the experimental setup from the MRI Agilent 9.4 T system can be compare to the ones obtained with the COMSOL Multiphysics® software. Another possible upgrade to the setup would be to provide a shear excitation to the center

of the phantom. For this purpose the excitation ring could be used and the actuation system still entrusted to the piezoelectric actuator. A prismatic guide-way needs to be designed to guarantee the perpendicularity between the excitation and the axis of the phantom. Also, a rigid structure should prevent the ends of the phantom to move accordingly.

Finally, different phantom configurations can be developed and experimented. According to the mechanical properties of the muscle, new phantoms can be better designed. Furthermore, real muscles can be tested with different frequencies and elongations.

APPENDICES

Appendix A

DRAWINGS

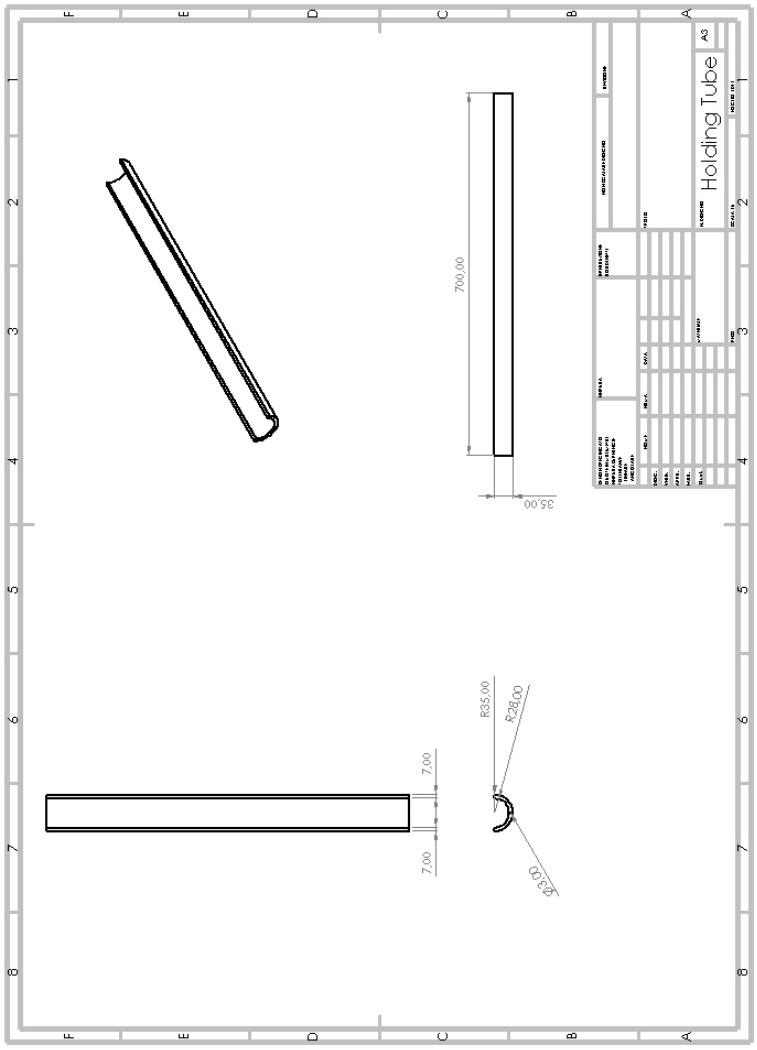

Figure 68: Drafting of the Holding Tube.

Appendix A (continued)

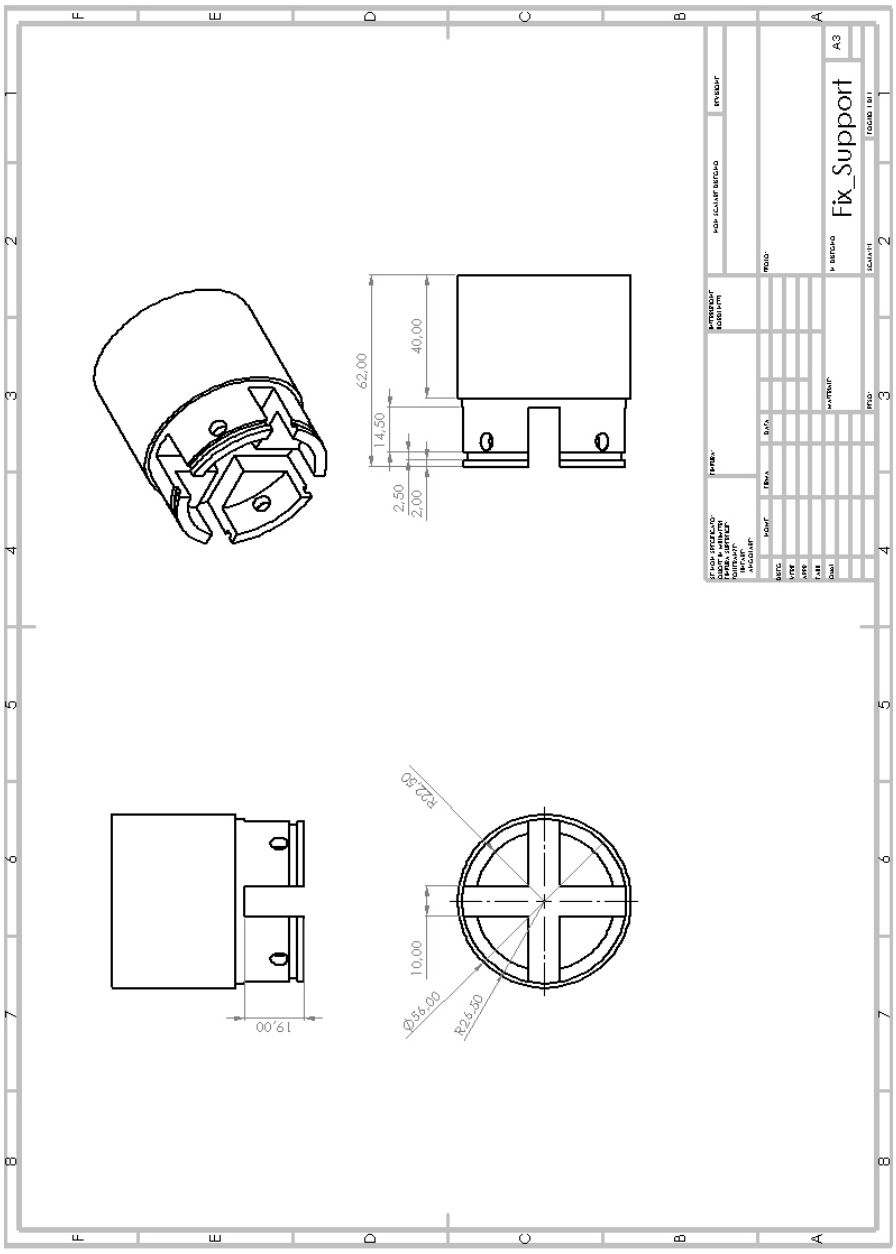

Figure 69: Drafting of the Fix Support.

Appendix A (continued)

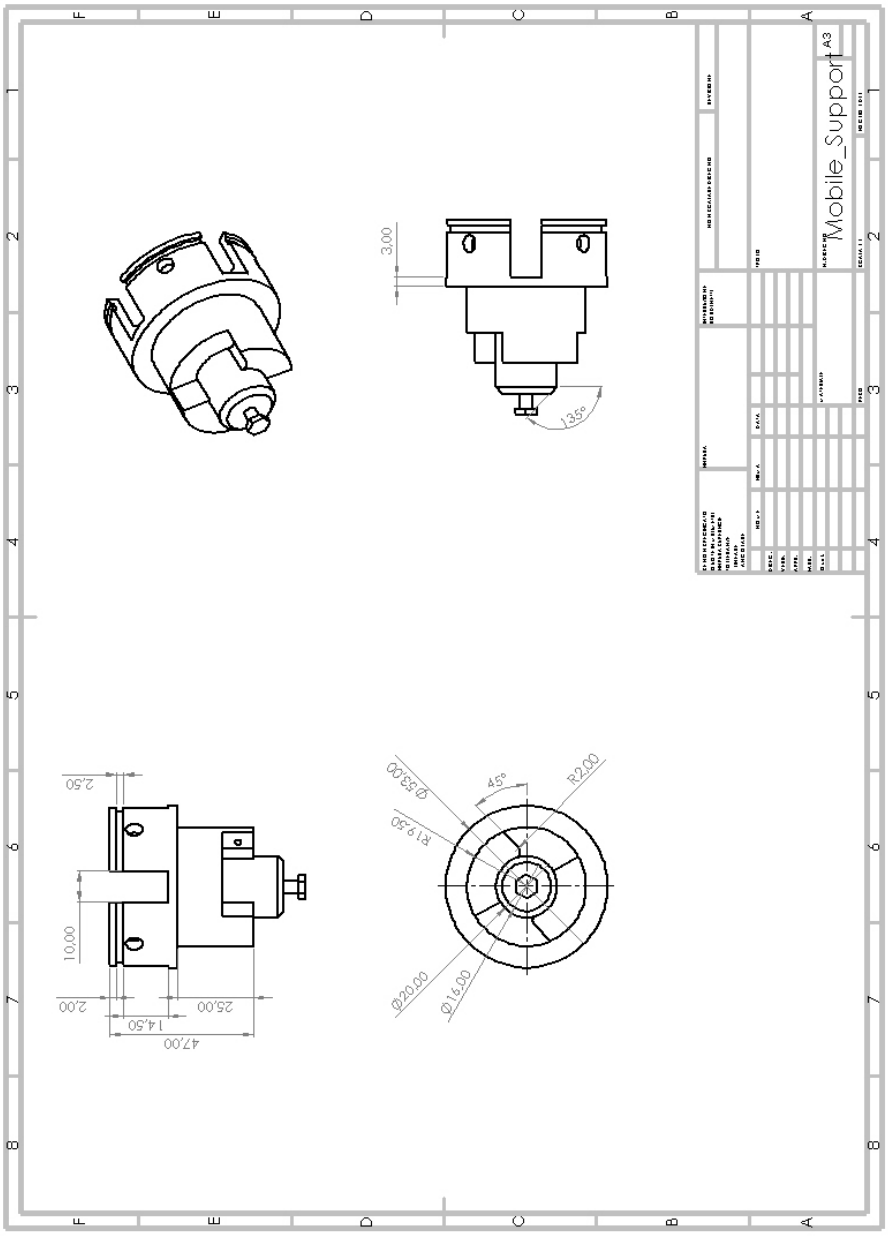

Figure 70: Drafting of the Mobile Support.

Appendix A (continued)

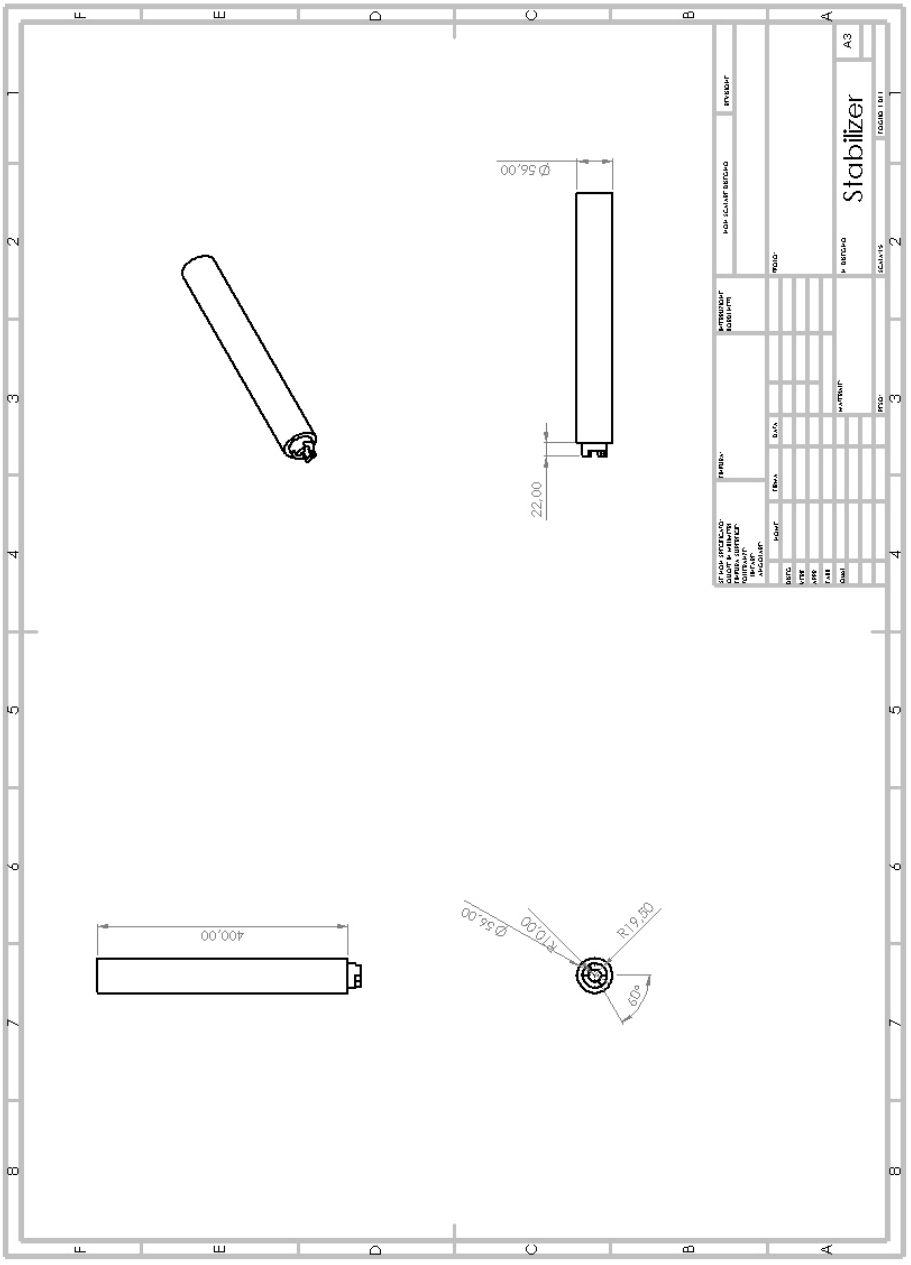

Figure 71: Drafting of the Stabilizer.

Appendix A (continued)

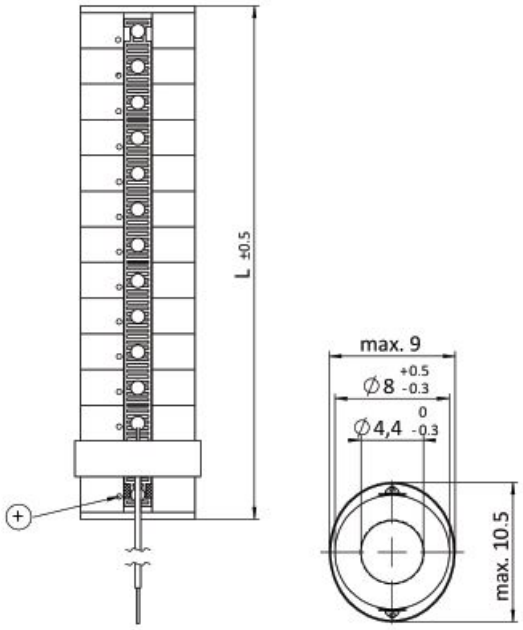

Figure 72: Drafting of the $PICMA^{®}$ Stack Multilayer Ring Actuator P-080.

Appendix A (continued)

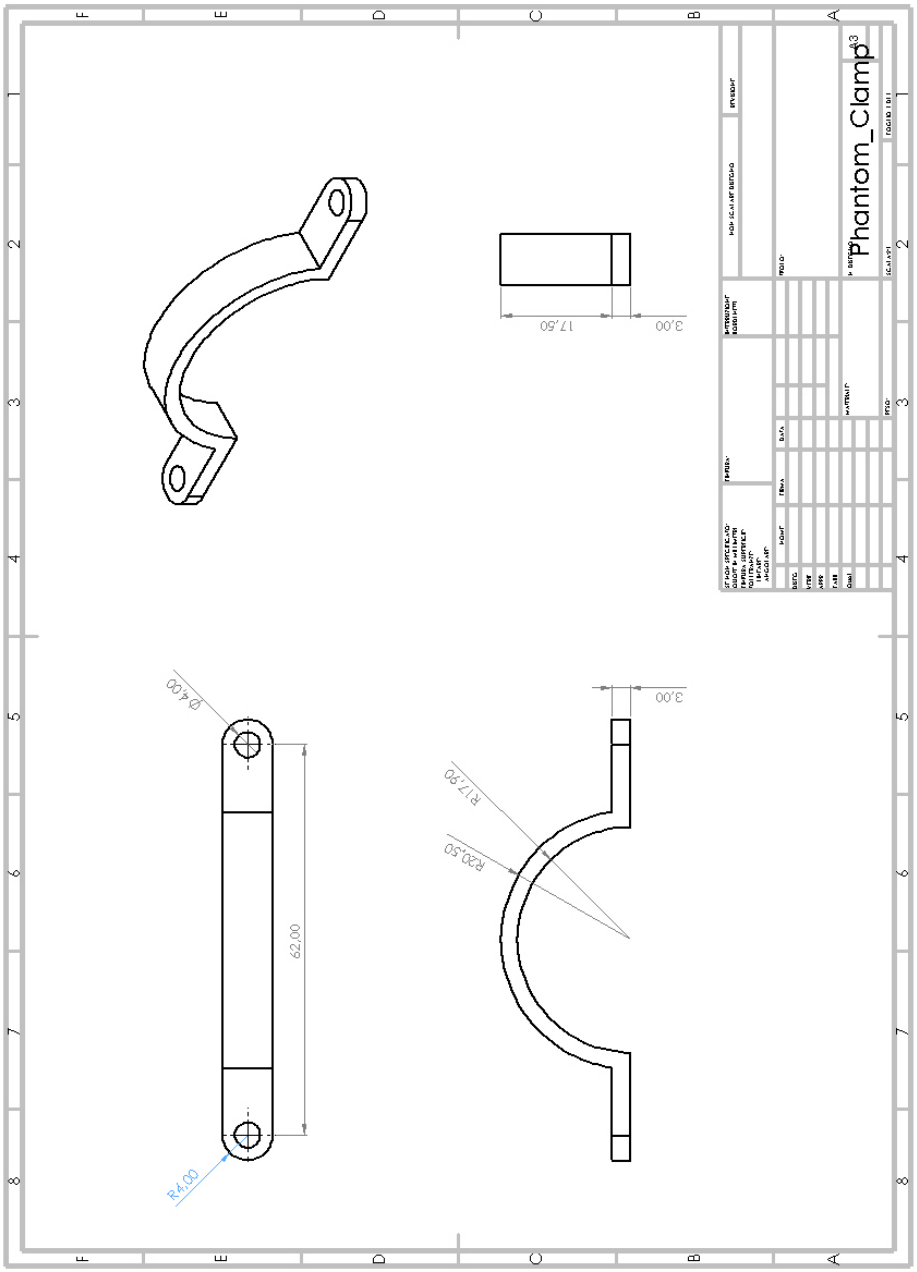

Figure 73: Drafting of the Phantom clamp.

Appendix A (continued)

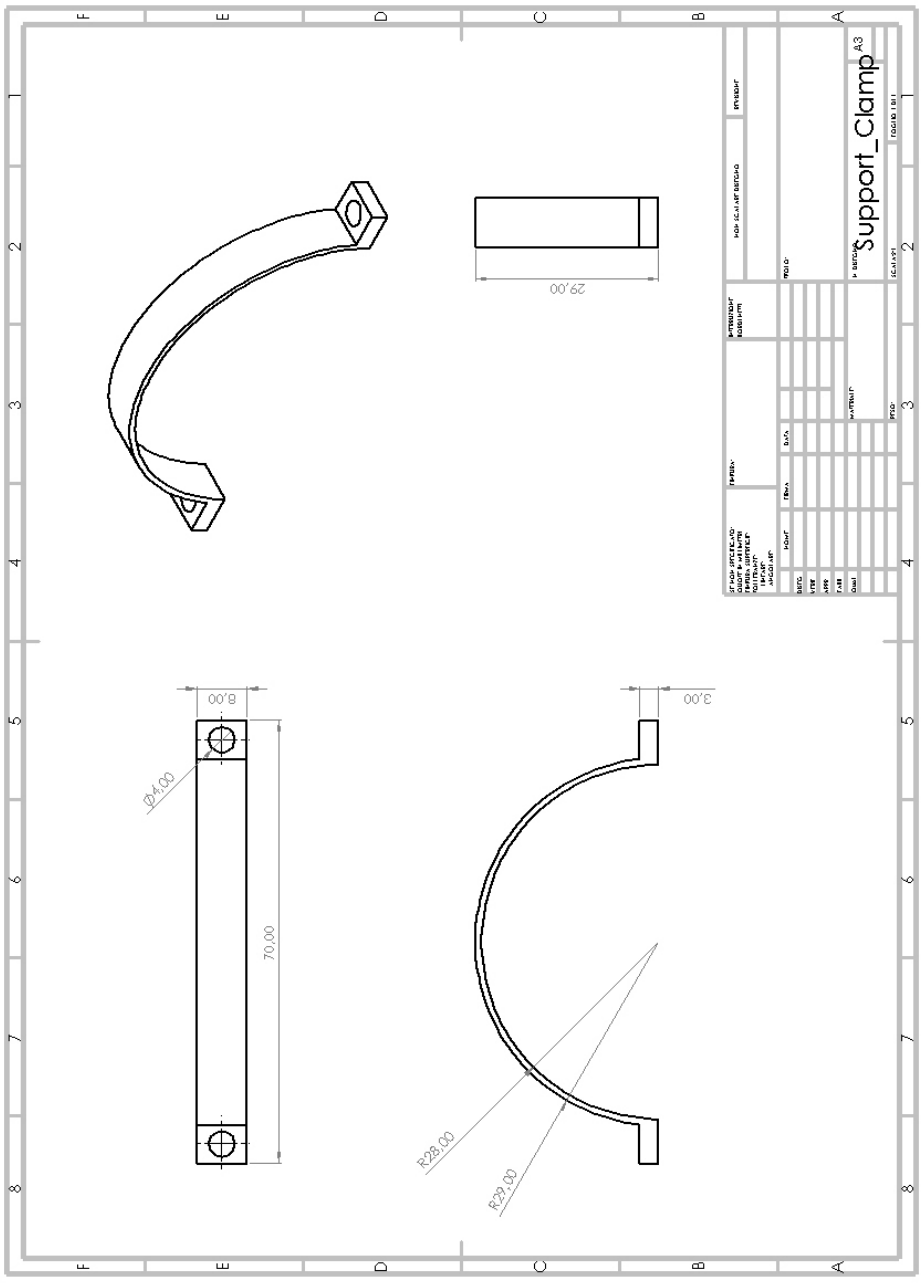

Figure 74: Drafting of the Support clamp.

Appendix A (continued)

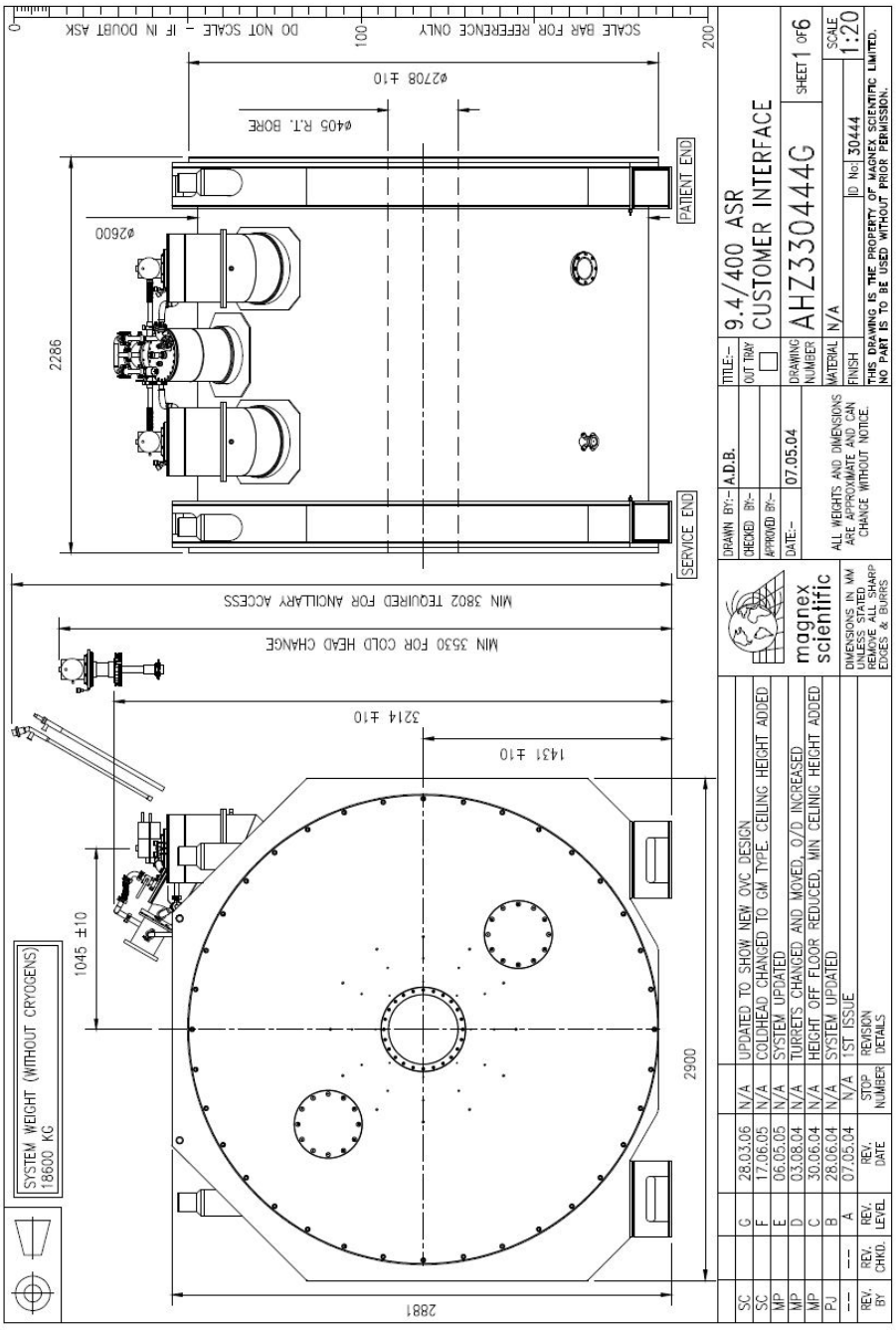

Figure 75: Drafting of the MRBR 9.4 TESLA/400 MM/ASR MAGNET SYSTEM - provided by Agilent Technologies, Inc.

Appendix B

MATLAB CODE

B.1 SLDV Post-processing

```
clear all
load ScanHorizAG600Hz04152021BandWidth2KHz_ax.txt; dum0=
    ScanHorizAG600Hz04152021BandWidth2KHz_ax;
load Prestressed10_600Hzx.txt; dum1=Prestressed10_600Hzx;
load Prestressed20_600Hzx.txt; dum2=Prestressed20_600Hzx;
load ScanMSAG400Hz04132021_ax.txt; dumV=ScanMSAG400Hz04132021_ax;
x0=dum0(:,2); y0=dum0(:,3); vr0=dum0(:,5); vi0=dum0(:,6);
x1=dum1(:,2); y1=dum1(:,3); vr1=dum1(:,5); vi1=dum1(:,6);
x2=dum2(:,2); y2=dum2(:,3); vr2=dum2(:,5); vi2=dum2(:,6);
xV=dumV(:,2); yV=dumV(:,3); vrV=dumV(:,5); viV=dumV(:,6);
%
FrealX0=scatteredInterpolant(x0,y0,vr0);FimagX0=scatteredInterpolant
    (x0,y0,vi0);
xa0=linspace(0,max(x0)-min(x0),100);ya0=linspace(0,max(y0)-min(y0)
    ,100);
xq0=repmat(xa0,100,1); yq0=repmat(ya0',1,100); F.Method = 'nearest';
```

Appendix B (continued)

```
14 zrealq0 = FrealX0(xq0+min(x0),yq0+min(y0));zimagq0 = FimagX0(xq0+min
       (x0),yq0+min(y0));
15 %
16 FrealX1=scatteredInterpolant(x1,y1,vr1);FimagX1=scatteredInterpolant
       (x1,y1,vi1);
17 xa1=linspace(0,max(x1)-min(x1),100);ya1=linspace(0,max(y1)-min(y1)
       ,100);
18 xq1=repmat(xa1,100,1); yq1=repmat(ya1',1,100); F.Method = 'nearest';
19 zrealq1 = FrealX1(xq1+min(x1),yq1+min(y1));zimagq1 = FimagX1(xq1+min
       (x1),yq1+min(y1));
20 %
21 FrealX2=scatteredInterpolant(x2,y2,vr2);FimagX2=scatteredInterpolant
       (x2,y2,vi2);
22 xa2=linspace(0,max(x2)-min(x2),100);ya2=linspace(0,max(y2)-min(y2)
       ,100);
23 xq2=repmat(xa2,100,1); yq2=repmat(ya2',1,100); F.Method = 'nearest';
24 zrealq2 = FrealX2(xq2+min(x2),yq2+min(y2));zimagq2 = FimagX2(xq2+min
       (x2),yq2+min(y2));
25 %
26 FrealXV=scatteredInterpolant(xV,yV,vrV);FimagXV=scatteredInterpolant
       (xV,yV,viV);
```

Appendix B (continued)

```
27 xaV=linspace(0,max(xV)-min(xV),100);yaV=linspace(0,max(yV)-min(yV)
       ,100);
28 xqV=repmat(xaV,100,1); yqV=repmat(yaV',1,100); F.Method = 'nearest';
29 zrealqV = FrealXV(xqV+min(xV),yqV+min(yV));zimagqV = FimagXV(xqV+min
       (xV),yqV+min(yV));
30 %%
31 % figure(1),surfc(xq,yq,zrealq);view([0 0 1]); axis('equal');
       shading interp; colorbar; colormap jet; caxis([-.0005 .0005])
32 % xt = get(gca, 'XTick'); set(gca, 'FontSize', 14);
33 %% title('X-motion encoded');
34 %% xlabel('x axis: parallel to plane of isotropy (mm)');
35 %% ylabel('y axis: parallel to axis of isotropy (mm)');
36 % figure(2),surfc(xq,yq,-zimagq);view([0 0 1]); axis('equal');
       shading interp; colorbar; colormap jet; caxis([-.0005 .0005])
37 % xt = get(gca, 'XTick'); set(gca, 'FontSize', 14);
38 %% title('Out of Phase');
39 %% xlabel('x axis: parallel to plane of isotropy (mm)');
40 %% ylabel('y axis: parellel to axis of isotropy (mm)');
41 %%
42 xa0=max(x0)-min(x0)-xa0;xa1=max(x1)-min(x1)-xa1;xa2=max(x2)-min(x2)-
       xa2;%xaV=max(xV)-min(xV)-xaV;
```

Appendix B (continued)

```
43 a0=mean(unwrap(angle(zrealq0+i*zimagq0),[],2))/pi/2; a1=mean(unwrap(
       angle(zrealq1+i*zimagq1),[],2))/pi/2;
44 a2=mean(unwrap(angle(zrealq2+i*zimagq2),[],2))/pi/2; aV=mean(unwrap(
       angle(zrealqV+i*zimagqV),[],2))/pi/2;
45 figure(3),subplot(2,1,1),plot(xa0,mean(zrealq0),'k-',xa1,mean(
       zrealq1),'b--',xa2,mean(zrealq2),'r:'); axis([0 .04 -1e-3 1e-3]);
        grid;%,xaV,mean(zrealqV),'g-.'
46 subplot(2,1,2),plot(xa0,mean(zimagq0),'k-',xa1,mean(zimagq1),'b--');
       axis([0 .04 -1e-3 1e-3]); grid;%,xaV,mean(zimagqV),'g-.'
47 figure(4),subplot(2,1,1),semilogy(xa0,mean(abs(zrealq0+i*zimagq0)),'
       k-',xa1,mean(abs(zrealq1+i*zimagq1)),'b--',xa2,mean(abs(zrealq2+i
       *zimagq2)),'r:'); grid; %axis([0 .04 1e-4 1e-3]);%,xaV,mean(abs(
       zrealqV+i*zimagqV)),'g-.'
48 subplot(2,1,2),plot(xa0,a0-a0(100),'k-',xa1,a1-a1(100),'b--',xa2,a2-
       a2(100),'r:'); grid; %axis([0 .04 -1e-3 1e-3]);%,xaV,aV-aV(1),'g
       -.'
49 %%
50 % figure(5)
51 % u = uicontrol('Style','slider','Position',[10 50 20 340],...
52 %       'Min',1,'Max',32,'Value',1);
53 % filename = 'manimated.gif';
```

Appendix B (continued)

```
54 %% for k = 1:32
55 %%     surfc(xq,yq,zrealq*cos((k-1)/16*pi)-zimagq*sin((k-1)/16*pi))
       ;view([0 0 1]); axis('equal'); shading interp; colorbar; colormap
        jet;
56 %%     caxis([-.0005 .0005]); xt = get(gca, 'XTick'); set(gca, '
       FontSize', 14);
57 %%%     title('X-motion encoded');
58 %%%     xlabel('x axis: parallel to plane of isotropy (mm)');
59 %%%     ylabel('y axis: parallel to axis of isotropy (mm)');
60 %%     u.Value = k;
61 %%     M(k) = getframe(gcf);
62 %%     im = frame2im(M(k));
63 %%     [imind,cm] = rgb2ind(im,256);
64 %%     if k == 1
65 %%         imwrite(imind,cm,filename,'gif', 'Loopcount',inf);
66 %%     else
67 %%         imwrite(imind,cm,filename,'gif','WriteMode','append');
68 %%     end
69 %% end
70 % for k = 1:32
```

Appendix B (continued)

```
71 %      plot(xa,mean(zrealq)*cos((k-1)/16*pi)-mean(zimagq)*sin((k-1)
       /16*pi)); axis([0 .04 -1e-3 1e-3]);
72 %      xt = get(gca, 'XTick'); set(gca, 'FontSize', 14);
73 %%      title('X-motion encoded');
74 %%      xlabel('x axis: parallel to plane of isotropy (mm)');
75 %%      ylabel('y axis: parallel to axis of isotropy (mm)');
76 %      u.Value = k;
77 %      M(k) = getframe(gcf);
78 %      im = frame2im(M(k));
79 %      [imind,cm] = rgb2ind(im,256);
80 %      if k == 1
81 %            imwrite(imind,cm,filename,'gif', 'Loopcount',inf);
82 %      else
83 %            imwrite(imind,cm,filename,'gif','WriteMode','append');
84 %      end
85 % end
86 % figure(6)
87 % axes('Position',[0 0 1 1])
88 % movie(M,10)
```

Appendix B (continued)

B.2 Agilent Post-processing

```
clear all, close all

%input
load cmp_elast.mat
load cmp_waves.mat

freqs = [800];
density = 1000;
rot = 0;
plotDim = 'axial';
maskingMethod = 'threshold';
% Frequency Dependent Inversion
for f = 1:size(freqs,2)
    disp(fprintf('%dHz',freqs(f)))
    [file, path] = FIDREAD_SEV2();

    bw = SemiAutoMask(mag,maskingMethod);
    uw = PhaseUnwrap(phi,bw);
    edgeErosion = 3; spacing = 14; order = 5; %5
```

Appendix B (continued)

```
20      [G1, CW_X, CW_Y, CW_Z, BWa, abs_G1, phi_G1, CURL, DIV] =
            Inv3d_Curl(uw,par,bw,edgeErosion,spacing,order);
21
22      Mag(:,:,:,f) = squeeze(mag(:,:,1,:));
23      Phase(:,:,:,f) = squeeze(uw(:,:,1,:));
24      BW(:,:,:,f) = BWa;
25      Gw(:,:,:,f) = G1;
26      U(:,:,:,1,f) = CW_X; U(:,:,:,2,f) = CW_Y; U(:,:,:,3,f) = CW_Z;
27      Ucurl(:,:,:,:,f) = CURL;
28      Ulap(:,:,:,:,f) = DIV;
29      Phi(:,:,:,f) = phi_G1;
30  end
31
32  % Multifrequency Inversion
33  [G_mod,phi_mod] = MultiFreqInversion(Ucurl,Ulap,BWa,freqs,density);
34
35  % Spatial Averaging
36  ave_G = median(G_mod(BWa), 'all');
37
38  %Sample slice of Image
39  previewSlice = ceil(size(Mag,3)/2);
```

Appendix B (continued)

```
40 VisualizeFrequencyResults(Mag,Phase,Gw,U,BW,freqs,previewSlice,
       plotDim,rot,cmp,cmp2)
41
42 Im0 = bw(:,:,previewSlice).*squeeze(Mag(:,:,previewSlice,1));
43 Im1 = medfilt2(G_mod(:,:,previewSlice), [6 6]); Im1(Im1 == 0) = NaN;
44 OverlayResults(Im0, Im1,'Frequency Independent Shear Modulus', '
       Modulus Value (kPa)','gray', cmp2)
45
46 Im1 = medfilt2(phi_mod(:,:,previewSlice), [6 6]); Im1(Im1 == 0) =
       NaN;
47 %%
48 OverlayResults(Im0, Im1,'Frequency Independent Phase', 'Modulus
       Value (kPa)','gray', cmp2)
49
50
51 function VisualizeFrequencyResults(mag, pha, G, U,BW,freqs,
       previewSlice,plotDim,rot,wavCmp,Gcmp)
52     %Visualize Magnitude and Phase images in one figure each
53     plotX = floor(sqrt(size(mag,3)));
54     plotY = ceil(size(mag,3)/plotX);
55     plotSize = [plotX, plotY];
```

Appendix B (continued)

```
56
57      for f = 1: size(mag,4)
58          Im = squeeze(BW(:,:,:,f)).*squeeze(mag(:,:,:,f));
59          Plot3dSlices(Im,'gray',plotDim,rot, plotSize);
60
61          Im = squeeze(BW(:,:,:,f)).*squeeze(pha(:,:,:,f));
62          Plot3dSlices(Im,'gray',plotDim,rot,plotSize)
63
64          %Visualize Wave Images
65          dir = ['X', 'Y', 'Z'];
66          for d = 1:size(U,4)
67              figTitle = sprintf('Smoothed %s Displacement Map at %dHz
                    ', dir(d),freqs(f));
68              Im = BW(:,:,previewSlice,f).*real(U(:,:,previewSlice,d,f
                    ));
69              PlotWaveSlice(Im,figTitle,'Displacement (um)',wavCmp)
70          end
71
72          %Visualize Storage and Loss Moduli overlayed on Magnitude
                image
```

Appendix B (continued)

```
73          Im0 = squeeze(BW(:,:,previewSlice,f)).*squeeze(mag(:,:,
                previewSlice,f));
74          Im1 = medfilt2(real(G(:,:,previewSlice,f)), [6 6]); Im1(Im1
                == 0) = NaN;
75          OverlayResults(Im0, Im1, sprintf('Storage Modulus %dHz',freqs
                (f)), 'Modulus Value (kPa)','gray', Gcmp)
76
77          Im0 = squeeze(BW(:,:,previewSlice,f)).*squeeze(mag(:,:,
                previewSlice,f));
78          Im1 = medfilt2(imag(G(:,:,previewSlice,f)), [6 6]); Im1(Im1
                == 0) = NaN;
79          OverlayResults(Im0, Im1, sprintf('Loss Modulus %dHz',freqs(f)
                ), 'Modulus Value (kPa)','gray', Gcmp)
80      end
81  end
82
83  function PlotWaveSlice(Im, figTitle, clrBarTitle, cmp)
84      figure
85      imagesc(Im)
86      axis off
87      colormap(cmp)
```

Appendix B (continued)

```
88      hcb = colorbar('vertcat');
89      hyl = ylabel(hcb, clrBarTitle, 'Rotation', 270);
90      hyl.Position(1) = hyl.Position(1) + 0.8;
91      title(figTitle)
92  end
93  function OverlayResults(Im0, Im1,figTitle, clrBarTitle,cmp1, cmp2)
94      figure
95      %back image
96      a1 = axes;
97      h1 = imagesc(Im0); colormap(a1, cmp1); axis off; c1 = colorbar;
            c1.Visible = 'off';
98      title(figTitle)
99      %front image
100     a2 = axes;
101     h2 = imagesc(Im1); colormap(a2, cmp2);  axis image; a2.Visible =
            'off';
102     c2 = colorbar('vertcat');
103     hyl = ylabel(c2, clrBarTitle, 'Rotation', 270);
104     hyl.Position(1) = hyl.Position(1) + 0.8;
105     linkaxes([a1,a2]);
106     % Make Forward Image Transparent at Padding
```

Appendix B (continued)

```
107         alpha(h2, isfinite(Im1)*1);
108         set(h2,'AlphaData',~isnan(Im1)*0.5)
109     end
```

CITED LITERATURE

1. Yogesh K. Mariappan, K. J. G. and Ehman, R. L.: Magnetic resonance elastography. Clinical Anatomy, 23:497—-511, 2010.

2. Rosa M.S. Sigrist, Joy Liau, A. E. K. M. C. C. J. K. W.: Ultrasound elastography: Review of techniques and clinical applications. Theranostics, 7(5):1303–1329, 2017.

3. Nanomotion technology, how it works. `https://www.nanomotion.com/nanomotion-technology/works/`. Accessed: 2021-03-15.

4. Elastography. `https://www.radiologyinfo.org/en/info.cfm?pg=elastography`. Accessed: 2021-03-30.

5. Lecture notes, bioe 594 "elastography". Instructor: Dieter Klatt. Fall 2020, University of Illinois at Chicago.

6. I. Levental, K.R. Levental, E. K. R. A. R. M. R. W. and Janmey, P.: A simple indentation device for measuring micrometer-scale tissue stiffness. J Phys Condens Matter, 22(19), 2010.

7. Amador, C., U. M. W. S. C. Q. C. K.-N. A. . G. J.: Shear elastic modulus estimation from indentation and sduv on gelatin phantoms. IEEE TRANSACTIONS ON BIOMEDICAL ENGINEERING, 58(6):1706–1714, 2011.

8. J.L. Gennisson, T. Deffieux, M. F. M. T.: Ultrasound elastography: Principles and techniques. Journal de Radiologie Diagnostique et Interventionnelle, 94(5):504–513, 2013.

9. Cardiac mr tagging or myocardial tagging refers to a mri based acquisition method designed for myocardial deformation analysis. `https://radiopaedia.org/articles/mr-tagging`. Accessed: 2021-03-31.

10. Chung, S., B. E. M. L. . A. L.: Liver stiffness assessment by tagged mri of cardiac-induced liver motion. Magnetic Resonance in Medicine, 65(4):945–955, 2011.

CITED LITERATURE (continued)

11. Magnetic resonance imaging. https://en.wikipedia.org/wiki/Magnetic_resonance_imaging#:~:text=Magnetic\%20resonance\%20imaging\%20(MRI)\%20is,the\%20organs\%20in\%20the\%20body. Accessed: 2021-03-31.

12. The piezoelectric effect. https://www.nanomotion.com/nanomotion-technology/piezoelectric-effect/#:~:text=Piezoelectric\%20Effect\%20is\%20the\%20ability,is\%20Greek\%20for\%20\%E2\%80\%9Cpush\%E2\%80\%9D. Accessed: 2021-03-31.

13. Anycubic photon review [2021]: Will this work for you? https://www.cdimiami.com/advantages-of-using-elastography-in-medical-imaging/. Accessed: 2021-04-02.

14. Guidetti, M.: Transverse Isotropic Multiscale Muscle Phantom for MR Elastography. Phd thesis, University of Illinois at Chicago, October 2017.

15. Xianpeng HuE, Fang-Hua Lin, C. L.: Equations for viscoelastic fluids. Handbook of Mathematical Analysis in Mechanics of Viscous Fluids, pages 1–29, 2016.

16. Magnetic resonance imaging (mri) of the brain and spine: Basics. https://case.edu/med/neurology/NR/MRI\%20Basics.htm, 2016. Accessed: 2021-04-02.

17. Seong-Joo Lee, Keunhong Jeong, J. H. S. H. J. L. S. M. H. C. S. K. N. . K. K.: Squid-based ultralow-field mri of a hyperpolarized material using signal amplification by reversible exchange. Scientific Reports, 9(12422):1–8, 2019.

18. Murase, K., . T. N.: Numerical solutions to the time-dependent bloch equations revisited. Magnetic Resonance Imaging, 29(1):126–131, 2011.

19. Jinghua Wang, Weihua Mao, M. Q. M. B. S. and Constable, R. T.: Factors influencing flip angle mapping in mri: Rf-pulse shape, slice-select gradients, off-resonance excitation, and bo inhomogeneities. Magnetic Resonance in Medicine, 56(1):463–468, 2006.

20. Richard B. Bucton, Robert R. Edelman, B. R. R. G. L. W. and Brady, T. J.: Contrast in rapid mr imaging: T1- and t2-weighted imaging. Journal of Computer Assisted Tomography, 11(1):7–16, 1987.

21. Magin Richard, Feng Xu, B. D.: Solving the fractional order bloch equation. Concepts in Magnetic Resonance Part A, 34A(1):16–23, 2009.

CITED LITERATURE (continued)

22. Clare, S.: Functional MRI : Methods and Applications. Phd thesis, University of Nottingham, October 1997.

23. Basic plane mathematics of mri. https://my-ms.org/mri_planes.htm#:~:text=Magnetic20resonance20imaging20(MRI)20is,the20image20that20is20taken.&text=The20basic20orientation20terms20forwould20be20a20transverse. Accessed: 2021-04-10.

24. Mri instrumentation and mri safety - magnetic field gradients are needed to encode the signal spatially. https://www.imaios.com/en/e-Courses/e-MRI/MRI-instrumentation-and-MRI-safety/gradients. Accessed: 2021-04-10.

25. Spatial encoding – basic imaging sequences. https://radiologykey.com/spatial-encoding-basic-imaging-sequences/#:~:text=The\%20space\%20dependence\%20of\%20the,to\%20a\%20well\%2Ddefined\%20region. Accessed: 2021-04-10.

26. Piezo actuators: Types and applications. https://www.americanpiezo.com/piezo-theory/actuators.html. Accessed: 2021-04-10.

27. Step motor basics. https://www.geckodrive.com/support/step-motor-basics.html. Accessed: 2021-04-10.

28. Panagiotis Vartholomeos, Christos Bergeles, L. Q. and Dupont, P. E.: An mri-powered and controlled actuator technology for tetherless robotic interventions. The International Journal of Robotics Research, 32(13):1536–1552, 2013.

29. Díaz-de Anda, A., F. J. G. L. M.-S. R. A. M. G. . M. A.: Experimental study of the timoshenko beam theory predictions. Journal of Sound and Vibration, 331(26):5732–5744, 2012.

30. Magnetic resonance imaging. https://en.wikipedia.org/wiki/Timoshenko\%E2\%80\%93Ehrenfest_beam_theory. Accessed: 2021-04-11.

31. Axial stress. http://www.wikiengineer.com/Structural/AxialStress. Accessed: 2021-04-11.

32. Shear stress. https://en.wikipedia.org/wiki/Shear_stress. Accessed: 2021-04-11.

CITED LITERATURE (continued)

33. Shear stress in engineering. http://www.wikiengineer.com/Structural/ShearStress. Accessed: 2021-04-11.

34. Torsion (mechanics). https://en.wikipedia.org/wiki/Torsion_(mechanics). Accessed: 2021-04-12.

35. What is torsional stress? — torsional shear stress. https://extrudesign.com/torsional-stress-torsional-shear-stress/#:~:text=Torsional\%20shear\%20stress\%20or\%20Torsional,the\%20couple\%20acting\%20on\%20it. Accessed: 2021-04-12.

36. Spatial encoding in mri. https://www.imaios.com/en/e-Courses/e-MRI/Signal-spatial-encoding/Phase-encoding. Accessed: 2021-04-10.

37. Gallagher, T. A., N. A. J. . H.-B.-L.: An introduction to the fourier transform: Relationship to mri. American Journal of Roentgenology, 190(5):1396–1405, 2008.

38. Tweten DJ, R. J. O. and Bayly, P. V.: Requirements for accurate estimation of anisotropic material parameters by magnetic resonance elastography: A computational study. Magn. Reson. Med., 78(6):2360–2372, 2017.

39. Tweten DJ, R. J. Okamoto, J. L. S.-J. R. G. and Bayly, P. V.: Estimation of material parameters from slow and fast shear waves in an incompressible, transversely isotropic material. J. Biomech, 48(15):4002–4009, 2015.

40. Destrade M, O. R.: On stress-dependent elastic moduli and wave speeds. IMA Journal of Applied Mathematics, 78(5):965–997, 2013.

41. Ogden RW, S. B.: Propagation of waves in an incompressible transversely isotropic elastic solid with initial stress: Biot revisited. Journal of Mechanics of Materials and Structures, 6(1–4):453–477, 2011.

42. Technologies, A.: Specification for an mrbr 9.4 tesla/400 mm/asr magnet system. Magnex Scientific Limited The Magnet Technology Centre, 1(1):1–13, 2006.

43. Advantages of using elastography in medical imaging. https://total3dprinting.org/anycubic-photon-review/#:~:text=DLP\%2C\%20or\%20digital\%20light\%20processing,liquid\%20resin\%20and\%20UV\%20rays. Accessed: 2021-03-31.

CITED LITERATURE (continued)

44. Viscoelasticity and rheological models. https://www.viskoelasticita.cz/soubor/viscoelasticity-and-rheological-models-pdf/. Accessed: 2021-04-12.

45. Rheological models. http://homepages.engineering.auckland.ac.nz/~pkel015/SolidMechanicsBooks/Part_I/BookSM_Part_I/10_Viscoelasticity/10_Viscoelasticity_03_Rheological.pdf. Accessed: 2021-04-12.

46. Linear elastic model. https://www.sciencedirect.com/topics/engineering/linear-elastic-model. Accessed: 2021-04-12.

47. Klatt, D., P. S. B. J. . S.-I.: Viscoelasticity-based mr elastography of skeletal muscle. Physics in Medicine and Biology, 55(21):6445–6459, 2010.

48. Doppler effect. https://en.wikipedia.org/wiki/Doppler_effect. Accessed: 2021-04-13.

49. Nolte, D.: The fall and rise of the doppler effect. Physics Today, 73(3):30–31, 2020.

50. Pina Colarusso, Linda H. Kidder, I. W. L.-E. N. L.: Raman and infrared microspectroscopy. Encyclopedia of Spectroscopy and Spectrometry, 1(1):1945–1954, 1999.

51. Sammet, S.: Magnetic resonance safety. Abdominal radiology, 41(3):444–451, 2016.

52. Yifei Liu, Thomas J. Royston, D. K. and Lewandowski, E. D.: Cardiac mr elastography of the mouse: Initial results. Magnetic Resonance in Medicine, 76(1):1879–1886, 2016.

VITA

NAME: Alberto Giarola

EDUCATION: Bachelor of Science in Mechanical Engineering, Politecnico di Torino, Turin, Italy, 2016−2019

Master of Science in Mechanical Engineering, Politecnico di Torino, Turin, Italy, 2019−*Present*

Master of Science in Mechanical Engineering, University of Illinois at Chicago, Chicago, 2020−*Present*

EXPERIENCE: Graduate Research Assistant in the Acoustics and Vibrations Laboratory, Richard and Loan Hill Department of Bioengineering, University of Illinois at Chicago, Chicago, Jan 2021−*Present*